Novel functionalized and patterned surfaces for cardiovascular applications

Romain Schieber

A thesis submitted to *Universitat Politècnica de Catalunya* and *Universität des Saarlandes* for the double degree of Doctor of Philosophy under Joint European Doctoral Programme in Materials Science and Engineering (DocMASE)

Supervisors:
Dr. Marta Pegueroles Neyra
Prof. Frank Mücklich

Barcelona, September 2017

Acknowledgments

Acknowledgements come first in the PhD thesis and, paradoxically, it is usually the very last part we write. Why is that? In my case, it is because I was scared… Obviously this task force us to remember all the people who helped and brightened up the (long) 5 years PhD journey… Then, writing acknowledgments is about realizing: all the beautiful persons I met, all the magic and intense moments we shared, all the scientific terrific mountains we projected to climb and were the firsts to summit. So I was scared to fully realize how unique was my PhD… at the moment it ends…

In the first place, I would like to thank my supervisor Marta Pegueroles. I started the PhD as a student and I leave it as a team-worker with so many scientific, organizational, and above all, relational skills. Marta, this transformation is the result of your professionalism and implication, thank you so much. In addition, I thank you for your peaceful and comprehensive behavior during all the PhD. You were my climbing rope and you made the mountains seem not that terrific ;-)

I would like to thank Prof. Maria Pau Ginebra and Prof. Xavier Gil for believing I could be a good PhD student, for finding a way I could incorporate their BBT team and for giving us the best conditions to investigate.

I had the chance to be part of the DocMASE programme and so I had a second university in Saarbrucken. I would like to thank Prof. Dr. Ing. Frank Mücklich for giving me the opportunity to work in his institute and for supervising this work. I also thank Flavio, the coordinator of the DocMASE programme. That's a huge work and responsibility which you manage perfectly and with dedication. I will always remember when I came to Saarbrucken for the first time without knowing a word of German… You picked me up at the airport, brought me to the room you booked for me, helped me to go through all the administrative tasks and introduced me to your group of friends. One can't expect more the first day in a new country… So Flavio, thank you for your friendship!

Flavio is in the category of people who make your life easier through their professionalism and their proactivity. In UPC I met many people in this category. Txell and Noelia are the masters in this field. Thank you so much for being there

and finding a solution to every problem I had during my PhD. In this category are included Montse, Trifon and Kim… Thank you to the three of you for finding time in your crazy schedules, helping all the times I needed it and also for doing it with enthusiasm and smiles. An unexpected person here is Maria-Angeles, she is not a scientist but I can assure you that with her happiness, positiveness and her energy she contributed significantly to our good research… So thank you so much Maria-Angeles.

Writing these acknowledgments the word HELP is going through my mind again and again… and I fully realize how lucky I was to grow with all this friendly workmates who always helped and transmitted there tricks and knowledges… Thanks to you I got the "climbing" techniques to go through the tricky sections of the mountains. Thank you Montse, for asking always about my progress and making me feel I did a great job. Thank you Cris, for your plasma and PLLA expertise. Thank you Daniel, for helping during my first congress in Granada. Thank you Cris, for your smile and your help even after 7 months of pregnancy. Thank you Jordi, for answering with patience to all my silly biological questions. Thank you to the enterprise-team (Miquel, Monica and Sergi) for transmitting always good vibes. Thank you Joan Josep, for rescuing me from the deepest crevasse I fell during PhD… the famous humid AFM crevasse! Thank you Carles Boludo, for inspiring me, you are my scientific hero and on top of that, you always find time to answer my technical or personal questions.

You don't climb a mountain without some friends to share the experience or the doubts with… In my case these close friends are so many that they got a team named: Pollitos&Pollitas ☺ I thank all of you for creating and being part of the Jungle Speed lunch therapy group… Most of the time you made me live this experience so happily, and the rest of the time you helped me to see the glass half-full. Thanks Erica, for sharing the same life balance and for our escape from PhD to Frankenjura. Thanks Erik for introducing me most of the Barcelona social places I know. Thanks Mire for being my PhD confident and for our summer library sessions. Thanks Robi for discovering the PhD experience side-by-side, even if you did everything faster. Thanks Quentin for your sarcastic vision of life and for all your administrative tricks. Thanks Yas for your father attitude with me at the beginning. Thanks Gius for being such an altruistic friend hidden behind this strange guy who preferred to wash his desk than meeting me properly.

Thanks Dani for being indulgent with my disastrous birthday mistake. Thanks Dani[2] for making me feel president, even if it is only president of the Gluten-free PhD student association. Thanks Jose for this unforgettable night in Stockholm. Thanks Nati for being my PhD mother during my first PhD steps. Thanks Jing for your curiosity, your unique humor and your inspiring progress in Spanish (I finally admit your Spanish is better than my English ;-). Thanks Miquel for your little craziness we all would like to have and for sharing all your “interesting” stories. Thanks Berni for becoming a true friend in only 6 months and thanks for this little moment at the end of the Chrismas Party. Thanks Newsha for your little craziness we all would like to have and sharing all your “interesting” stories (it seems you fit with Miquel ;-).

Apart from the Pollitos&Pollitas team I had the pleasure to meet other beautiful PhD students. Sara thank you so much for being the sun everywhere you go. Ana I never met someone so generous, thanks for your always good words. Judit I will always remember our first congress, how lost we were then and how big the PhD seemed to us. David I remember that day when I wasn’t sure if it was appropriate to send you my CV. I did it and as answer you convince me to join the BBT and moreover, you convince the BBT to accept me. I will never thank you enough for the opportunity you gave me that day. I learnt a lot with you. Together with Yas you were my PhD fathers. Both of you made me a more confident and tolerant person, I hope one day I could help you as much as you helped me. Prya thank you for your contagious big smile. Mary thanks you for all the experimental tricks you gave me and our mutual help friendship, it was really useful for me.

The PhD and Marta gave me also the chance to transmit my experience and knowledge to master students: Joe, Marc, Daniel, Isa, Yago y Helena. Thanks to all of them for their works. Thanks Daniel for your implication and rigor, you will be a high-level researcher. Thanks Isa for your enthusiasm to work with us, even if we were not that lucky with the results. Thanks Yago for making the 3D stent challenge possible with your own style and thank you for believing in Kim deadlines ;-)

I was less time in Saarbrucken but there I had also the chance to meet beautiful persons. Thanks Michael for guiding my research in my first stay and for all your teaching on laser stuff. Thanks Shiqi for your unique friendship, for receiving me

at your place, for your Chinese food and for your laugh. Thanks Fede for being one of these persons who always ask how is everything going and try to find a way to help. Our friendship and your help made my stays in Saarbrucken a nice experience. Thanks Isabella for your funny vision of work and life. Thanks Seba for helping and for our sport discussions.

I would also like to thanks all my friends, who obviously contributed to my PhD in their own way. Particularly, I would like to thanks the ones living in Barcelona, who suffered sometimes my changing mood. Thank you Miguelito, for always being there to help me to escape from the PhD obsession. Thank you Vero and Marc, for understanding the difference between a “PhD thesis by papers” and a “PhD thesis by book” - or at least for trying to understand it ☺

Every climber would tell you that a good technique is not enough to be a strong climber… In other words “control is nothing without power”… And where does the power come from? It is time to talk about my family… My mother did, do and will do everything I need and at the same time she supports every decision I take… I can’t thank you enough Mamoon! On the contrary, my father, has sometimes difficulties to understand my strange and non-conformist decisions… but eventually he always accepts it and even contributes to the success of my crazy challenges… Le Pap thank you so much for all your unlimited support. Next comes my brother Victor… or Vic… or Vicou... or also we like to call him the perfect brother… because he always takes care of us… even if he is my little brother… even if sometimes it could be too much: at the end of my first PhD year, 2013, I told him that I started to write my first scientific paper, since then every time we talk I had the same question “Did you publish your first paper?”… Fortunately I finally published this paper… in 2017. Thanks Vicou for all your interest and support in all my projects. I do have another brother, Louis. He is not as perfect as Vicou… He is more about chaos and surprise… But nobody can ask more questions and enter dipper in your mind than he. His curiosity and his interest in his relatives life are inspiring and make you feel your insignificant life or your little project are so valuable and useful. Thanks Loulou for your complicity and for being my talisman.

As you have seen, all the way up to that terrific scientific mountains I have been very lucky to meet so many beautiful people, to believe in the robustness of my rope, to learn the technique from my colleagues, to be rescued by experts, to

share the experience with my friends, to use my natural power… But without my climbing partner I would probably not have summited these huge mountains… or even worst… Carmencita, she is the one on the other side of the rope since 10 years now and I feel so confident since then that I never untied my knot… I feel so confident since then that I decided to climb mountains that seemed unreachable before… the ones who met me before can attest that at that time my English and my Spanish sucked, I didn't want to live outside France, I had no professional ambition and even less the intention to do PhD… So Carmen, for being at my side, for inspiring me, for supporting me in all my projects and for making me a better person I thank you infinitely. I love you.

Abstract

Nowadays, cardiovascular diseases are mainly treated by implantation of a metallic or polymeric mesh, called stent, which maintains the artery widely open. This technique shows very good clinical results, however, it exists non-negligible cases of in-stent restenosis (ISR) and late stent thrombosis (LST) during the first year after stent implantation. These complications are mainly due to a delayed recovery of the endothelium after stent implantation, which also involves smooth muscle cells (SMCs) over-proliferation and platelets aggregation. Stent surface modification to modulate a specific cell lineage response has not been comprehensively explored. In particular, surface nano-topography, biofunctionalization or chemical features may be applied to increase endothelial cells (ECs) adhesion and/or migration, and to control platelet agglomeration.

The overall aim of this thesis was to obtain novel modified surfaces for stents implants with the ability to induce accelerated reendothelialization and controlled platelet aggregation in order to avoid ISR and LST. On CoCr alloy, as the gold standard material for bare metal stents (BMSs), two different strategies were evaluated, generation of linear patterns by direct laser interference patterning (DLIP) and, immobilization of biomolecules. On poly(L-lactic acid) (PLLA), as a material for bioresorbable stents (BRSs), endothelialization was enhanced by surface functionalization with NaOH etching, plasma treatment and cutinase enzyme hydrolysis.

CoCr alloy surfaces were successfully modified with a linear pattern of different periodicities and depths. Afterwards, Arg-Gly-Asp (RGD) and Tyr-Ile-Gly-Ser-Arg (YIGSR) peptides were covalently immobilized to the surfaces through silanization. Early ECs adhesion was improved on the peptide-functionalized surfaces, especially for YIGSR compared to RGD. High-depth nano-patterned surfaces generated ECs alignment within the topographical lines and enhanced ECs migration. Noteworthy, the combined use of both strategies, topography and biofunctionalization, synergistically accelerated the ECs migration and proliferation. Also, platelet adhesion and aggregation decreased in all patterned surfaces compared to smooth CoCr

probably due to changes in wettability and oxide layer characteristics. Cellular studies provided evidence of the potential of DLIP topographies and YIGSR biofunctionalization to foster endothelialization without enhancement of platelet adhesion, which will be of high importance when designing new stents.

Concerning polymeric biodegradable materials, PLLA films were obtained by solvent-casting in chloroform and, oxygen plasma, NaOH solution or cutinase enzyme treatments were used to functionalize the PLLA films and create surface hydroxyl and carboxyl groups without compromising biocompatibility. A higher amount of functional groups and an improved ECs adhesion was observed by oxygen plasma and cutinase enzyme hydrolysis compared to NaOH etching. Plasma or cutinase enzyme functionalized PLLA films presented a degradation rate similar to a peripheral commercial stent. Finally, 3D-printed PLLA BRSs were obtained by solvent-cast direct write technique. Consequently, the combined use of the solvent-cast direct write technique and plasma or enzyme functionalization holds a great potential to fabricate 3D-printed PLLA BRSs with the capacity to accelerate the surface endothelialization.

Overall, the present thesis offers a comprehensive view of the effectiveness of modifying CoCr alloys and PLLA films with specific topographies or functionalization strategies to enhance surface endothelialization while preventing restenosis and thrombosis.

Zusammenfassung

Heutzutage werden vaskuläre Erkrankungen hauptsächlich durch Implantation eines metallischen oder polymeren Netzes, genannt Stent, behandelt, welcher vormals verengte Arterien weit geöffnet hält. Diese Technik zeigt bereits sehr gute klinische Ergebnisse. Allerdings existieren auch nicht zu vernachlässigende Fälle von In-Stent Restenose (ISR) und späten Stentthrombosen (LST) im ersten Jahr nach Implantation des Stents. Diese Komplikationen entstehen hauptsächlich aufgrund einer verzögerten Erholung der Endothele nach Einsetzen des Stents, sowie durch übermäßiges Wachstums der vaskulären glatten Muskelzellen (SMCs) und einer Thrombozytenaggregation. Modifikationen der Stent-Oberfläche, um die Interaktion mit spezifischen Zellypen zu kontrollieren, sind noch nicht umfassend erforscht. Insbesondere können Oberflächen-Nano-Topographie, Biofunktionalisierung oder chemische Modifizierungen angewendet werden, um die Adhäsion und / oder Migration der Endothelzellen (ECs) zu erhöhen und die Agglomeration von Blutplättchen niedrig zu halten.

Das Gesamtziel dieser Arbeit war es, neuartige modifizierte Oberflächen für Stentimplantate zu entwickeln, die die Reendothelialisierung beschleunigen und eine Thrombozytenaggregation verringern, um ISR und LST vorzubeugen. Auf einer CoCr-Legierung, dem Gold-Standard-Material für unbeschichtete Metallstents (BMSs), wurden zwei unterschiedliche Strategien verfolgt; einerseits die Erzeugung linearer Muster durch direkte Laserinterferenzstrukturierung (DLIP) und Immobilisierung von Biomolekülen. Auf Poly (L-Milchsäure) (PLLA) als Material für bioresorbierbare Stents (BRSs) wurde die Endothelialisierung durch Oberflächenfunktionalisierung mit NaOH-Ätzen, mit einer Plasmabehandlung und mit Cutinase-Enzym-Hydrolyse verbessert.

Zum anderen wurden Oberflächen einer CoCr-Legierung erfolgreich mit einem Linien-Muster unterschiedlicher Periodizität und Tiefe modifiziert. Anschließend wurden Arg-Gly-Asp (RGD) und Tyr-lle-Gly-Ser-Arg (YIGSR) Peptide durch Silanisierung kovalent an den Oberflächen immobilisiert. Die frühe ECs-Adhäsion wurde auf den Peptid-funktionalisierten Oberflächen verbessert, insbesondere

für YIGSR im Vergleich zu RGD. Nanostrukturierte Oberflächen mit großer Tiefe erzeugten eine ECs-Ausrichtung innerhalb der topographischen Linien und förderten die EC-Migration und -Proliferation. Bemerkenswerterweise wurden diese synergetisch durch Kombination der zwei Strategien, Topographie und Biofunktionalisierung, beschleunigt. Auch die Thrombozytenadhäsion und –aggregation sanken in allen strukturierten Oberflächen verglichen mit glattem CoCr, möglicherweise auf Grund von Veränderungen der Benetzbarkeit und der Oxidschichteigenschaften. Zellstudien belegen das Potential von DLIP-Topographien und YIGSR-Biofunktionalisierung, um die Endothelialisierung ohne Erhöhung der Thrombozytenadhäsion zu fördern, was von großer Bedeutung bei der Entwicklung neuer Stents sein wird.

In Bezug auf polymere biologisch abbaubaren Materialien wurden PLLA-Schichten durch Solvent-Casting in Chloroform hergestellt. Sauerstoffplasma, NaOh-Lösemittel oder Cutinase-Enzym-Behandlungen wurden genutzt, um die PLLA-Schichten zu funktionalisieren und Oberflächen-Hydroxylgruppen und -Carboxylgruppen herzustellen, ohne die Biokompatibilität zu beeinträchtigen. Im Vergleich zu NaOH-Ätzen wurden durch Sauerstoffplasma und durch Cutinase-Enzym-Hydrolyse eine höhere Anzahl an funktionellen Gruppen und eine verbesserte ECs-Adhäsion festgestellt. Plasma- oder Cutinase-Enzym-funktionalisierte PLLA-Schichten zeigten eine ähnliche Degradation wie ein peripher, kommerzieller Stent. Abschließend wurden 3D-gedruckte PLLA-BRSs durch Solvent-Cast Direct Writing hergestellt. Folglich bietet die Kombination aus Solvent-Cast Direct Writing und Plasma- oder Enzymfunktionalisierung ein großes Potenzial, 3D-gedruckte PLLA-BRSs mit beschleunigter Oberflächenendothelialisierung herzustellen.

Insgesamt bietet die vorliegende Arbeit einen umfassenden Überblick über die Effektivität der Modifizierung von CoCr-Legierung und PLLA-Filmen mit spezifischen Topographien oder Funktionalisierungsstrategien zur Verbesserung der Oberflächenendothelialisierung bei gleichzeitiger Vermeidung von Restenose und Thrombose.

Resumen

Actualmente las enfermedades cardiovasculares están principalmente tratadas por implantación de una malla metálica o polimérica, llamada stent, que mantiene la arteria abierta. Esta técnica presenta muy buenos resultados clínicos, sin embargo, existen casos de reestenosis intra-stent (ISR) y trombosis tardia del stent (LST) durante el año que sigue la implantación. Estas complicaciones están principalmente debidas a una reparación demasiado lenta del endotelio después de la implantación del stent; que también implica una sobre-proliferación de células musculares lisas y una agregación de plaquetas. La modificación de la superficie del stent para generar una respuesta celular específica no ha sido explorada en profundidad. Particularmente, nano-topografía, biofuncionalización o modificaciones químicas pueden ser aplicadas para incrementar la adhesión y la migración de las células endoteliales (ECs), y para controlar la aglomeración de las plaquetas.

El objetivo global de esta tesis es de obtener nuevas superficies modificadas para stent implantes con la habilidad de inducir una endotelización acelerada y de controlar la agregación de plaquetas. Sobre CoCr, material de referencia para los stent metálicos desnudos (BMSs), dos estrategias diferentes fueron evaluadas, la creación de patrones lineales por la técnica Direct Laser Interference Patterning (DLIP) y, la inmovilización de biomoléculas. Sobre acido L-polilláctico (PLLA), como material para stent biodegradables (BRSs), la endotelización fue activada por funcionalización de la superficie vía tratamientos con NaOH, plasma o enzima cutinasa.

Patrones lineales de diferentes periodicidades y profundidades fueron obtenidos sobre superficies de CoCr. Después, los péptidos Arg-Gly-Asp (RGD) y Tyr-Ile-Gly-Ser-Arg (YIGSR) fueron enganchados covalentemente por silanización sobre les superficies de CoCr lisas y con patrones. La adhesión de ECs aumento sobre las superficies funcionalizadas, especialmente con el péptido YIGSR comparado con el RGD. Las superficies con patrones profundos generaron un alineamiento de las ECs con la dirección de las líneas del patrón y aceleraron la migración de esas mismas células. Además, el uso combinado de

esas dos estrategias, topografía y biofuncionalización, acelero sinérgicamente la migración y la proliferación de las ECs. Por fin, la adhesión y la agregación de plaquetas disminuyo sobre todas las superficies con patrones comparado con las superficies de CoCr lisas, efecto causado por los cambios de la capa de óxido introducido por la técnica DLIP. Los estudios celulares demuestran el potencial de las topografías DLIP y de la biofuncionalización para mejorar la endotelización sin aumentar la adhesión de plaquetas, lo que puede ser interesante a la hora de diseñar nuevos stents.

En cuanto a los stent biodegradables, películas de PLLA fueron obtenidas por la técnica de solvent-casting y, plasma de oxígeno, solución de NaOH o enzima cutinasa fueron utilizados para funcionalizar esas películas de PLLA y, así crear grupos hidroxilos y carboxilos en superficie sin comprometer la biocompatibilidad. Plasma de oxígeno y enzyma cutinasa generaron más grupos funcionales y mejoraron más la adhesión de ECs comparado con el tratamiento de NaOH. Además, las superficies de PLLA modificadas por plasma o enzima presentaron una degradación similar a la degradación de un stent comercial. Finalmente, BRSs de PLLA fueron obtenidos por impresión 3D vía la técnica de solvent-cast direct write. Consecuentemente, el uso combinado de esa técnica y de la funcionalización por plasma o enzima presenta un gran potencial para fabricar BRSs de PLLA impreso en 3D con la capacidad de acelerar la endotelización de la superficie.

En conclusión, esta tesis demuestra la efectividad de modificar las superficies de CoCr o PLLA con topografías específicas o con estrategias de funcionalización para mejorar la endotelización y paralelamente reducir los riesgos de trombosis y reestenosis.

Publication and other contributions

Publication

R. Schieber, F. Lasserre, M. Hans, M. Fernández-yagüe, M. Díaz-ricart, G. Escolar, M. Ginebra, F. Mücklich, M. Pegueroles, Direct Laser Interference Patterning of CoCr Alloy Surfaces to Control Endothelial Cell and Platelet Response for Cardiovascular Applications, *Adv. Healthc. Mater.* (2017). doi:10.1002/adhm.201700327.

Conference contributions

R. Schieber, S. Raymond, F. Mücklich, M. Pegueroles, 3D printed bioresorbable stents by solvent-cast direct-write technique, *2th Annual Conference European Society for Biomaterials*, 4th – 7th September 2017, Athens (Greece) – Oral presentation.

R. Schieber, D. Moreno, C. Mas Moruno, F.J. Gil, F. Mücklich, M. Pegueroles, Biofunctionalization of patterned PLLA surfaces with RGD, REDV and YIGSR peptides to promote endothelial cells adhesion and migration, *2016 TERMIS-EU Conference*, 28th June – 1st July 2016, Uppsala (Sweden) – Poster presentation.

R. Schieber, D. Moreno, C. Mas Moruno, F.J. Gil, F. Mücklich, M. Pegueroles, Biofunctionalization of patterned PLLA surfaces with cell adhesive peptides to promote endothelial cells adhesion, *XXXVIII Congreso de la Sociedad Ibérica de Biomecánica y Biomateriales*, 6th – 8th November 2015, Barcelona (Spain) – Poster presentation.

D. Moreno, **R. Schieber**, F.J. Gil, M. Pegueroles, Functionalization of patterned PLLA surfaces with cell adhesive peptides to promote endothelial cells adhesion and migration*, I Seminar of Nanosurfaces: Advanced Processing and Characterization – II International Seminar on Biomaterials, Biomechanics and Regenerative Medicine*, 16th - 18th September 2015, Medellin (Colombia) – Poster presentation.

R. Schieber, D. Moreno, C. Mas Moruno, M. Hans, M. Díaz-ricart, G. Escolar, F.J. Gil, F. Mücklich, M. Pegueroles, Surface endothelialization and non-thrombogenic strategies for cardiovascular applications, *8th EEIGM International Conference on Advanced Materials Research*, 11th – 13th June 2015, Valencia (Spain) – Oral presentation.

R. Schieber, M. Fernández-Yagüe, M. Hans, M. Díaz-ricart, G. Escolar, F.J. Gil, F. Mücklich, M. Pegueroles, Endothelization and thrombogenicity response of CoCr alloy nano depth patterns for cardiovascular stents, *26th Annual Conference European Society for Biomaterials*, 31st august – 3rd september 2014, Liverpool (United Kingdom) – Poster presentation.

R. Schieber, M. Fernández-Yagüe, M. Hans, F.J. Gil, F. Mücklich, M. Pegueroles, Patterned CoCr alloy by Laser Interference Surface Structuring for cardiovascular applications, *XIII Congreso Nacional de Materiales*, 18th – 20th June 2014, Barcelona (Spain) – Oral presentation.

R. Schieber, M. Hans, M. Fernández-Yagüe, F.J. Gil, F. Mücklich, M. Pegueroles, Laser interference surface structuring of CoCr alloy to endothelize cardiovascular stents, *XXXVI Congreso de la Sociedad Iberica de Biomecenica y Biomateriales (SIBB),* 25th – 27th october 2013, Granada (Spain) – Oral presentation.

Scholarship

Pre-doctoral grant Erasmus Mundus Joint Doctorates – European Joint Doctoral Programme in Materials Science and Engineering (DocMASE), European Comission from European Union. October 2012 – September 2016.

Table of Contents

Glossary of terms

BMS bare metal stent

BRS bioresorbable stent

CoCr cobalt-chromium

CPTES 3-chloropropyltriethoxysilane

DES drug eluting stent

DLIP direct laser interference patterning

E Young’s modulus

EC endothelial cell

FDA food and drug administration

FIM first-in-human study

HUVEC human umbilical vein endothelial cell

IRS in-stent restenosis

LST late stent thrombosis

NaOH sodium hydroxide

PLLA poly(L-lactic acid)

RGD (Arg-Gly-Asp)

SMC smooth muscle cell

UTS ultimate tensile strength

YIGSR (Tyr-Ile-Gly-Ser-Arg)

Chapter I: Introduction

Cardiovascular diseases is one of the leading causes of mortality and morbidity in the world [1]. According to the World Health Organization (WHO), 17.3 million people died from cardiovascular related diseases in 2008, and this number is projected to rise to an estimated 23.6 million by 2030 [2]. Age and bad habits like smoking, sedentary lifestyles, or fat diet are a major factor in cardiovascular problems.

Cardiac events like heart attack or cerebrovascular accidents are mainly caused by the formation of an artherosclerotic plaque in the artery wall which eventually blocks the blood flow preventing the delivery of oxygen and nutrients to the body. The main cardiovascular disease is atherosclerosis, which consists in an accumulation of lipids and cholesterol in the artery wall leading to a reduction of the artery inner section, also called stenosis. The evolution and rupture of the atherosclerotic plaque and the endothelium leads to the formation of thrombus, also called thrombosis.

Nowadays, cardiovascular diseases are mainly treated by implantation of a metallic or polymeric mesh, called stent, which maintains the artery widely open [3]. This technique shows very good clinical results however, it exists non-negligible cases of in-stent restenosis (ISR) and late stent thrombosis (LST) during the first year after stent implantation [4]. These complications are mainly due to a delayed endothelium reconstruction after removal of the endothelium during stent implantation which also involves SMC over-proliferation and a platelet aggregation. The cardiovascular research is focused in improving stents by optimizing stent characteristics: design, material, drug delivery, surface coatings… However, few studies have been done on stent surface modification in order to modulate a specific cell lineage response.

The overall aim of this thesis was to obtain novel modified surfaces for stents implants with the ability to induce accelerated reendothelization and controlled

platelet aggregation in order to avoid ISR and LST. In the present introduction, the scientific context is explained, as well as the medical problem, the stent solution, the stent biomaterials and the possible surface modifications to reach the presented aim.

1. Endothelialization

1.1. Definition

Endothelialization is the formation of endothelial tissue. A healthy endothelium, the inner layer of the artery in contact with blood, is composed of a monolayer of endothelial cells (ECs) and it has antithrombogenic properties, among others. Consequently, endothelialization is an extremely important process expected to occur as soon as possible when the endothelium is damaged.

1.2. Artery structure

Arteries are blood vessels that carry oxygenated blood away from the heart to supply the body with oxygen. The native artery is an extremely complex multi-layered tissue composed of many proteins and cell types, each playing a crucial role in the mechanical and biological behavior of the structure. An artery is composed of three major layers as seen on **Figure I.1**:

- ***Tunica intima*** *or* ***Endothelium***, is the innermost layer of the vessel wall and it contains elastic and connective tissue. A monolayer of endothelial cells is in contact with the hollow internal cavity in which the blood flows, the lumen. As the cellular interface between the circulating blood and the vessel wall, the endothelium main function is to avoid blood coagulation through the production of molecules with antithrombotic properties, including nitric oxide, prostacyclin, tissue plasminogen activator, thrombomodulin, heparin-like molecules, and tissue factor pathway inhibitor [5]. Moreover, the healthy endothelium permeability is also crucial to provide a barrier between the artery lumen and surrounding tissue, to keep the blood inside the artery and, at the same time, allows the exchange of nutrients with the interior of the tunica media [6,7].
- ***Tunica media***, is composed of elastic tissue and several layers of smooth muscle cells (SMCs) in a matrix of collagen types I and III, elastin and proteoglycans. In the largest arteries, as the aorta, the amount of elastic

tissue is very considerable. The muscle fiber cells are arranged in 5 to 7 layers of circular and longitudinal SMCs of about 50 µm length [8,9].

- ***Tunica adventitia*** *or* ***Tunica externa***, is the most external layer composed of connective tissue with fibroblasts, microvascular networks and randomly arranged collagen type I [10,11].

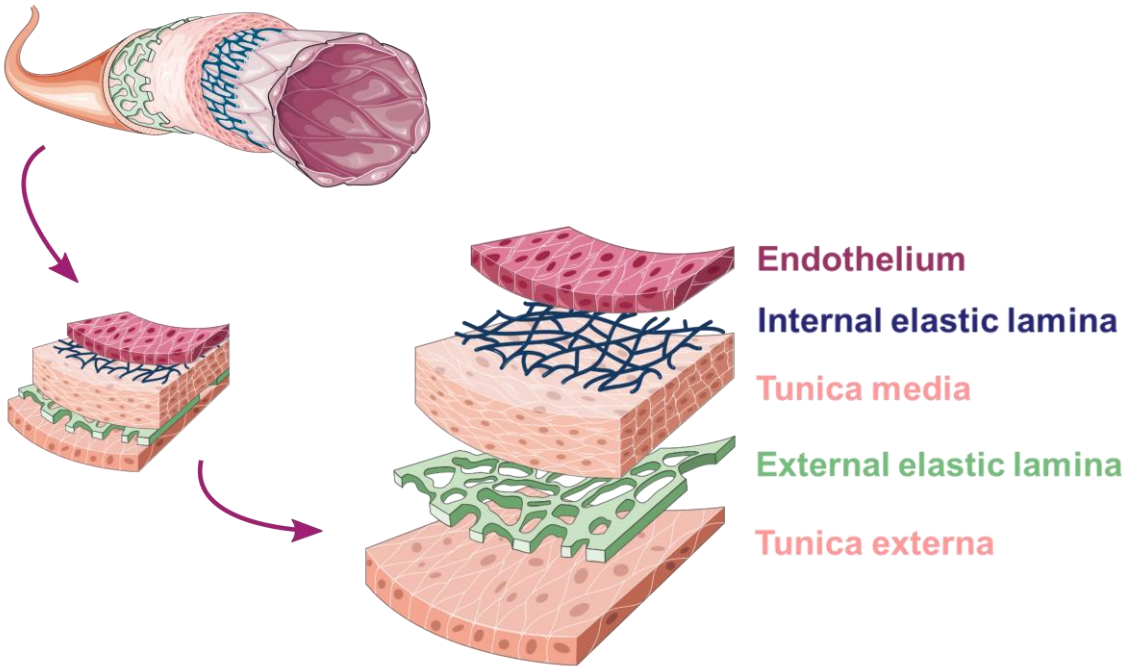

Figure I.1*: Schematic views of the functional artery with its three major layers: endothelium, tunica media and tunica externa.*

1.3. Cardiovascular diseases

Cardiovascular diseases are mostly caused by **atherosclerosis**, which is a physiologic phenomenon beginning at the embryonic stage and evolving with arteries ageing. This disease is related to genetic predisposition and lifestyle.

Adhesion of circulating monocytes to the surface of the endothelium appears to be an early event in the development of atherosclerotic lesions. Next, they insinuate through the endothelium and are transformed into macrophages, which ingest lipids and form fatty deposits [12]. Meanwhile, a number of molecular factors, like platelet adhesion, generate proliferation of SMCs in the intima. Monocytes, lipids, platelets, SMCs, and fibrous connective tissues form an inflammatory plaque called atheroma (**Figure I.2**). Finally, atherosclerosis can generate two main complications:

- **Stenosis**, which is the long-term evolution of atherosclerosis due to a slow growth of the atheroma plaque leading to final obstruction of the artery.
- **Thrombosis**, which is a quick and acute complication corresponding to the rupture of the endothelium and/or the atheroma plaque. This rupture exposes the collagen of tunica intima connective tissues to the bloodstream [13]. On contact with collagen, platelets become activated. Platelet activation induce several thrombogenic event like platelet adhesion and aggregation [14]. Finally, a thrombus is formed which can obstruct the artery or detach and obstruct another vessel.

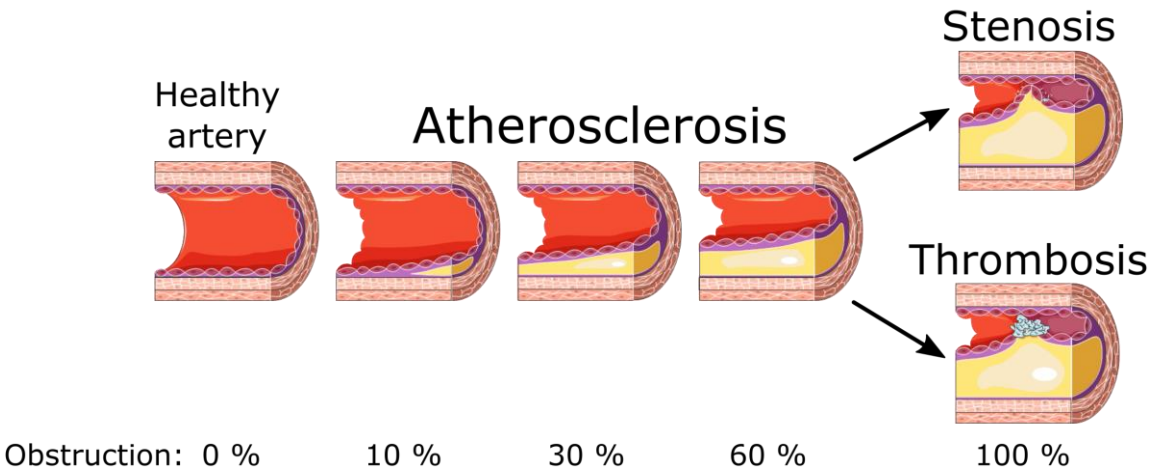

***Figure I.2**: Schematic representation of a portion of artery in a healthy state, with atherosclerosis disease progress at different stages, resulting in stenosis and/or thrombosis.*

1.4. Stents

In the 70' coronary diseases were healed by Coronary Bypass Graft Surgery consisting in removing the occluded section of the artery and replacing it with a healthy conduct by performing a coronary bypass. But this open chest surgery is an invasive method which is therefore heavy and complicated. Also, as it requires the chest wall to be cracked open, it can easily lead to infections.

The advent of **percutaneous transluminal coronary angioplasty** in 1977 provided a fundamental change in the treatment of coronary artery diseases [1]. **Angioplasty** is the technique of mechanically widening narrowed or obstructed arteries. **Percutaneous surgery**, also called "non-invasive" surgery means that the surgery is done through the skin instead of doing open chest surgery. It consists in doing a small incision in the patient's skin at the level of an artery.

Then a catheter is inserted through the incision in the vascular system. These catheters are hollow flexible tubes for insertion into a body vessel to distend a passageway for other medical tools. Unlike the traditional open heart surgery, the heart does not need to be arrested during the procedure.

Non-invasive surgery has been used since 40 years with the first human coronary balloon angioplasty performed intra-operatively in 1977 by Gruentzig, Myler and Hanna in San Francisco [1]. It consisted in the enlargement of the stenosed coronary artery thanks to a balloon inflated in the atherosclerosed artery portion (**Figure I.3**).

Rapidly the coronary balloon angioplasty will be replaced by the use of coronary stent. Stent are mesh implanted in the diseased arteries to hold it open to a predetermined diameter (**Figure I.3**). In 1982, appeared the first patent, by Hans Wallsten, concerning a self-expandable metallic braided stent called Wallstent (Boston Scientific, United States) [15]. The first implantation of the Wallstent in human coronary position is done by J. Puel in 1986 [15].

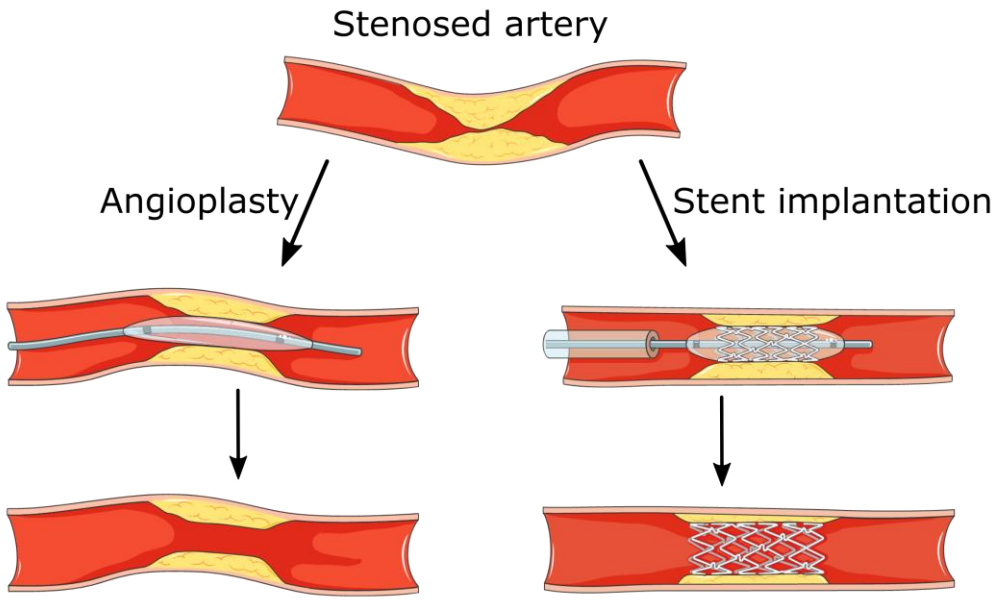

***Figure I.3**: Non-invasive coronary surgery on a stenosed artery: angioplasty on the left and stent implantation on the right.*

Vascular stents represent today one of the main application of percutaneous technology. Its popularity arises due to its less invasive nature (compared to surgical alternatives) and its better clinical outcome (compared to balloon angioplasty) [16,17]. The use of stents for all applications has dramatically increased

since their approval by the United States Food and Drug Administration (FDA) in 1994, largely as a result of therapeutic and technological advances. In 2010, in the United States, an estimated of 492 000 patients underwent percutaneous transluminal coronary angioplasty in the United States and the stent market reach $5 billion per year [18].

1.4.1. Stent properties

Endovascular stents are expandable meshes that range from 6 to 60 mm in length and from 2 to 10 mm in diameter, most commonly made from stainless steel, chromium-cobalt alloy, the nickel-titanium alloy Nitinol, although tantalum [19], platinum [19], plastic [20], and biodegradable materials [21,22] have also been used. In a compressed state the stent is mounted on a catheter and threaded through the vascular tree to a site of narrowing. The stent is next enlarged in diameter approximately 50%, either by a spring-like recoil into their naturally expanded shape (e.g. Nitinol) or by plastic deformation under the influence of a cylindrical balloon inflated within the stent to 8-20 atmospheres of pressure. Once the catheter is withdrawn the stent is left within the artery.

As the stent's main function is to compress the atheroma, stent should present high mechanical properties as high Young's modulus (E) or high ultimate tensile strength (UTS) (**Table I.1**). As for all implant, stent materials should be biocompatible and corrosion resistant in body conditions.

Table I.1: *Stent required characteristics and associated biomaterials properties. E: Young modulus; UTS: Ultimate tensile strength*

Stent necessary properties	Description	Associated biomaterials properties
High scaffolding	Ability to provide strong mechanical support to the vessel wall	High E
High expansion ratio	The material should undergo sufficient expansion and conform to the vessel wall	High UTS
Excellent corrosion resistance	Ability to prevent corrosion induced by formation of oxide films	No prejudicial corrosion in body conditions
Good biocompatibility	Material must be biocompatible so as to not elicit an adverse reaction from the body	Low % of complications in the clinical studies
Thrombo-resistivity	The material should be blood compatible and not encourage platelet adhesion and deposition	Low % of thrombosis in the clinical studies
Inexpensive to manufacture	The material should be cost-effective to purchase	Cheap and easy-to process

1.4.2. Stent evolution

1.4.2.1. Bare metal stent (BMS)

BMS, which is an expandable tube of metallic mesh, was introduced in 1986. BMS provides a mechanical scaffold to widely open the narrowed artery, to prevent artery elastic recoil and negative remodeling. However, besides crushing the atheroma plaque, stent deployment destroys partially and disrupts the endothelium [23], triggering an over-exposure of collagen, SMCs, fibronectin and laminin to the blood flow; and consequently generating a cascade of thrombogenic events allowing the platelets to aggregate. This is the initial point of the thrombus formation, creating a wall injury that presents clot formation where the macrophages get attracted due to the metallic foreign surface. Finally, it occurs an uncontrolled proliferation and migration of SMCs to the intima leading to the re-narrowing of arteries called in-stent restenosis (ISR) [19,24,25]. As a consequence of this cascade of biological events, it can be observed early thrombosis, 1 to 3 % the 10 first days [15] and mostly ISR during the first year after stent implantation [3] (**Figure I.4**). However, when compared with balloon angioplasty, BMS significantly reduces the ISR rate from 50 % to 20 – 30 % [3,16,21].

1.4.2.2. Drug Eluting Stent (DES)

In addition to acting as a vascular scaffold, stents soon evolved to become drug delivery systems in the form of DES. DESs are composed of a metallic stent covered by a polymer which contains a pharmacologic agent. They allow a local drug release to the artery wall. These drugs include anti-inflammatory, anti-proliferative and anti-migratory agents. The goal of DES technology is to minimize vascular inflammation and SMCs proliferation, in order to reduce ISR. Early trials of different DESs demonstrated markedly reduced rates of ISR from 20 – 30 % to 5 – 10 % [26–29], heralding the DES revolution that followed. Although DESs reduce ISR, the liberation of anti-proliferative drugs also induce a delayed reendothelialization and, consequently, increased the risk of LST occurring more than one year after stent implantation [30–32]. Some studies, identified a rate of late stent thrombosis (LST) as high as 9.4% [33]. Consequently, continuation of dual-anti-platelet therapy is required for one or more years after DES placement.

1.4.2.3. Bioresorbable Stent (BRS)

The interest of a BRS is to have a temporary stent that bioabsorbs with time allowing the vessel to recover its natural shape and function. BRS are an alternative for the currently-used permanent cardiovascular stents as it has been shown that the effect of stents is temporary and limited to a period of 6 to 12 months after intervention during which arterial remodeling and healing occur [34]. The advantages of BRS in front of DES are the stent fully degradation in 12 to 24 months, among others:

- A reduction in adverse events such as LST [35,36].
- The return of vessel vasomotion, adaptive shear stress, late luminal enlargement, and late expansive remodeling [37].
- A reduction in bleeding complications and consequently no requirement for long-term dual antiplatelet therapy.
- Elimination of the concern that some patients have of having an implant in their bodies for the rest of their lives [38].

It's worth mentioning that actual research on BRS is developing stents with a polymeric coating containing pharmacologic agents.

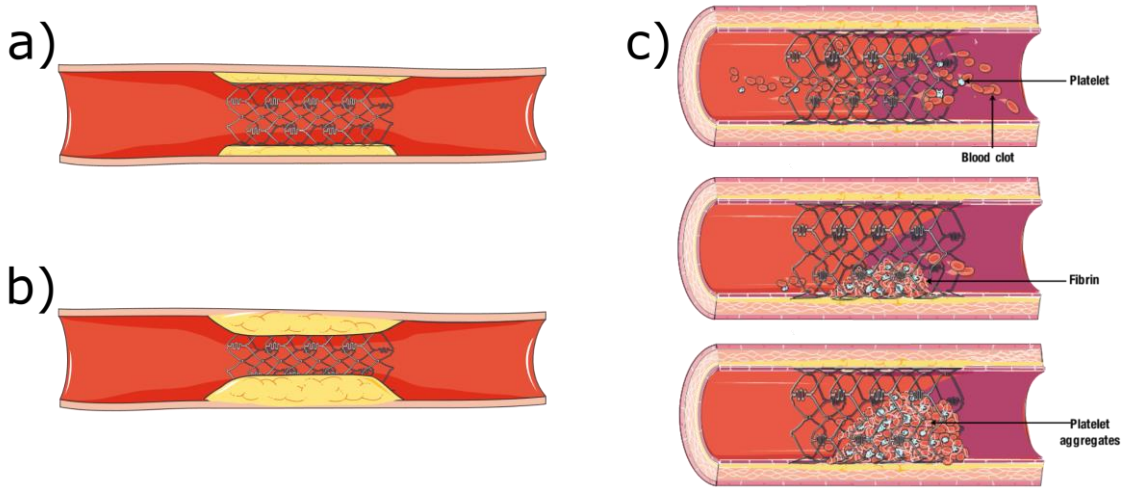

***Figure I.4**: Complications after stent implantation. (a) Section of artery just after stent implantation. (b) ISR due to stent implantation. (c) Different stages of stent thrombosis.*

1.4.3. Stent next generation

BMS, DES and BRS main characteristics are summarized in **Figure I.5**. Fully biodegradable stent seems to be the ideal compromise to, first, induce the artery to recover its structure and functionality and, secondly, to avoid ISR or LST

generated by the presence of permanent BMS or DES. However, BRS are very new devices and the Food and Drug Administration (FDA) waited to July 2016 to approve the first BRS for coronary artery, the Absorb GT1 (Abbott, United States). At April 2017 Abbot restricted the use of Absorb GT1 in Europe due to some cardiac events related to the implantation of this BRS. Moreover, in tortuous section of the artery, there is higher mechanical stress due to blood flow modification. In these portions of arteries it would be risky to use BRS due to its mechanical properties deterioration with biodegradation. Thus, permanent stent will continue being implanted for several years or decades. Generally, BMSs have a higher incidence of ISR whereas DESs have a higher frequency of LST. Then, the surgeon select one of the two according to the cardiovascular disease specificity. In conclusion, we believe that in the short and medium term no one will be discarded, stent implantation will be done with BMS, DES or BRS according to the medical cases.

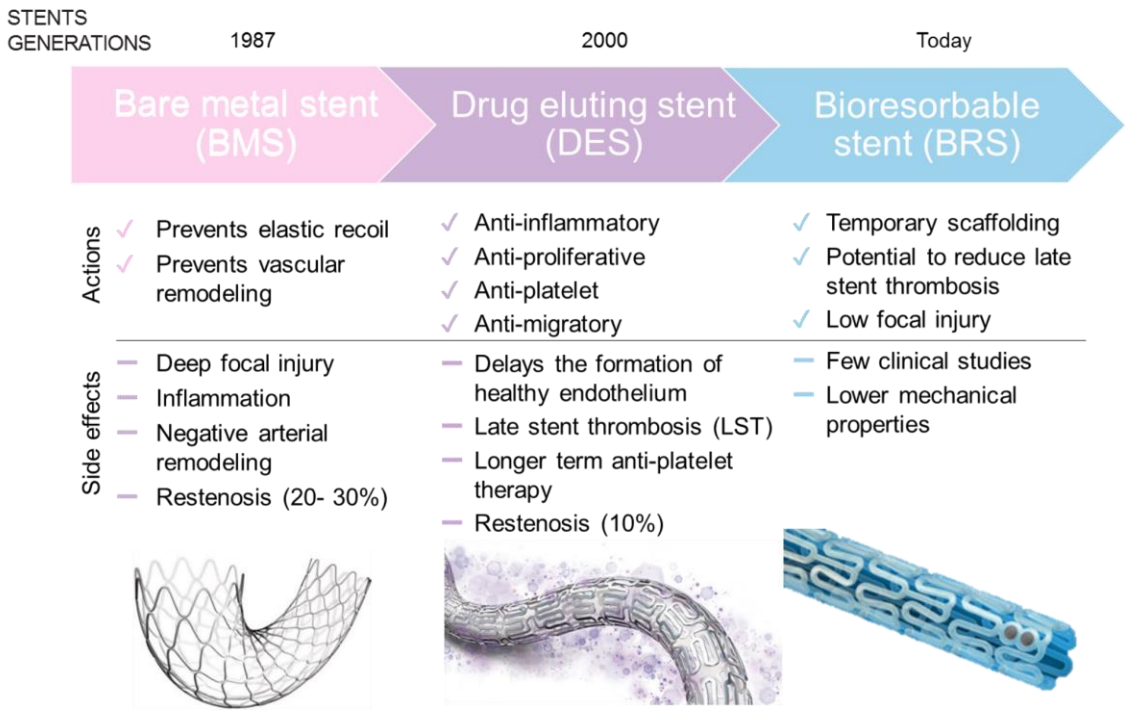

***Figure I.5**: Stent generations and its mains characteristics. Modified from [39].*

2. Biomaterials for stents

2.1. Cobalt-chromium (CoCr) alloy for stents fabrication

2.1.1. Metals for stents

As the main objective of the BMS was to counter the negative effects of the balloon angioplasty, it should address properties such as rigidity for maintenance of dilatation and resistance to elastic recoil, elasticity or plasticity for expansion, corrosion resistance, radiopacity and radial strength [15].

Therefore, from the viewpoint of mechanical properties, it is natural that stents are made of metals. The metallic materials most currently used for coronary stents are 316L stainless steel (SS), cobalt chromium (CoCr) alloys and titanium alloys [40–42].

Stainless Steel

SS is a steel alloy with a minimum of 12-13 mass % of Cr. The main reason for the use of SSs is the good balance between strength (E ≈ 193 GPa) and elongation, which facilitates the manufacture of the stent, the plasticity for the balloon expansion, and the maintenance of geometry to resist the elastic recoil of blood vessels. Most metal stents are made of austenitic SS 316L. SSs do not corrode in an oxygen-containing atmosphere, but they corrode locally and sometimes form pits in chloride solutions as found in some body fluids. Type 316L SS shows pitting and crevice corrosion when implanted in the human body [43,44].

Nickel-titanium alloy (Nitinol)

The nickel-titanium (NiTi) alloy, also known as Nitinol, is a metal alloy with an approximately equiatomic composition of titanium (Ti) and nickel (Ni) (49-51 mol % of Ni) and shows unique mechanical properties such as shape memory, and superelasticity. Shape memory effect gives NiTi the ability to be deformed at one temperature, and then return to its original shape when being heated to its transformation temperature. Superelasticity occurs at specific temperature and allows the material to recover to its original shape after an apparent plastic deformation as soon as the stress is removed. Because of these unique properties, the NiTi alloy is used to fabricate guide wires, stents, orthodontic arch wires, and endodontic reamers, among others. The SMART

stent (Cordis, United States) and Radius stent (SciMED Live System, United States) are examples of NiTi BMSs currently used. However, the NiTi alloy usually exhibits crevice corrosion and pitting, and it corrodes during service in aortic endografts, where pitting and craters are observed on the alloy [45].

2.1.2. CoCr alloys

CoCr alloys show high strength, toughness, castability, corrosion resistance, and wear resistance. CoCr alloy was initially used as a cast alloy because working it is difficult due to its high hardness. The Wallstent, is made of Elgiloy, a 40Co-20Cr-15Ni-7Mo-Mn alloy that was developed as a heat-resistant alloy. For biomedical use, cast Co–Cr–Mo alloys, commonly known as Vitallium alloys family, resist pitting and crevice corrosion. Because of the carbide in its structure, CoCr alloys have excellent wear resistance and are used for sliding parts of artificial joints.

Wrought CoCr alloys, which are used for stents, were designed to avoid cast defects in cast CoCr alloys. The strength and elongation of wrought CoCr alloys, which increase with heat treatment and cold working, are as high as those of SS. The corrosion resistance of the wrought CoCr alloy is lower than that of cast CoCr alloy, but higher than that of SS. Therefore, wrought CoCr alloy is used for guide wires, clips, orthodontic arch wires, and catheters.

Mainly, for the corrosion resistance properties, it has been decided to select CoCr alloy ASTM F90 to study metallic surface modification for cardiovascular applications. This alloy is a wrought 51Co-20Cr-15W-10Ni alloy for surgical implant applications. It has a Young's modulus of 210 GPa and a unique ability to resist corrosion in very severe environments [46–48].

2.2. Poly(L-lactic acid) (PLLA) for stents fabrication

2.2.1. Biodegradable materials for stents

DESs are made of a metallic core, generally CoCr alloy, stainless steel or Nitinol, covered by a polymeric coating containing drugs. Permanent polymer were used for the first DES generation [21,49–51]. Next, biodegradables polymers coating were developed to reduce the long-term risks associated with the presence of a permanent polymer [16]. These materials offer the attractive combination of controlled drug elution in parallel with biodegradation of the polymer into inert

monomers. **Table I.2** shows DESs biodegradable materials used as coating, its mechanical properties and its observed clinical advantages and disadvantages.

Few biodegradable polymers have been used for DESs coating: poly(lactic acid) (PLA), poly(lactic-co-glycolic acid) (PLGA), polycaprolactone (PLC) and polyvinylpyrrolidone (PVP). Among them, only DESs with a PLA have been approved by the European Union (EU) with a Conformité Européenne marquage (CE mark). All the other DESs are under First-In-Man (FIM) or recent clinical studies.

The polymers use for the SIMPLE II coating, a copolymer of PLC and PVP, induced non satisfactory clinical results and cannot be use for BRS because of its low mechanicals properties. The copolymers used for the Supralimus and Infinium coating was synthesized especially for this application and its properties are confidential.

All the PLA coating show better clinical results than BMSs, including few LST and a better endothelial recovery. Finally, PLA have the highest mechanical properties, suggesting it could be also the best candidate for BRSs.

Table I.2: *Mechanical properties and clinical results of biodegradable polymers used as coatings for DESs. PLC: polycaprolactone; PVP: polyvinylpyrrolidone; PLGA: poly(lactic-co-glycolic acid); PLA: poly(lactic acid); E: Youngs modulus; UTS: ultimate tensile strength; Tg: glass-transition temperature; FIM: first-in-man study; late loss: reduction of the lumen diameter in the 6 months after stent implantation.*

DESs	Polymers	State of investigation	Clinical advantages	Clinical disadvantages	Mechanical properties	Ref.
Simple II	**PLC / PVP**	FIM ; not approved		Average rate of in-stent angiographic restenosis and average late loss	PLC properties: E = 30-200 MPa; UTS = 20-40 MPa Tg = -61ºC	[3,52]
Nevo stent	**PLGA**	Recent clinical studies; not approved	Satisfactory binary ISR rates and in-stent late loss		E = 1-4 GPa; UTS = 41,4-55,2 MPa	[53,54]
Biomatrix stent	**PLA**	CE mark	Few LST events; near complete endothelial recovery (>95%)		UTS= 15-150MPa; E = 2,7-4,14 GPa	[53,55]
NOBORI	**PLA**	CE mark	Significantly better endothelial recovery than BMSs		UTS= 15-150MPa; E = 2,7-4,14 GPa	[53,56]
Axxess	**PLA**	CE mark	At 6-month follow-up, in-stent late loss was 0.09 mm	80% and 42% of patients, respectively, required 2 or 3 additional stents to cover the lesion	UTS= 15-150MPa; E = 2,7-4,14 GPa	[53,57]
XTENT	**PLA**	CE mark	CoCr structure; modular design made up of multiple 6-mm segments that were interdigitated		UTS= 15-150MPa; E = 2,7-4,14 GPa	[53,57]
JACTAX	**PLA**	Recent clinical studies; not approved			UTS= 15-150MPa; E = 2,7-4,14 GPa	[53,57]
Supralimus and Infinnium stent	**Copolymer (confidential)**	FIM ; not approved	Rate of in-stent angiographic restenosis of 0.0%; low late loss			[50,53,58]
Synergy stent	**PLGA**	Recent clinical studies; not approved		target lesion failure at 30 days	E = 1-4 GPa; UTS = 41,4-55,2 MPa	[53,57]

Table I.3: *Mechanical and degradation properties and clinical results of biodegradable polymers used for BRSs. PLLA: poly(L-lactic acid); PDLLA: poly(D,L-lactic acid); E: Young's modulus; UTS: ultimate tensile strength; FIM: first-in-man study; late loss: reduction of the lumen diameter in the 6 months after stent implantation; MACE: major adverse cardiac events; TLR: target lesion revascularization.*

BRSs	Polymers	Stat of investigation	Clinical advantages	Clinical disadvantages	Properties	Ref.
IGAKI-TAMAI stent	**PLLA**	Long human studies (more than 10 years); CE mark for peripheral arteries since 2007	Non-drug eluting (PLLA without drug); a low complication rate; survival rates free from death, cardiac death, MACE, and TLR were 89%, 98%, 60%, and 76%, respectively.	Concern has arisen about the ability to apply heat, to self-expand the stent, without causing possible necrosis of the artery wall.	UTS= 15-150MPa; E = 2,7-4,14 GPa; Degradable in 18-24 month.	53,57,59
Paclitaxel-eluting PLLA	**PLLA**	Non-human studies; not approved	reduced proliferation and stenosis after vascular intervention		UTS= 15-150MPa; E = 2,7-4,14 GPa	53,60
ABSORB GT1	**PLLA (and a PDLLA coating with evrolimus inside)**	CE mark for coronary arteries since 2011; FDA approval in 2016	reduced in-stent late loss and a low MACE rate of 4.4%; few acute vessel recoil; no LST has been observed out to 3 years follow-up		UTS= 15-150MPa; E = 2,7-4,14 GPa Degradable in 24 month; radial support during 3 months	35,36,53
REVA stent	**Tyrosine polycarbonate**	FIM; not approved	Improve acute recoil; minimal vessel shrinkage at follow-up	Mechanical failure led to a higher than anticipated rate of target lesion revascularization	Radio opaque; degradable in 36 month; radial force comparable to a BMS	61,62
IDEAL BDS	**Poly(anhydride ester) (salicylic acid)**	FIM; not approved	Successful results in pig coronary arteries; in human trials, absence of acute or chronic recoil; reduction in inflammation compared to BMS.	Insufficient neointimal inhibition due to inadequate drug dosing and very quick elution of Sirolimus.	Degradable in 12 months; radial strength greater than BMS; resistant to gamma radiation	19,63

Table I.3 shows developed BRS, being all of them approved or under clinical trial. Tyrosine polycarbonate, used for the REVA stent, got correct FIM study results. However, it presents mechanicals failure associated with a too long polymer degradation and too recent studies. For these reasons it is preferable not to use tyrosine polycarbonate.

Poly(anhydride ester) (salicylic acid), used for the IDEAL BRS, shows successful results in human trials, particularly an absence of acute or chronic recoil and a reduce inflammation compared to BMSs have been reported. This is the result of its high radial strength and its appropriate degradation rate. Also, the presence of salicylic acid in the polymer backbone permit to release drug without introducing drug inside the polymer. Insufficient neointimal inhibition is the only defect of this biodegradable polymer.

2.2.2. PLLA

PLLA and poly(D-lactic acid) (PDLA) are two different stereosisomers of PLA. For BRSs, PLLA has been chosen mainly for its higher crystallinity (about 37%) and, therefore, its higher mechanical properties (E = 3 GPa and UTS = 15-150 MPa; **Table I.4**).

A semi-crystalline polymer (PLLA) is obtained from L-lactide.The special interest on PLLA to fabricate BRS is probably due to the fact that it is the biodegradable polymer with the highest mechanical properties [64]. Also, among all biodegradable polymers, it has the slowest degradation rate [65], and, when obtained with a high molecular weight, it has been shown to take up to 5 years to be completely resorbed in vivo [66,67]. PLA undergoes thermal degradation at temperatures above 200ºC mainly by hydrolysis, however, lactide reformation, oxidative main chain scission, and inter- or intra-molecular transesterification reactions also occur [68]. PLA degradation is dependent on time, temperature, low-molecular-weight impurities, and catalyst concentration [68]. Also, PLLA used for BRSs have shown satisfactory clinical results, like particularly few major adverse cardiac events (MACE) and few thrombosis complication. Among them, the ABSORB GT1 is approved by the UE and the FDA for coronary arteries.

To conclude, PLLA has already been used in many DESs and BRSs, it has all the mechanical and degradation properties necessary for the application and, it

presents multiples clinical studies with good results (**Table I.4**). Furthermore, the only two certified BRS are made of PLLA.

Table I.4: *Properties and clinical results of PLLA used in stent application.*

Stent necessary properties	Optimum value	PLLA
High scaffolding	Highest E	3 GPa
High expansion ratio	Highest UTS	15-150MPa
Excellent corrosion resistance	No corrosion before degradation	Yes
Good biocompatibility	Good clinical results; few complication post stent implantation	low complication rate; reduced in-stent late loss; low MACE rate of 4.4%; few acute vessel recoil
Slow degradation	Best time of polymer degradation: 12 months	12-24 month
Thrombo-resistivity	No thrombosis	Few thrombosis cases
Inexpensive to manufacture	Cheap; easy-to process; easy-to buy	Really well-known polymer; a lot of studies for stent application; not specially expensive

3. Surface modification

Surface properties of the implant are of great importance whenever it is implanted into living tissue. Biological interactions between the host tissue and the implant are mainly taking place at the surface of the device. The substrate surface can be designed to prevent or promote cell growth, stimulate or prevent blood clothing, attract or reject specific proteins, or in some other way control the biological response.

Numerous investigations have been conducted to optimize surface implant biocompatibility and, at the same time, to obtain a bioactive surface. In cardiovascular field, an implant is bioactive if it induces reendothelization, reduces SMC proliferation or platelet aggregation. Consequently, main complications after stent implantation, ISR and LST, should be avoided. The most common approaches to achieve such materials are (**Figure I.6**):

- Topographical modification to obtain specific isotropic roughness or nano-micro patterns [19].
- Chemical modification in order to modulate surface functional groups, surface energy or surface electrostatic charge (NaOH etching, cold plasma, ozone, UV, among others) [19].

- Biofunctionalization of surface by immobilization of specific biomolecules which facilitates or activates a cascade of biological events and, eventually regenerates or replaces functioning tissue [69].

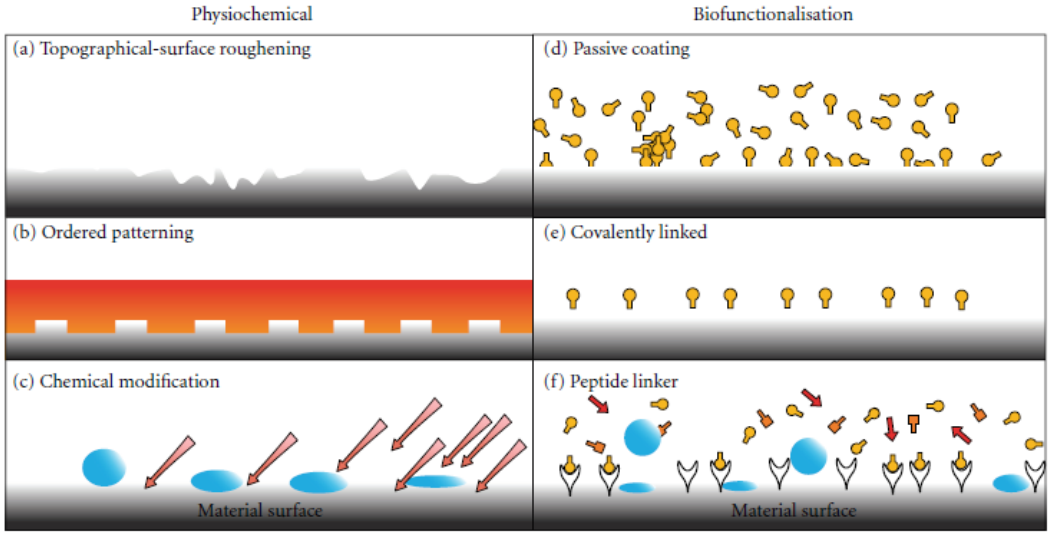

***Figure I.6**: Examples of various physical, chemical, and biofunctionalization techniques to enhance hemocompatibility. Biofunctionalized surfaces interact with cell surface receptors, which are integrins. Whereas physiochemical modification can influence cell-material interactions through charge, topography, and attractive/repulsive forces due to hydrophobic and hydrophilic interactions [69].*

3.1. Topography

3.1.1. Cell response to topography

Surface roughness and texture of implants is known to influence biological response. Topography on the micro- and nano-metric scale is an important physical property, which influences protein adsorption, platelet adhesion, thrombogenicity, and cell behaviour. Originally, studies have suggested that a rough surface is more prone to thrombogenicity [70–72] and thus, surface treatments were essential to obtain a contamination-free and smooth surface for stent material applications. To obtain such stent surfaces various surface treatments are used, including mechanical polishing, electropolishing, ultrasonic cleaning, chemical etching and degreasing, as well as low-pressure plasma etching [73]. Electropolishing possesses several compelling advantages that render it the most popular surface treatment method for polishing stents surfaces [74]. Nowadays, the literature presents rather conflicting information about the exact role of topographical manipulation to platelet response, with a study reporting no

significant differences between platelet activation on smooth or nanoscale topographical surfaces [75]. Other studies have shown that specific low roughness surfaces or nano-depth pattern can induce an antithrombogenic effect. For example, Chen *et al.* [76] showed that nano-micro patterned surfaces of TiO_2 presented lower platelet adhesion than on flat surfaces indicating that platelet activation may be dependent on the dimension of surface features as well as their aspect ratio. Certain nanostructured materials can have inherent antithrombogenic properties. If, in addition, high aspect ratio features are incorporated in their design then, platelet contact will be mainly limited to the tips of the nanopillars (or 'hilltops' and therefore, activation could be minimized [77,78]. Meanwhile, several studies observed the behaviour of ECs on different substrates with different patterning structures such as grooves, pillars, pits and ridges at the nano- and micro-meter range [79–82]. Numerous *in vitro* work demonstrated the importance of grooves on alignment of ECs promoting parallel migration, especially under low and normal stress conditions [79–82]. Biela *et al.* [80] showed that 10 µm width grooves induced ECs alignment and directed migration on silicon Si. Whereas, another study demonstrated a preferential orientation and elongation of ECs on anisotropically ordered ridges larger than 800 nm on a polyurethane substrate [81]. Thus, it is no real consensus on determining which topographical features influence a certain cell lineage adhesion.

3.1.2. Direct Laser Interference Patterning (DLIP)

A range of physical techniques are actually applied to modify the surface topography of vascular graft materials: metallographic grinding, plasma etching, photolithographic etching, UV lithography, among others [50,83,84]. Most of the employed processing techniques involve multiple preparation procedures incorporating coating and/or patterning steps. On the contrary, the **Direct Laser Interference Patterning (DLIP)** technique requires one single processing step and can be applied to a wide range of materials [85]. The principle is based on the unique intensity pattern generated by interfering laser beams (**Figure I.7**), which show periodicities from the submicron range up to 50 µm. By photothermal interaction with the irradiated surfaces, the periodic patterns translate to the actual spacing factor of the afterwards topographically and/or chemically structured surface.

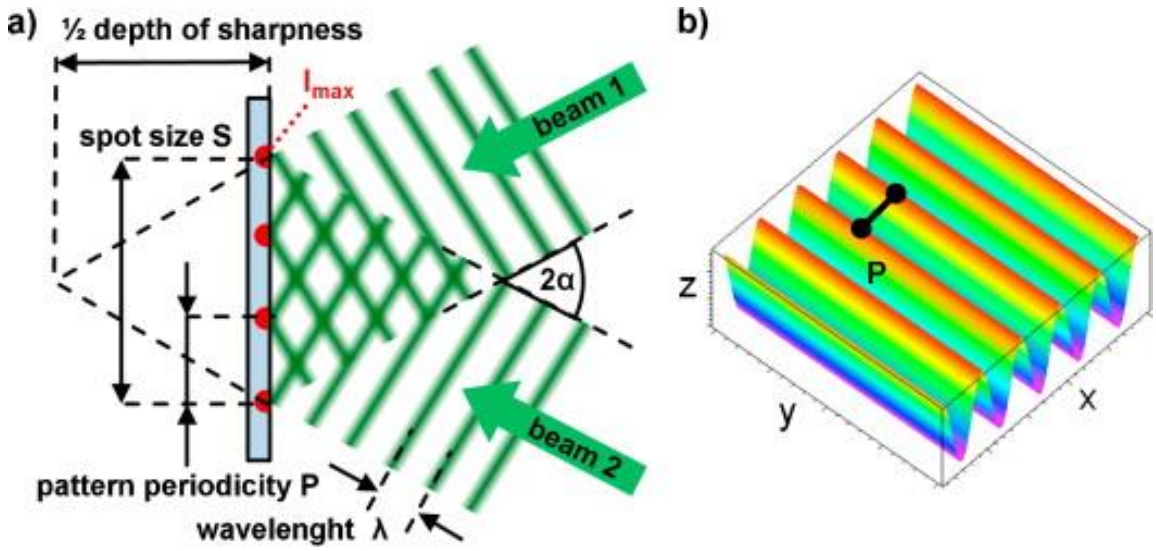

***Figure I.7**: Direct Laser Interference Patterning (DLIP) technique: (a) Beam configuration and principle of DLIP for a two beams set-up; (b) The calculated intensity distribution in case of two equal, interfering beams shows a line-like pattern with cos2(α) profile [86].*

Also, DLIP presents the possibility to obtain depth pattern lower than 20 nm which have never been elaborated for cardiovascular application. Finally, this technique has never been used in the cardiovascular field. Therefore, this PhD thesis proposes to use DLIP technique on CoCr alloy in order to obtain nano-micro patterned structure. To promote endothelial cells alignment and migration, lineal pattern will be design (**Figure I.8**). In addition, to study the influence of pattern depth on platelet adhesion, different pattern-depth will be fabricated.

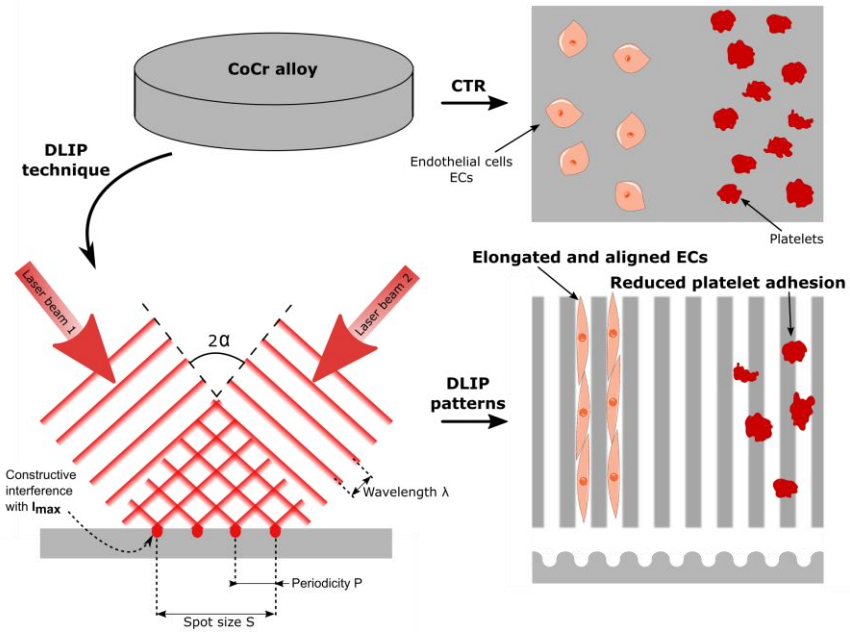

***Figure I.8**: Schematic representation of CoCr surfaces modification by DLIP technique and the expected effect on ECs and platelets response.*

3.2. Chemistry

Chemical methods are based on chemical reactions occurring at the surface of the material producing modifications of the chemical composition, structure, and/or stoichiometry of native materials surface.

Modifying surface topography, as described in the previous section, influences also important chemical properties. For instance, rougher topography increases surface electrostatic charge and surface energy. Both properties have a strong impact on the interactions of the material with the surrounding biological system. That is the reason why all the techniques introduced in the previous section have been also used to modify surface chemical composition, and eventually to create chemical patterns [86].

Other approaches to increase surface energy and hydrophilicity that produced promising in vitro and in vivo outcomes have been recently developed, such as cold plasma treatment [87–89] (**Figure I.9**), ultraviolet irradiation [90], sodium hydroxide (NaOH) etching [91,92] or ozone irradiation [93].

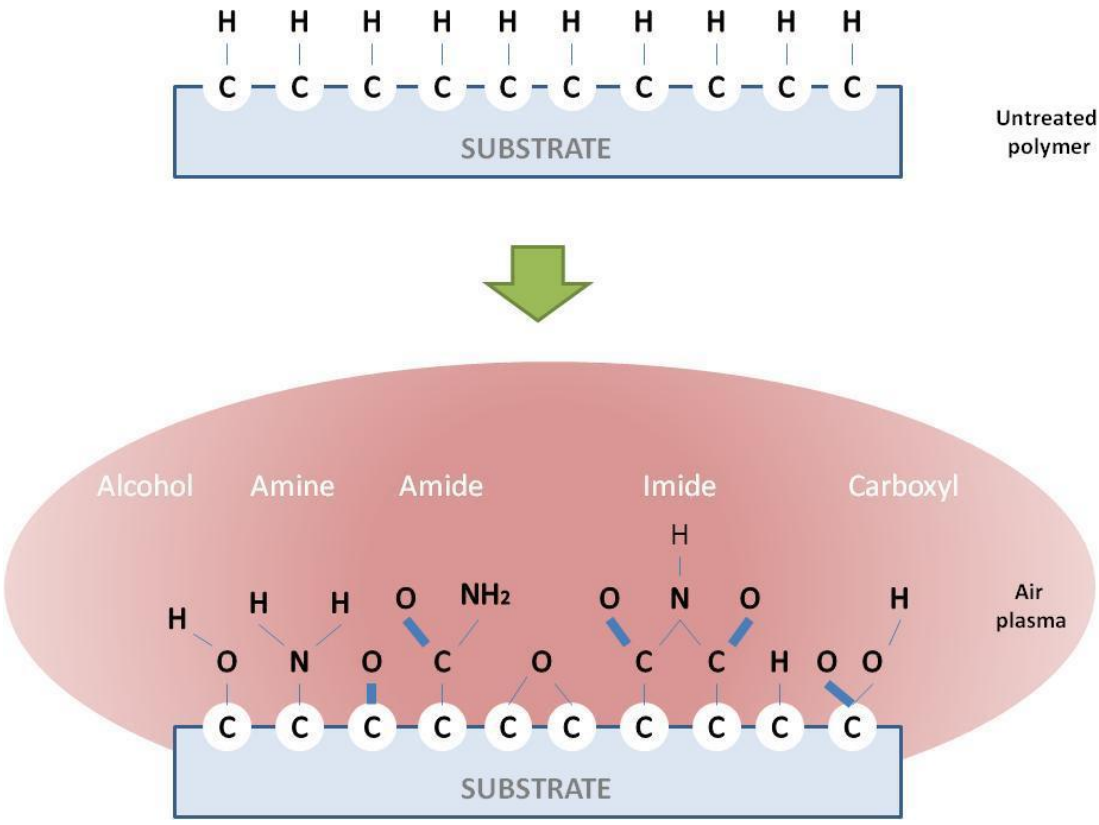

***Figure I.9**: Scheme of polymer surface functionalization by plasma processes using air as gas for plasma generation [105].*

For metallic alloys, chemical etching consists in the immersion of the samples into different acid (e.g. HCl, H_2SO_4, HNO_3 and HF) [94] or alkaline (e.g. NaOH) [8,95] chemical solutions. Depending on the chemical solution, the modified material can exhibit different reactivity. Thus, it is possible to induce the formation of a protecting layer by passivation or the dissolution and the flattening of surface defects. CoCr alloy reacts with alkaline solutions improving the formation of – OH groups on the CoCr surface due to the high pH solution.

Also, enzymatic treatments have been proposed and successfully used for the surface modification of natural and synthetic polymers [96,97]. For polyesters, such as PLLA, the hydrolysis of the ester bond by applying cutinase enzymes generate new hydroxyl and carboxyl groups onto the surface, which have been used to direct drug loading [98], to create superhydrophobic surfaces [99] or to bind serum albumin in order to increase biocompatibility [96]. Different activation treatments work differently onto PLLA surfaces, while NaOH treatment is an aggressive non-selective hydrolysis that generates etching [100,101], oxygen plasma acts more superficially (< 1 µm) and according to treatment conditions generates unspecific functionalization, hydrolysis and eventually etching [102,103] and, cutinase enzyme allows a selective hydrolysis of the ester bonds of the outermost surface layers of the polymer generating only hydroxyl and carboxyl groups [100,104].

3.3. Biofunctionalization

The described methods to modify surface properties of implants do not change intrinsic bioinert chemical characteristics of the surfaces and, hence, are limited in improving their biological response. The strategies that aim on modifying the biochemical nature of the surface in order to create specific interactions with specific cells can be more promising and are introduced in the following sections. Biofunctionalization of surfaces is a strategic research field, which relies on the use of biology tools to create biomimetic surfaces to incorporate biologically active molecules to generate specific responses [106].

The success of an implant relies on the establishment of strong and long lasting biochemical and mechanical interactions between the biomaterial and the surrounding endothelial tissue. The initial adhesion events of ECs on bioactive surfaces involve two distinct steps. An initial phase, where cells rapidly attach to the materials via physicochemical interactions (i.e. electrostatic forces,

hydrophobic interactions, hydrogen bonds, and van der Wall forces). And a second adhesive phase, in which cell adhesive proteins interact with each other and promote signal transduction and activation of long-term adhesion processes including cell proliferation and differentiation [107].

Integrins represent the most prominent family of cell adhesion receptors, and have crucial roles in cellular processes that require cell attachment or growth of tissue. In particular, integrins mediate cell-cell contacts and cell adhesion to proteins of the extracellular matrix (ECM) [108,109]. ECs express cell-surface integrins such as β_1 [108,110,111], which have the capacity to recognize and bind to ECM proteins. ECs ECM is composed of collagen 1, laminin, heparin and fibrin [112]. Modification of implant materials with biomolecules derived from ECM components represents thus, an attractive concept for biomaterial scientists to promote integrin-mediated binding of ECs and improve reendothelization. In the next sections, this approach will be described.

3.3.1. Cell response to biofunctionalization

Early studies investigated the use of natural, full-length ECM proteins to coat implant surfaces. These investigations included the use of collagen, heparin [113–116], laminin [117] and fibrin [118]. Although this approach was proven to be successful to enhance cell adhesion on the functionalized surfaces, the use of proteins bears several disadvantages that precluded their widespread use and application. In the first place, proteins are enzymatically unstable and long-term functionality within the body would not be possible. In addition, protein production is usually performed in other organisms, and therefore its use in humans is associated with an increased risk of infections and adverse immune responses. Also, proteins are costly to produce in large amounts and their manipulation, modification and characterization for surface coating purposes is a demanding task. Last but not least, the conformation of the protein and/or the orientation of the bioactive motifs might be influenced by the physicochemical properties of the surface resulting in non-favorable presentations to support cell adhesion [119,120].

Most of these drawbacks may be overcomed by using short ECM-derived peptides that contain the cell adhesive motifs, usually of only a few amino acids, present in the natural proteins (**Figure I.10**). Linear peptides are readily available using current solid phase peptide synthesis methodologies, and can be produced

in large quantities at a very low cost. They are easily characterized and functionalized for coating purposes. Moreover, due to lower steric requirements, they could be immobilized with higher density on solid supports compared to native ECM proteins. They are also much less sensitive to pH and temperature changes than full-length proteins. Finally, short linear peptides are not immunogenic and their use is exempt from infection risks.

The **RGD sequence** (Arg-Gly-Asp) represents by far the most extensively studied cell adhesion motif used to functionalize surfaces and implant materials in order to stimulate cell attachment and adhesion, enhance cell migration and influence cell proliferation and differentiation [119]. Since its discovery in 1984 as the minimal cell binding sequence in fibronectin [121], this tripeptide has also been identified in many other ECM proteins with cell adhesive properties. Thus, besides fibronectin, the RGD sequence was detected in fibrinogen, collagen type I, vitronectin, von Willebrand factor, osteopontin, laminin, tenascin and thrombospondin [122–124]. Of the 24 known integrins, 8 receptor subtypes have been described to recognize and bind the RGD motif: $\alpha_v\beta_1$, $\alpha_v\beta_3$, $\alpha_v\beta_5$, $\alpha_v\beta_6$, $\alpha_v\beta_8$, $\alpha_5\beta_1$, $\alpha_8\beta_1$ and $\alpha_{IIb}\beta_3$ [108,109]. As said before, ECs are known to express β_1 integrins. Thus, it seems plausible that functionalization of surfaces with short RGD motifs might help to promote EC adhesion and reendothelization. The literature is full of examples of enhanced EC adhesion on matrices coated with short RGD peptides [69,125,126]. However, due to the presence of RGD receptors in most integrins, RGD motif binds with most integrins. Consequently, ECs adhesion to RGD is not specific and it is probable that RGD motif induces SMCs adhesion and platelets adhesion.

Various ECM peptide sequences, which have been determined to influence specifically EC behavior, have been isolated and grafted on materials to enhance biological properties, for example, Arg-Glu-Asp-Val (REDV), Pro-His-Ser-Arg-Asn (PHSRN) and Gly-Arg-Gly-Asp-Ser-Pro (GRGDSP) from fibronectin, laminin-derived recognition sequences, Ile-Lys-Leu-Leu-Ile (IKLLI), Ile-Lys-Val-Ala-Val (IKVAV), Leu-Arg-Glu (LRE), Pro-Asp-Ser-Gly-Arg (PDSGR), and Tyr-Ile-Gly-Ser-Arg (YIGSR), and collagen type I derived sequence, Asp-Gly-Glu-Ala (DGEA). In particular, the **laminin-derived peptide sequence YIGSR** has demonstrated improved EC attachment, spreading and resistance to shear stress [127–129]. Recently, Taite *et al*. incorporated polyethylene glycol (PEG)

and the YIGSR peptide into the backbone of polyurethane to improve the long-term patency of polyurethane vascular grafts [130]. The incorporation of PEG reduced platelet adhesion *in vitro*. Additionally, the incorporation of YIGSR peptide encouraged EC adhesion and SMCs did not adhere to YIGSR-containing polyurethane.

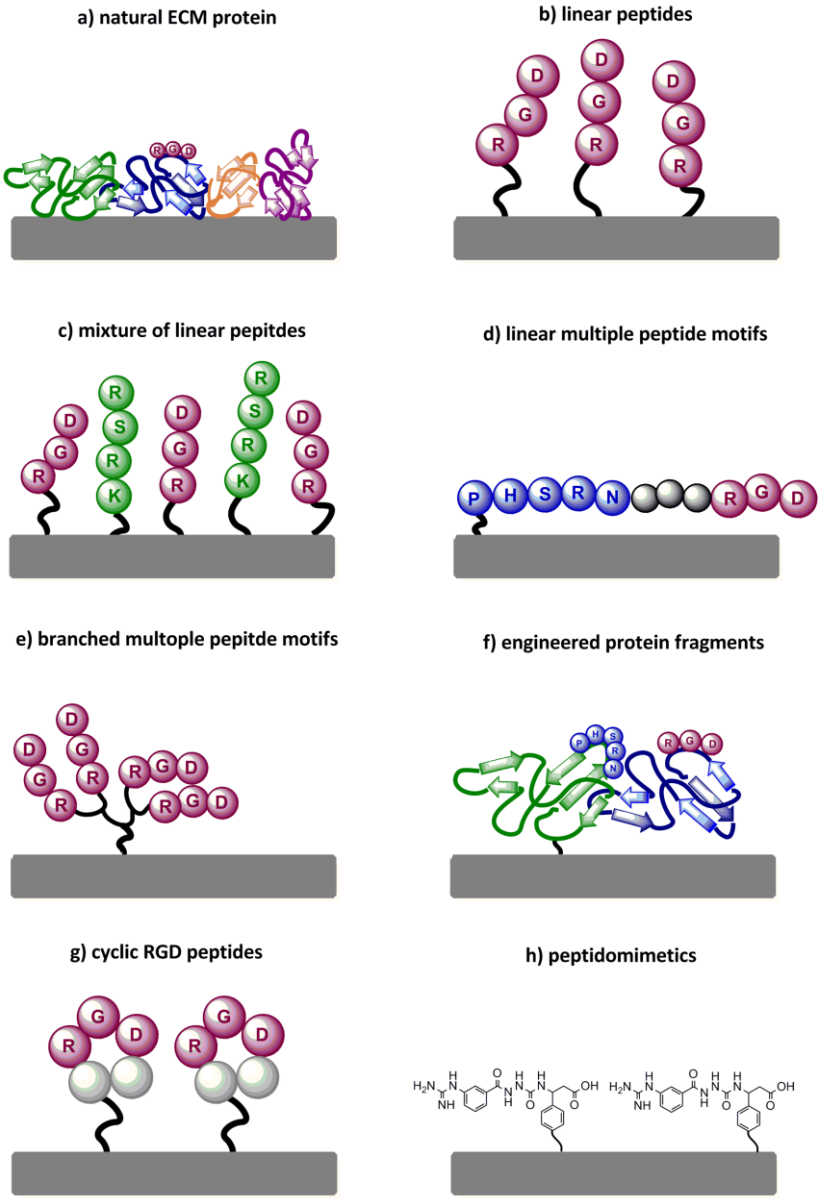

***Figure I.10**: Strategies to biofunctionalize material surfaces with biomolecules. A) Adsorption of naturally occurring ECM proteins. These proteins contain cell adhesive motifs such as the RGD sequence; B) Immobilization of cell adhesive linear peptides, i.e. RGD peptides; C) Combination of linear peptides that synergize or act via distinct cell adhesive mechanisms; D) Use of peptides that bear multiple bioactive sequences in a controlled fashion; E) Multiple copies of the same epitope, e.g. multiple antigenic peptides (MAPs) of RGD peptides, may be used to increase cell adhesion; F) Engineered protein fragments presenting synergy domains required for selective cell adhesion, e.g. RGD and PHSRN direct α5β1-mediated adhesion; G) Immobilization of cyclic RGD peptides highly active and selective for integrins expressed by osteoblasts; H) Coating of surfaces with RGD peptidomimetic designed to be highly specific and stable to enzymatic degradation [131].*

3.3.2. Design of biofunctional molecules

The binding of the bioactive molecule to the metallic surface represents a critical step in the process of biofunctionalization. Thus, even peptide sequences with high cell adhesive potential may fail to promote cellular attachment if the immobilization of the biomolecules to the materials surface, and their presentation to cell-surface receptors, are not optimal.

The design of the biomolecule is a critical step to successfully immobilize it to the biomaterials surface. The main parts of a biomolecule and the desired characteristics of the surface for an optimal immobilization are the following (**Figure I.11**):

1) The implant material: as we have previously mentioned the biological performance of a material strongly depends on its bulk and surface properties. In particular, the chemistry of the surface will determine the type of binding of the biomolecule to the material.

2) The anchor is commonly a chemical group that allows a strong and selective binding of the peptide sequence to the surface. It is crucial that such attachment is long-lasting and stable through all the process of implantation (e.g. stable to sterilization). In regard to the chemistry of the surface, distinct anchors might be used. For instance, thiols bind to gold and titanium/titanium oxide with high affinity; phosphonates to titanium/titanium oxide; and isothiocyanates to amino groups [119]. Furthermore, surfaces may be functionalized with crosslinker molecules bearing specific functional chemical groups, thereby allowing a wide range of chemoselective reactions to attach molecules to the surface [119].

3) A key element in a coating system usually underestimated is the spacer. This linker unit provides the required distance between the peptide motif and the surface material, in order to optimally present the bioactive sequence to cell-surface receptors. Taking as example RGD peptides, it has been reported that a minimum spacer is necessary to ensure a correct accessibility of the RGD sequence to the integrins and achieve cell adhesion [132,133]. Chemical groups commonly used include aminohexanoic acid and polyethylene glycol (PEG). Choosing the right spacer, might be a difficult task, since not only the length but also other physicochemical properties need to be carefully considered. For instance, PEG chains offer an antifouling behavior that is useful to avoid non-specific protein adsorption, and to confer antimicrobial properties to the

surface [134]; nonetheless, PEG-based spacers are highly flexible and their use might result in bent conformations not accessible for the cells.

4) Bioactive sequences useful to control the desired cell response.

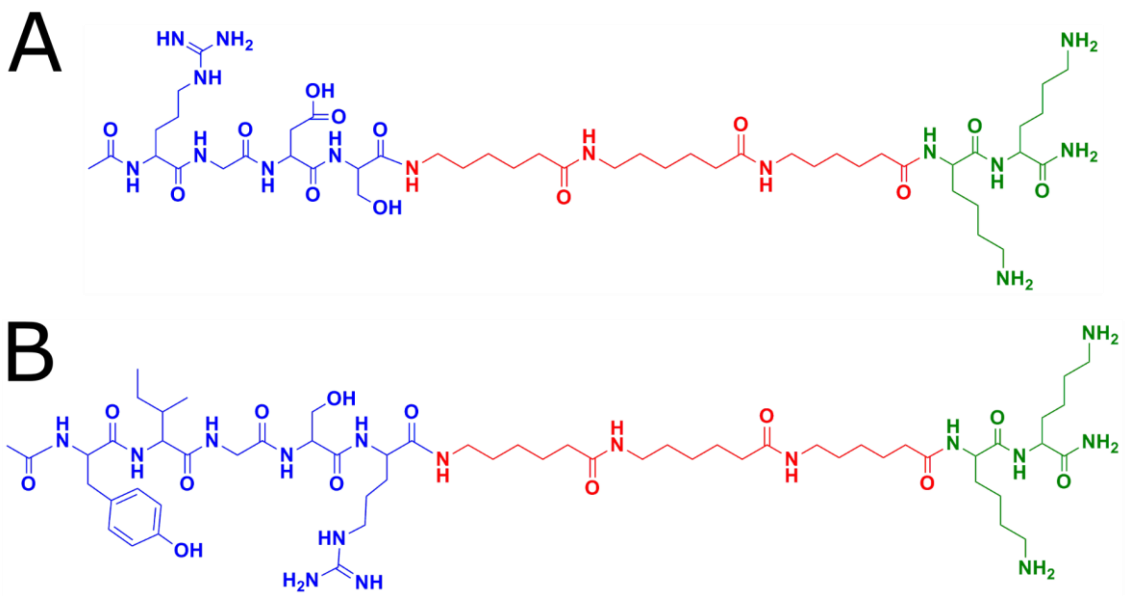

***Figure I.11**: Examples of designed biofunctional molecules. Green: anchoring sequence (Lys-Lys). Red: spacer units (Ahx-Ahx-Ahx). Blue: functional sequences (A: Arg-Gly-Asp-Ser and B: Tyr-Ile-Gly-Ser-Arg).*

3.3.3. Immobilization strategies

There are three major strategies to biofunctionalize biomaterial surfaces: physical adsorption, physical entrapment or immobilization, and covalent attachment [135]. Here, we will shortly focus only on the processes of physisorption and covalent binding.

The process of **physical adsorption**, also known as **physisorption**, relies on the establishment of non-covalent interactions between the biomolecule and the surface. These interactions, which include hydrophobic and electrostatic interactions, van der Waal forces and hydrogen bonds, are weak but altogether may result in effective adsorption of biomolecules on a surface. The success of physical adsorption is therefore based on the physicochemical properties of the biomolecule and the surface properties (chemistry and energy) of the material. Although this approach is simple and fast, and has been widely used to immobilize proteins on the surface it is based on weak interactions, and therefore, the stability of the biological coating might be compromised at longterm and be

not optimal for clinical applications. Moreover, the adsorption of proteins into a surface takes place in a nonspecific manner and may result an unfavourable adsorption (i.e. adhesive sequences not accessible) thereby displaying reduced adhesive activities.

The **covalent immobilization** of biomolecules onto surface materials offers an alternative which brings an improved stability to the biomaterial coating. Covalent immobilization is often used with short adhesive peptides which typically do not physisorb efficiently to metal surfaces, since they lack the minimum number of chemical groups to establish stable noncovalent interactions. Some authors refer to covalent immobilization as chemisorption, meaning that strong chemical bonds, ionic or covalent, bind stronlgy the surface and the biomolecule. To avoid that such irreversibly immobilization modifies the chemical structure of the active sequence, with concomitant loss of biological activity, the use of the appropriate anchors to bind covalently and selectively with the chemical groups of the surface, is highly recommended. These interesting and controlled characteristics makes covalent bonding as a preferred strategy over physical adsorption to immobilize biomolecules on metallic surfaces.

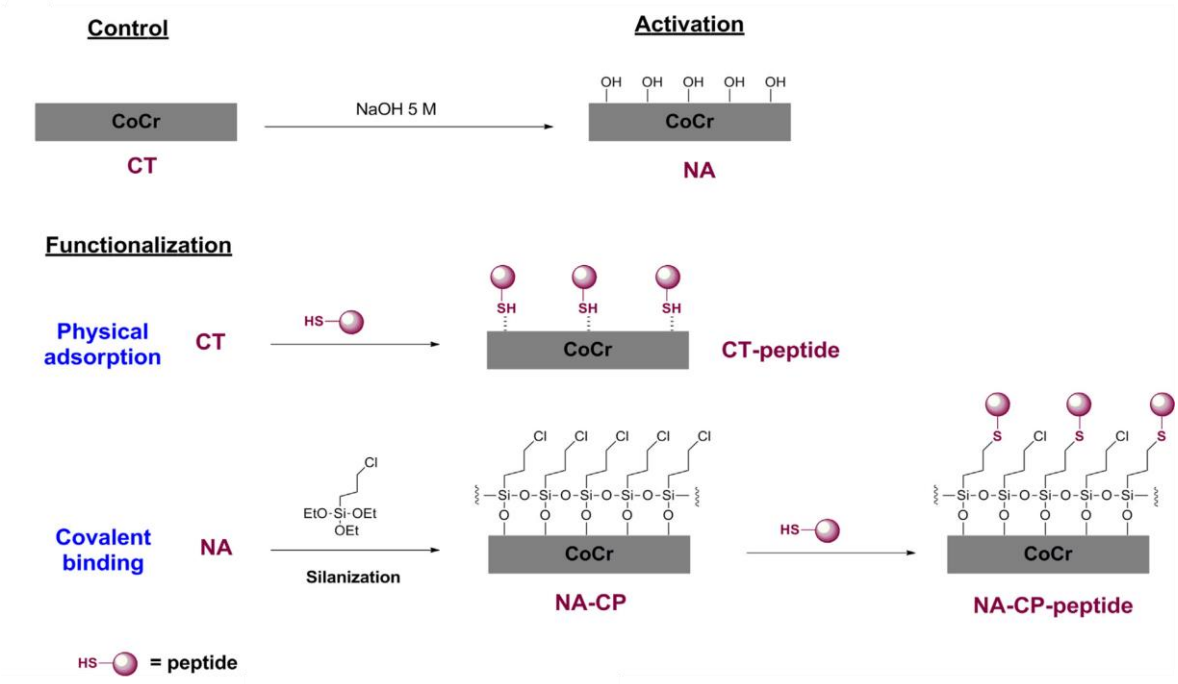

***Figure I.12**: Examples of immobilization methods of cell adhesive peptides on CoCr alloy: physical adsorption and, covalent bonding through NaOH activation and CPTES silanization. Adapted from [8].*

4. 3D printing for stent fabrication

Stephen Nigro, president of HP Inc.'s 3D printer business, said '*we're on the cusp of the Fourth Industrial Revolution*'. This thesis also propose to evaluate the interest of the use of solvent-cast direct writing technique to obtain 3D-printed biodegradable stents.

3D printing world is offering the possibility to obtain fully customized products. For this reason, biomaterials scientists are focusing their efforts on finding ways to use the different 3D printing technologies to obtain implants with a personalized shape to the treated patient. The idea is to acquire a 3D image of the damaged living tissue of the patient, to use this image to design the implant 3D-shape and finally to fabricate a customized implant by 3D technologies. The most outstanding part of this solution being that the time between imaging acquisition and device implantation could be reduced to 2 days. Moreover, the stents can be also personalized to patient's drugs needs.

Due to the particularly complex cylindrical shape and low infill percentage of stents, few studies have been conducted to obtain 3D-printed stent. Particularly, no cardiovascular stent has been obtained by 3D printing due to the extremely low stent wire diameter (< 120 µm) and the use of other techniques.

Although traditional 3D printing based on selective laser sintering (SLS), stereolithography (SAS) and fused deposition modeling (FDM) can provide a fast, reproducible and precise approach to generate biomaterials, these techniques would be probably too complex to adapt to obtain cardiovascular stent. On the other hand, 3D direct ink writing (DIW) techniques permit to print tridimensional biomaterials under milder conditions, without the need of high temperatures or invasive photopolymerization processes.

DIW is an additive fabrication technique that includes all the 3D printing processes where an ink is extruded through a nozzle and plotted layer by layer in 3 dimensions [136,137]. The ideal rheological behavior should present a gel-like consistency with a viscosity low enough to allow flowing through the nozzle when extruded [137]. Moreover, the paste must have a pseudoplastic behavior in order to rapidly increase its viscosity once deposited providing a self-supporting structure [138]. Finally, the obtained structures should also resist the subsequent hardening steps or curing processes [139].

This technique has already been used with PLLA to obtain very complex shape with wire diameter inferior to 100 µm [140] (**Figure I.13**). For these reasons, we decided to adapt this technique to print a cylindrical stent on a rotating mandrel.

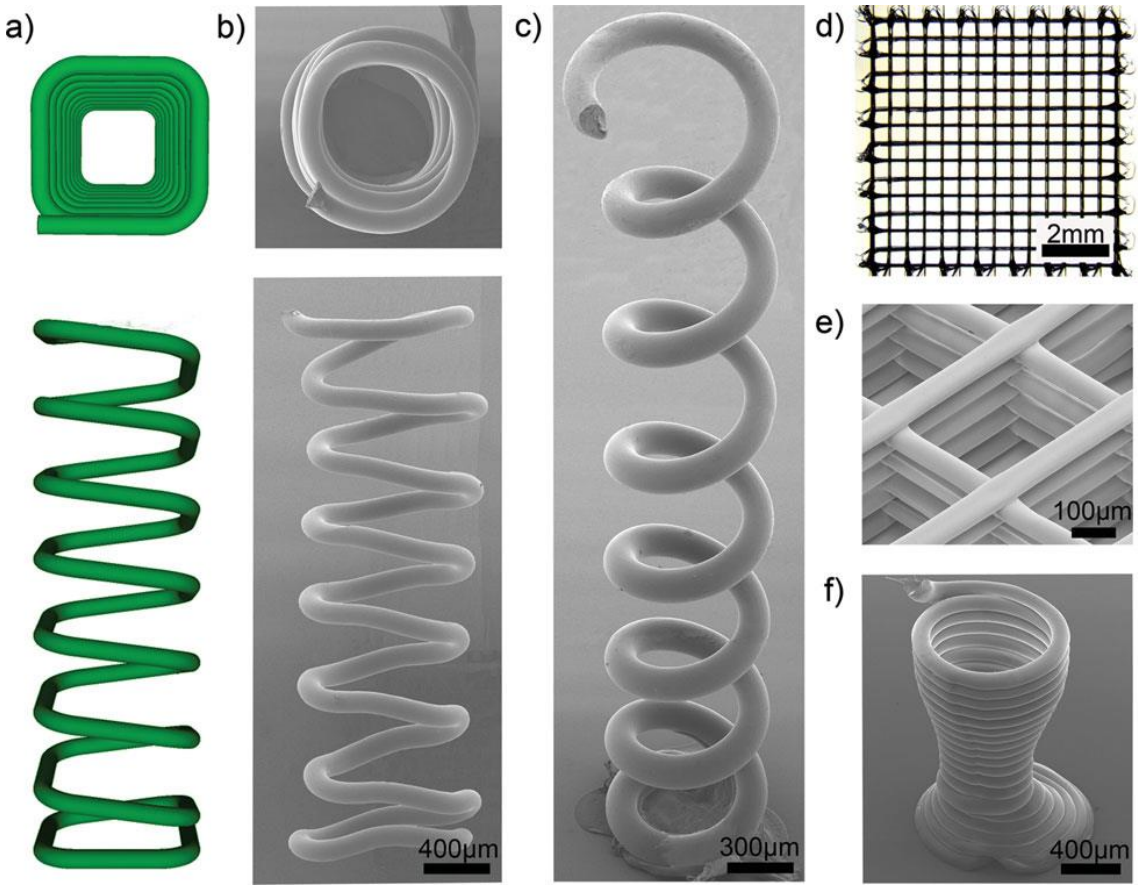

***Figure I.13**: Different microstructures manufactured by 3D direct ink writing by Guo et al. [140]. (a) Top and side view virtual images of the programmed DIW fabrication of the square spiral. (b) Top and side view SEM images of an actual PLA square spiral. (c) Inclined top view SEM image of a PLA circular spiral. (d) Representative optical image of a PLA scaffold composed of nine layers. (e) Inclined top view SEM image of PLA 9-layer scaffold. (f) SEM image of a PLA cup.*

References

(1) Simard, T.; Hibbert, B.; Ramirez, F. D.; Froeschl, M.; Chen, Y.-X.; O'Brien, E. R. The Evolution of Coronary Stents: A Brief Review. *Can. J. Cardiol.* **2014**, *30* (1), 35–45.

(2) Mendis, S.; Pekka, P.; Norrving, B. Global Atlas on Cardiovascular Disease Prevention and Control. **2011**, 155.

(3) Garg, S.; Serruys, P. W. Coronary Stents: Current Status. *J. Am. Coll. Cardiol.* **2010**, *56* (10 Suppl), S1-42.

(4) Nakamura, K.; Keating, J. H.; Edelman, E. R. Pathology of Endovascular Stents. *Interv. Cardiol. Clin.* **2016**.

(5) Otsuka, F.; Finn, A. V.; Yazdani, S. K.; Nakano, M.; Kolodgie, F. D.; Virmani, R. The Importance of the Endothelium in Atherothrombosis and Coronary Stenting. *Nat. Rev. Cardiol.* **2012**, *9* (8), 439–453.

(6) Newby, A. Molecular Mechanisms in Intimal Hyperplasia. *J. Pathol.* **2000**, *190* (3), 300–309.

(7) Kipshidze, N.; Dangas, G.; Tsapenko, M.; Moses, J.; Leon, M. B.; Kutryk, M.; Serruys, P. Role of the Endothelium in Modulating Neointimal Formation: Vasculoprotective Approaches to Attenuate Restenosis after Percutaneous Coronary Interventions. *J. Am. Coll. Cardiol.* **2004**, *44* (4), 733–739.

(8) Castellanos, M. I.; Mas-Moruno, C.; Grau, A.; Serra-Picamal, X.; Trepat, X.; Albericio, F.; Joner, M.; Manero, J. M.; Pegueroles, M. Functionalization of CoCr Surfaces with Cell Adhesive Peptides to Promote HUVECs Adhesion and Proliferation. *Appl. Surf. Sci.* **2016**, *393*, 82–92.

(9) Thakar, R. G.; Cheng, Q.; Patel, S.; Chu, J.; Nasir, M.; Liepmann, D.; Komvopoulos, K.; Li, S. Cell-Shape Regulation of Smooth Muscle Cell Proliferation. *Biophysj* **2009**, *96* (8), 3423–3432.

(10) Ross, R. The Smooth Muscle Cell. II. Growth of Smooth Muscle in Culture and Formation of Elastic Fibers. *J. Cell Biol.* **1971**, *50* (1), 172–186.

(11) Sartore, S.; Chiavegato, a.; Faggin, E.; Franch, R.; Puato, M.; Ausoni, S.; Pauletto, P. Contribution of Adventitial Fibroblasts to Neointima Formation and Vascular Remodeling: From Innocent Bystander to Active Participant. *Circ. Res.* **2001**, *89*

(12), 1111–1121.

(12) Ghattas, A.; Griffiths, H. R.; Devitt, A.; Lip, G. Y. H.; Shantsila, E. Monocytes in Coronary Artery Disease and Atherosclerosis: Where Are We Now? *J. Am. Coll. Cardiol.* **2013**, *62* (17), 1541–1551.

(13) Cooley, B. C. Collagen-Induced Thrombosis in Murine Arteries and Veins. *Thromb. Res.* **2013**, *131* (1), 49–54.

(14) Li, S.; Li, X.; Li, J.; Deng, X.; Li, Y.; Cong, Y. Experimental Arterial Thrombosis Regulated by Androgen and Its Receptor via Modulation of Platelet Activation. *Thromb. Res.* **2007**, *121* (1), 127–134.

(15) Hanawa, T. Materials for Metallic Stents. *J. Artif. Organs* **2009**, *12* (2), 73–79.

(16) Serruys P.W., et al. A Comparison of Balloon-Expandable-Stent Implantation with Balloon Angliplasty in Patients with Coronary Artery Desease. *N. Engl. J. Med.* **1994**, *331*, 490–495.

(17) Höher, M.; Wöhrle, J.; Grebe, O. C.; Kochs, M.; Osterhues, H. H.; Hombach, V.; Buchwald, A. B. A Randomized Trial of Elective Stenting after Balloon Recanalization of Chronic Total Occlusions. *J. Am. Coll. Cardiol.* **1999**, *34* (3), 722–729.

(18) Go, A. S.; Mozaffarian, D.; Roger, V. L.; Benjamin, E. J.; Berry, J. D.; Borden, W. B.; Bravata, D. M.; Dai, S.; Ford, E. S.; Fox, C. S.; Franco, S.; Fullerton, H. J.; Gillespie, C.; Hailpern, S. M.; Heit, J. a; Howard, V. J.; Huffman, M. D.; Kissela, B. M.; Kittner, S. J.; Lackland, D. T.; Lichtman, J. H.; Lisabeth, L. D.; Magid, D.; Marcus, G. M.; Marelli, A.; Matchar, D. B.; McGuire, D. K.; Mohler, E. R.; Moy, C. S.; Mussolino, M. E.; Nichol, G.; Paynter, N. P.; Schreiner, P. J.; Sorlie, P. D.; Stein, J.; Turan, T. N.; Virani, S. S.; Wong, N. D.; Woo, D.; Turner, M. B. Heart Disease and Stroke Statistics--2013 Update: A Report from the American Heart Association. *Circulation* **2013**, *127* (1), 6–245.

(19) Nazneen, F.; Herzog, G.; Arrigan, D. W. M.; Caplice, N.; Benvenuto, P.; Galvin, P.; Thompson, M. Surface Chemical and Physical Modification in Stent Technology for the Treatment of Coronary Artery Disease. *J. Biomed. Mater. Res. B. Appl. Biomater.* **2012**, *100B* (7), 1989–2014.

(20) Holmes, D.; Camrud, A. Polymeric Stenting in the Porcine Coronary Artery Model: Differential Outcome of Exogenous Fibrin Sleeves versus Polyurethane-Coated

Stents. *J. Am. Coll. Cardiol.* **1994**, *24* (August), 525–531.

(21) van der Giessen, W. J.; Lincoff, a M.; Schwartz, R. S.; van Beusekom, H. M.; Serruys, P. W.; Holmes, D. R.; Ellis, S. G.; Topol, E. J. Marked Inflammatory Sequelae to Implantation of Biodegradable and Nonbiodegradable Polymers in Porcine Coronary Arteries. *Circulation* **1996**, *94* (7), 1690–1697.

(22) Busch, R.; Strohbach, A.; Rethfeldt, S.; Walz, S.; Busch, M.; Petersen, S.; Felix, S.; Sternberg, K. New Stent Surface Materials: The Impact of Polymer-Dependent Interactions of Human Endothelial Cells, Smooth Muscle Cells, and Platelets. *Acta Biomater.* **2014**, *10* (2), 688–700.

(23) Grewe, P. H.; Deneke, T.; Machraoui, a; Barmeyer, J.; Müller, K. M. Acute and Chronic Tissue Response to Coronary Stent Implantation: Pathologic Findings in Human Specimen. *J. Am. Coll. Cardiol.* **2000**, *35* (1), 157–163.

(24) Li, S.; Henry, J. J. D. Nonthrombogenic Approaches to Cardiovascular Bioengineering. *Annu. Rev. Biomed. Eng.* **2011**, *13*, 451–475.

(25) Verheul, H. M. W.; Pinedo, H. M. Possible Molecular Mechanisms Involved in the Toxicity of Angiogenesis Inhibition. *Nat. Rev. Cancer* **2007**, *7* (6), 475–485.

(26) Sigwart, U.; Urban, P.; Golf, S.; Kaufmann, U.; Imbert, C.; Fischer, a.; Kappenberger, L. Emergency Stenting for Acute Occlusion after Coronary Balloon Angioplasty. *Circulation* **1988**, *78* (5), 1121–1127.

(27) Carrié, D.; Elbaz, M.; Andrieu, M.; Cantié, P.; Fourcade, J.; Puel, J. Ten-Year Clinical and Angiographic Follow-up of Coronary Wallstent. *Am. J. Cardiol.* **2000**, *85* (1), 95–98, A8.

(28) Morice M.C., Serruys P.W., and al. A Randomized Comparison of a Sirolimus-Eluting Stent with a Standard Stent for Coronary Revascularization. *N. Engl. J. Med.* **2002**, *346* (23), 1773–1780.

(29) Moses, J.; Leon, M. Sirolimus-Eluting Stents versus Standard Stents in Patients with Stenosis in a Native Coronary Artery. *N. Engl. J. Med.* **2003**, *349*, 1315–1323.

(30) Serruys, P. W.; Daemen, J. Are Drug-Eluting Stents Associated with a Higher Rate of Late Thrombosis than Bare Metal Stents? Late Stent Thrombosis: A Nuisance in Both Bare Metal and Drug-Eluting Stents. *Circulation* **2007**, *115* (11), 1433–9; discussion 1439.

(31) McFadden, E. P.; Stabile, E.; Regar, E.; Cheneau, E.; Ong, A. T. L.; Kinnaird, T.;

Suddath, W. O.; Weissman, N. J.; Torguson, R.; Kent, K. M.; Pichard, A. D.; Satler, L. F.; Waksman, R.; Serruys, P. W. Late Thrombosis in Drug-Eluting Coronary Stents after Discontinuation of Antiplatelet Therapy. *Lancet* **2004**, *364* (9444), 1519–1521.

(32) Ong, A. T. L.; McFadden, E. P.; Regar, E.; de Jaegere, P. P. T.; van Domburg, R. T.; Serruys, P. W. Late Angiographic Stent Thrombosis (LAST) Events with Drug-Eluting Stents. *J. Am. Coll. Cardiol.* **2005**, *45* (12), 2088–2092.

(33) Serruys, P. W.; Onuma, Y.; Garg, S.; Vranckx, P.; De Bruyne, B.; Morice, M.-C.; Colombo, A.; Macaya, C.; Richardt, G.; Fajadet, J.; Hamm, C.; Schuijer, M.; Rademaker, T.; Wittebols, K.; Stoll, H. P. 5-Year Clinical Outcomes of the ARTS II (Arterial Revascularization Therapies Study II) of the Sirolimus-Eluting Stent in the Treatment of Patients with Multivessel de Novo Coronary Artery Lesions. *J. Am. Coll. Cardiol.* **2010**, *55* (11), 1093–1101.

(34) Moravej, M.; Mantovani, D. Biodegradable Metals for Cardiovascular Stent Application: Interests and New Opportunities. *Int. J. Mol. Sci.* **2011**, *12* (7), 4250–4270.

(35) Tanimoto, S.; Serruys, P. W.; Thuesen, L.; Dudek, D.; de Bruyne, B.; Chevalier, B.; Ormiston, J. a. Comparison of in Vivo Acute Stent Recoil between the Bioabsorbable Everolimus-Eluting Coronary Stent and the Everolimus-Eluting Cobalt Chromium Coronary Stent: Insights from the ABSORB and SPIRIT Trials. *Catheter. Cardiovasc. Interv.* **2007**, *70* (4), 515–523.

(36) Ormiston, J. a; Webster, M. W. I.; Armstrong, G. First-in-Human Implantation of a Fully Bioabsorbable Drug-Eluting Stent: The BVS Poly-L-Lactic Acid Everolimus-Eluting Coronary Stent. *Catheter. Cardiovasc. Interv.* **2007**, *69* (1), 128–131.

(37) Serruys, P. W.; Ormiston, J. a; Onuma, Y.; Regar, E.; Gonzalo, N.; Garcia-Garcia, H. M.; Nieman, K.; Bruining, N.; Dorange, C.; Miquel-Hébert, K.; Veldhof, S.; Webster, M.; Thuesen, L.; Dudek, D. A Bioabsorbable Everolimus-Eluting Coronary Stent System (ABSORB): 2-Year Outcomes and Results from Multiple Imaging Methods. *Lancet* **2009**, *373* (9667), 897–910.

(38) Ormiston, J. a; Serruys, P. W. S. Bioabsorbable Coronary Stents. *Circ. Cardiovasc. Interv.* **2009**, *2* (3), 255–260.

(39) Castellanos, M. I. Functionalized CoCr Alloy Surfaces with Cell Adhesive Molecules

to Improve Endothelialization, 2017.

(40) Hanawa, T. Biofunctionalization of Titanium for Dental Implant. *Jpn. Dent. Sci. Rev.* **2010**, *46* (2), 93–101.

(41) Niinomi, M. Metallic Biomaterials. *J. Artif. Organs* **2008**, *11* (3), 105–110.

(42) Lim, I. A. L. Biocompatibility of Stent Materials. **2004**, *11*, 33–37.

(43) Akazawa, T.; Minami, S.; Takahashi, K.; Kotani, T.; Hanawa, T.; Moriya, H. Corrosion of Spinal Implants Retrieved from Patients with Scoliosis. *J. Orthop. Sci.* **2005**, *10* (2), 200–205.

(44) Tomizawa, Y.; Hanawa, T.; Kuroda, D.; Nishida, H.; Endo, M. Corrosion of Stainless Steel Sternal Wire after Long-Term Implantation. *J. Artif. Organs* **2006**, *9* (1), 61–66.

(45) Heintz, C.; Riepe, G.; Birken, L.; Kaiser, E.; Chakfé, N.; Morlock, M.; Delling, G.; Imig, H. Corroded Nitinol Wires in Explanted Aortic Endografts: An Important Mechanism of Failure? *J. Endovasc. Ther.* **2001**, *8* (3), 248–253.

(46) Poncin, P.; Proft, J. Stent Tubing: Understanding the Desired Attributes. *Proc. ASM Conf. Mater. Process. Med. Devices* **2003**, No. September, 253–259.

(47) Nef, H. M.; Möllmann, H.; Weber, M.; Auch-Schwelk, W.; Bonzel, T.; Varelas, J.; Nordt, T. K.; Schofer, J.; Minden, H. H.; Stumpf, J.; Schneider, S.; Elsässer, A.; Hamm, C. W. Cobalt-Chrome MULTI-LINK VISION^{TM}-Stent Implantation in Diabetics and Complex Lesions: Results from the DaVinci-Registry. *Clin. Res. Cardiol.* **2009**, *98* (11), 731–737.

(48) Khatibi, G.; Lederer, M.; Betzwar Kotas, A.; Frotscher, M.; Krause, A.; Poehlmann, S. High-Cycle Fatigue Behavior of Thin-Walled CoCr Tubes. *Int. J. Fatigue* **2015**, *80*, 103–112.

(49) Aróstegui, a.; Nazábal, J. Critical Inter-Particle Distance Dependence and Super-Toughness in Poly(butylene Terephthalate)/grafted Poly(ethylene-Octene) Copolymer Blends by Means of Polyarylate Addition. *Polymer (Guildf).* **2003**, *44* (18), 5227–5237.

(50) Li, Y.; Thouas, G. a; Chen, Q.-Z. Biodegradable Soft Elastomers: Synthesis/properties of Materials and Fabrication of Scaffolds. *RSC Adv.* **2012**, *2* (22), 8229–8242.

(51) Kraitzer, A.; Kloog, Y.; Zilberman, M. Approaches for Prevention of Restenosis. *J.*

Biomed. Mater. Res. B. Appl. Biomater. **2008**, *85* (2), 583–603.

(52) Park, H.; Seo, J.; Lee, H.-Y.; Kim, H.-W.; Wall, I. B.; Gong, M.-S.; Knowles, J. C. Synthesis of Elastic Biodegradable Polyesters of Ethylene Glycol and Butylene Glycol from Sebacic Acid. *Acta Biomater.* **2012**, *8* (8), 2911–2918.

(53) Van de Velde, K.; Kiekens, P. Biopolymers: Overview of Several Properties and Consequences on Their Applications. *Polym. Test.* **2002**, *21* (4), 433–442.

(54) Serruys, P. W.; Sianos, G.; Abizaid, A.; Aoki, J.; den Heijer, P.; Bonnier, H.; Smits, P.; McClean, D.; Verheye, S.; Belardi, J.; Condado, J.; Pieper, M.; Gambone, L.; Bressers, M.; Symons, J.; Sousa, E.; Litvack, F. The Effect of Variable Dose and Release Kinetics on Neointimal Hyperplasia Using a Novel Paclitaxel-Eluting Stent Platform: The Paclitaxel In-Stent Controlled Elution Study (PISCES). *J. Am. Coll. Cardiol.* **2005**, *46* (2), 253–260.

(55) Barlis, P.; Regar, E.; Serruys, P. W.; Dimopoulos, K.; van der Giessen, W. J.; van Geuns, R.-J. M.; Ferrante, G.; Wandel, S.; Windecker, S.; van Es, G.-A.; Eerdmans, P.; Jüni, P.; di Mario, C. An Optical Coherence Tomography Study of a Biodegradable vs. Durable Polymer-Coated Limus-Eluting Stent: A LEADERS Trial Sub-Study. *Eur. Heart J.* **2010**, *31* (2), 165–176.

(56) Hamilos, M. I.; Ostojic, M.; Beleslin, B.; Sagic, D.; Mangovski, L.; Stojkovic, S.; Nedeljkovic, M.; Orlic, D.; Milosavljevic, B.; Topic, D.; Karanovic, N.; Wijns, W. Differential Effects of Drug-Eluting Stents on Local Endothelium-Dependent Coronary Vasomotion. *J. Am. Coll. Cardiol.* **2008**, *51* (22), 2123–2129.

(57) Garg, S.; Serruys, P. W. Coronary Stents: Looking Forward. *J. Am. Coll. Cardiol.* **2010**, *56* (10 Suppl), 43–78.

(58) Lemos, P. a; Moulin, B.; Perin, M. a; Oliveira, L. a R. R.; Arruda, J. A.; Lima, V. C.; Lima, A. a G.; Caramori, P. R. a; Medeiros, C. R.; Barbosa, M. R.; Brito, F. S.; Ribeiro, E. E.; Martinez, E. E. Randomized Evaluation of Two Drug-Eluting Stents with Identical Metallic Platform and Biodegradable Polymer but Different Agents (Paclitaxel or Sirolimus) Compared against Bare Stents: 1-Year Results of the PAINT Trial. *Catheter. Cardiovasc. Interv.* **2009**, *74* (5), 665–673.

(59) Douek, P. C.; Correa, R.; Neville, R.; Unger, E. F.; Shou, M.; Banai, S.; Ferrans, V. J.; Epstein, S. E.; Leon, M. B.; Bonner, R. F. Dose-Dependent Smooth Muscle Cell Proliferation Induced by Thermal Injury with Pulsed Infrared Lasers. *Circulation*

1992, *86* (4), 1249–1256.

(60) Vogt, F.; Stein, A.; Rettemeier, G.; Krott, N.; Hoffmann, R.; vom Dahl, J.; Bosserhoff, A.-K.; Michaeli, W.; Hanrath, P.; Weber, C.; Blindt, R. Long-Term Assessment of a Novel Biodegradable Paclitaxel-Eluting Coronary Polylactide Stent. *Eur. Heart J.* **2004**, *25* (15), 1330–1340.

(61) Matsumoto, D.; Shinke, T.; Geva, S.; Chronos, N.; Jabara, R. Stent Degradation of Novel Fully Bioabsorbable Salicylate-Based Sirolimus-Eluting Stent Evaluated By Oct in Pig Coronary Artery. *J. Am. Coll. Cardiol.* **2010**, *55* (10), A217.E2058.

(62) POLLMAN, M. J. Engineering a Bioresorbable Stent: REVA Programme Update. *EuroIntervention 5*.

(63) Jabara, R.; Chronos, N.; Robinson, K. Novel Bioabsorbable Salicylate-Based Polymer as a Drug-Eluting Stent Coating. *Catheter. Cardiovasc. Interv.* **2008**, *72* (2), 186–194.

(64) Garlotta, D. A Literature Review of Poly (Lactic Acid). **2002**, *9* (2).

(65) Ulery, B. D.; Nair, L. S.; Laurencin, C. T. Biomedical Applications of Biodegradable Polymers. **2011**, *49* (12), 832–864.

(66) Xu, H. H. K.; Weir, M. D.; Simon, C. G. Injectable and Strong Nano-Apatite Scaffolds for Cell/Growth Factor Delivery and Bone Regeneration. *Dent. Mater.* **2008**, *24* (9), 1212–1222.

(67) Hyon, S.; Jamshidi, K.; Ikada, Y. Synthesis of Polylactides with Different Molecular Weights. *Biomaterials* **1997**, *18* (22), 1503–1508.

(68) Jamshidi, K.; Hyon, S. H.; Ikada, Y. Thermal Characterization of Polylactides. *Polymer (Guildf).* **1988**, *29* (April), 2229–2234.

(69) de Mel, A.; Jell, G.; Stevens, M. M.; Seifalian, A. M. Biofunctionalization of Biomaterials for Accelerated in Situ Endothelialization: A Review. *Biomacromolecules* **2008**, *9* (11), 2969–2979.

(70) Milleret, V.; Hefti, T.; Hall, H.; Vogel, V.; Eberli, D. Influence of the Fiber Diameter and Surface Roughness of Electrospun Vascular Grafts on Blood Activation. *Acta Biomater.* **2012**, *8* (12), 4349–4356.

(71) Park, J. Y.; Gemmell, C. H.; Davies, J. E. Platelet Interactions with Titanium: Modulation of Platelet Activity by Surface Topography. *Biomaterials* **2001**, *22* (19), 2671–2682.

(72) Hecker, J. F.; Scandrett, L. A. Roughness and Thrombogenicity of the Outer Surfaces of Intravascular Catheters. *J. Biomed. Mater. Res.* **1985**, *19* (4), 381–395.

(73) Trigwell, S.; Hayden, R. D.; Nelson, K. F.; Selvaduray, G. Effects of Surface Treatment on the Surface Chemistry of NiTi Alloy for Biomedical Applications. **1998**, *489* (February), 483–489.

(74) Eliaz, N.; Nissan, O. Innovative Processes for Electropolishing of Medical Devices Made of Stainless Steels. **2007**, *7* (9).

(75) Dalby, M. J.; Marshall, G. E.; Johnstone, H. J. H.; Affrossman, S.; Riehle, M. O. Interactions of Human Blood and Tissue Cell Types with 95-Nm-High Nanotopography. *IEEE Trans. Nanobioscience* **2002**, *1* (1), 18–23.

(76) Chong, D. S. T.; Lindsey, B.; Dalby, M. J.; Gadegaard, N.; Seifalian, a M.; Hamilton, G. Luminal Surface Engineering, "Micro and Nanopatterning": Potential for Self Endothelialising Vascular Grafts? *Eur. J. Vasc. Endovasc. Surg.* **2014**, *47* (5), 566–576.

(77) Koh, L. B.; Rodriguez, I.; Venkatraman, S. S. The Effect of Topography of Polymer Surfaces on Platelet Adhesion. *Biomaterials* **2010**, *31* (7), 1533–1545.

(78) Chen, L.; Han, D.; Jiang, L. On Improving Blood Compatibility: From Bioinspired to Synthetic Design and Fabrication of Biointerfacial Topography at Micro/nano Scales. *Colloids Surf. B. Biointerfaces* **2011**, *85* (1), 2–7.

(79) Zorlutuna, P.; Rong, Z.; Vadgama, P.; Hasirci, V. Influence of Nanopatterns on Endothelial Cell Adhesion: Enhanced Cell Retention under Shear Stress. *Acta Biomater.* **2009**, *5* (7), 2451–2459.

(80) Biela, S. a; Su, Y.; Spatz, J. P.; Kemkemer, R. Different Sensitivity of Human Endothelial Cells, Smooth Muscle Cells and Fibroblasts to Topography in the Nano-Micro Range. *Acta Biomater.* **2009**, *5* (7), 2460–2466.

(81) Liliensiek, S. J.; Wood, J. a; Yong, J.; Auerbach, R.; Nealey, P. F.; Murphy, C. J. Modulation of Human Vascular Endothelial Cell Behaviors by Nanotopographic Cues. *Biomaterials* **2010**, *31* (20), 5418–5426.

(82) Morgan, J. T.; Wood, J. a; Shah, N. M.; Hughbanks, M. L.; Russell, P.; Barakat, A. I.; Murphy, C. J. Integration of Basal Topographic Cues and Apical Shear Stress in Vascular Endothelial Cells. *Biomaterials* **2012**, *33* (16), 4126–4135.

(83) Guillem-Marti, J.; Delgado, L.; Godoy-Gallardo, M.; Pegueroles, M.; Herrero, M.;

Gil, F. J. Fibroblast Adhesion and Activation onto Micro-Machined Titanium Surfaces. *Clin. Oral Implants Res.* **2013**, *24* (7), 770–780.

(84) Lu, J.; Rao, M. P.; MacDonald, N. C.; Khang, D.; Webster, T. J. Improved Endothelial Cell Adhesion and Proliferation on Patterned Titanium Surfaces with Rationally Designed, Micrometer to Nanometer Features. *Acta Biomater.* **2008**, *4* (1), 192–201.

(85) Mucklich, F.; Lasagni, A.; Daniel, C. Laser Interference Metallurgy – Using Interference as a Tool for Micro/nano Structuring. *Int. J. Mater. Res* **2006**, *97*, 1337–1344.

(86) Hans, M.; Müller, F.; Grandthyll, S.; Hüfner, S.; Mücklich, F. Applied Surface Science Anisotropic Wetting of Copper Alloys Induced by One-Step Laser Micro-Patterning. **2012**, *263*, 416–422.

(87) Chu, P. K.; Chen, J. Y.; Wang, L. P.; Huang, N. Plasma-Surface Modification of Biomaterials. **2002**, *36*, 143–206.

(88) Siow, K. S.; Britcher, L.; Kumar, S.; Griesser, H. J. Plasma Methods for the Generation of Chemically Reactive Surfaces for Biomolecule Immobilization and Cell Colonization - A Review. *Plasma Process. Polym.* **2006**, *3* (6–7), 392–418.

(89) Jordá-Vilaplana, a.; Fombuena, V.; García-García, D.; Samper, M. D.; Sánchez-Nácher, L. Surface Modification of Polylactic Acid (PLA) by Air Atmospheric Plasma Treatment. *Eur. Polym. J.* **2014**, *58*, 23–33.

(90) Att, W.; Hori, N.; Iwasa, F.; Yamada, M.; Ueno, T.; Ogawa, T. The Effect of UV-Photofunctionalization on the Time-Related Bioactivity of Titanium and Chromium-Cobalt Alloys. *Biomaterials* **2009**, *30* (26), 4268–4276.

(91) Miller, D. C.; Thapa, A.; Haberstroh, K. M.; Webster, T. J. Endothelial and Vascular Smooth Muscle Cell Function on Poly(lactic-Co-Glycolic Acid) with Nano-Structured Surface Features. *Biomaterials* **2004**, *25* (1), 53–61.

(92) Serrano, M. C.; Portolés, M. T.; Vallet-Regí, M.; Izquierdo, I.; Galletti, L.; Comas, J. V.; Pagani, R. Vascular Endothelial and Smooth Muscle Cell Culture on NaOH-Treated Poly(epsilon-Caprolactone) Films: A Preliminary Study for Vascular Graft Development. *Macromol. Biosci.* **2005**, *5* (5), 415–423.

(93) Koo, G.-H.; Jang, J. Surface Modification of Poly(lactic Acid) by UV/Ozone Irradiation. *Fibers Polym.* **2009**, *9* (6), 674–678.

(94) Zinger, O.; Anselme, K.; Denzer, A.; Habersetzer, P.; Wieland, M.; Jeanfils, J.; Hardouin, P.; Landolt, D. Time-Dependent Morphology and Adhesion of Osteoblastic Cells on Titanium Model Surfaces Featuring Scale-Resolved Topography. *Biomaterials* **2004**, *25* (14), 2695–2711.

(95) Castellanos, M. I.; Zenses, A.-S.; Grau, A.; Rodríguez-Cabello, J. C.; Gil, F. J.; Manero, J. M.; Pegueroles, M. Biofunctionalization of REDV Elastin-like Recombinamers Improves Endothelialization on CoCr Alloy Surfaces for Cardiovascular Applications. *Colloids Surfaces B Biointerfaces* **2015**, *127*, 22–32.

(96) Nyanhongo, G. S.; Rodríguez, R. D.; Prasetyo, E. N.; Caparrós, C.; Ribeiro, C.; Sencadas, V.; Lanceros-Mendez, S.; Acero, E. H.; Guebitz, G. M. Bioactive Albumin Functionalized Polylactic Acid Membranes for Improved Biocompatibility. *React. Funct. Polym.* **2013**, *73* (10), 1399–1404.

(97) Pellis, A.; Herrero Acero, E.; Ferrario, V.; Ribitsch, D.; Guebitz, G. M.; Gardossi, L. The Closure of the Cycle: Enzymatic Synthesis and Functionalization of Bio-Based Polyesters. *Trends Biotechnol.* **2016**, *34* (4), 316–328.

(98) Pellis, A.; Silvestrini, L.; Scaini, D.; Coburn, J. M.; Kaplan, D. L.; Herrero, E.; Guebitz, G. M. Enzyme-Catalyzed Functionalization of Poly (L-Lactic Acid) for Drug Delivery Applications. *Process Biochem.* **2016**, 1–20.

(99) Ortner, A.; Pellis, A.; Gamerith, C.; Orcal Yebra, A.; Scaini, D.; Kaluzna, I.; Mink, D.; de Wildeman, S.; Herrero Acero, E.; Guebitz, G. M. Superhydrophobic Functionalization of Cutinase Activated Poly(lactic Acid) Surfaces. *Green Chem.* **2017**.

(100) Doi, Y.; Steinbüchel, A. *Polyesters III, Applications and Commercial Products (Biopolymers, Vol. 4)*; 2002.

(101) Tsuji, H.; Ikada, Y. Properties and Morphology of Poly (L -Lactide). II . Hydrolysis in Alkaline Solution. *J. Polym. Sci. Part A-Polymer Chem.* **1997**, *36*, 59–66.

(102) Shishoo, R. Plasma Treatment - Industrial Applications and Its Impact on the C & L Industry. *J. Coat. Fabr.* **1996**, *26*, 26–35.

(103) Rasal, R. M.; Janorkar, A. V; Hirt, D. E. Progress in Polymer Science Poly (Lactic Acid) Modifications. *Prog. Polym. Sci.* **2010**, *35* (3), 338–356.

(104) Pellis, A.; Acero, E. H.; Weber, H.; Obersriebnig, M.; Breinbauer, R.; Srebotnik, E.; Guebitz, G. M. Biocatalyzed Approach for the Surface Functionalization of poly(L-

Lactic Acid) Films Using Hydrolytic Enzymes. *Biotechnol. J.* **2015**, *10* (11), 1739–1749.

(105) Labay, C. TREATMENT OF TEXTILE SURFACES BY PLASMA TECHNOLOGY FOR BIOMEDICAL APPLICATIONS, 2014.

(106) Bohner, M.; Lemaitre, J. Can Bioactivity Be Tested in Vitro with SBF Solution? *Biomaterials* **2009**, *30* (12), 2175–2179.

(107) Siebers, M. C.; ter Brugge, P. J.; Walboomers, X. F.; Jansen, J. a. Integrins as Linker Proteins between Osteoblasts and Bone Replacing Materials. A Critical Review. *Biomaterials* **2005**, *26* (2), 137–146.

(108) Hynes, R. O. Integrins : Bidirectional , Allosteric Signaling Machines In Their Roles as Major Adhesion Receptors , Integrins. **2002**, *110* (Table 1), 673–687.

(109) Humphries, J. D.; Byron, A.; Humphries, M. J. Integrin Ligands at a Glance. *J. Cell Sci.* **2006**, *119*, 3901–3903.

(110) Short, S. M.; Talbott, G. a; Juliano, R. L. Integrin-Mediated Signaling Events in Human Endothelial Cells. *Mol. Biol. Cell* **1998**, *9* (8), 1969–1980.

(111) Collo, G.; Pepper, M. S. Endothelial Cell Integrin alpha5beta1 Expression Is Modulated by Cytokines and during Migration in Vitro. *J. Cell Sci.* **1999**, *112*, 569–578.

(112) Davis, G. E.; Senger, D. R. Endothelial Extracellular Matrix: Biosynthesis, Remodeling, and Functions during Vascular Morphogenesis and Neovessel Stabilization. *Circ. Res.* **2005**, *97* (11), 1093–1107.

(113) Broggini, N.; Tosatti, S.; Ferguson, S. J.; Schuler, M.; Textor, M.; Bornstein, M. M.; Bosshardt, D. D.; Buser, D. Evaluation of Chemically Modified SLA Implants (modSLA) Biofunctionalized with Integrin (RGD)- and Heparin (KRSR)-Binding Peptides. *J. Biomed. Mater. Res. A* **2012**, *100* (3), 703–711.

(114) Go, D. H.; Joung, Y. K.; Park, S. Y.; Park, Y. D.; Park, K. D. Heparin-Conjugated Star-Shaped PLA for Improved Biocompatibility. *J. Biomed. Mater. Res. A* **2008**, *86* (3), 842–848.

(115) Ahn, Y. K.; Jeong, M. H.; Kim, J. W.; Kim, S. H.; Cho, J. H.; Cho, J. G.; Park, C. S.; Juhng, S. W.; Park, J. C.; Kang, J. C. Preventive Effects of the Heparin-Coated Stent on Restenosis in the Porcine Model. *Catheter. Cardiovasc. Interv.* **1999**, *48* (3), 324–330.

(116) De Scheerder, I.; Wang, K.; Wilczek, K.; Meuleman, D.; Van Amsterdam, R.; Vogel, G.; Piessens, J.; Van de Werf, F. Experimental Study of Thrombogenicity and Foreign Body Reaction Induced by Heparin-Coated Coronary Stents. *Circulation* **1997**, *95* (6), 1549–1553.

(117) Hynd, M. R.; Frampton, J. P.; Dowell-Mesfin, N.; Turner, J. N.; Shain, W. Directed Cell Growth on Protein-Functionalized Hydrogel Surfaces. *J. Neurosci. Methods* **2007**, *162* (1–2), 255–263.

(118) McKenna, C. J.; Camrud, a R.; Sangiorgi, G.; Kwon, H. M.; Edwards, W. D.; Holmes, D. R.; Schwartz, R. S. Fibrin-Film Stenting in a Porcine Coronary Injury Model: Efficacy and Safety Compared with Uncoated Stents. *J. Am. Coll. Cardiol.* **1998**, *31* (6), 1434–1438.

(119) Hersel, U.; Dahmen, C.; Kessler, H. RGD Modified Polymers: Biomaterials for Stimulated Cell Adhesion and beyond. *Biomaterials* **2003**, *24* (24), 4385–4415.

(120) Aparicio, C.; Gil, F. J.; Planell, J. A.; Engel, E. Human-Osteoblast Proliferation and Differentiation on Grit-Blasted and Bioactive Titanium for Dental Applications. *J. Mater. Sci. Mater. Med.* **2002**, *13* (12), 1105–1111.

(121) Pierschbacher, M. D.; Ruoslahti, E. Variants of the Cell Recognition Site of Fibronectin That Retain Attachment-Promoting Activity. *Proc. Natl. Acad. Sci. U. S. A.* **1984**, *81* (19), 5985–5988.

(122) Plow, E. F.; Pierschbacher, M. D.; Ruoslahti, E.; Marguerie, G. a; Ginsberg, M. H. The Effect of Arg-Gly-Asp-Containing Peptides on Fibrinogen and von Willebrand Factor Binding to Platelets. *Proc. Natl. Acad. Sci. U. S. A.* **1985**, *82* (23), 8057–8061.

(123) Friedlander, D. R.; Hoffman, S.; Edelman, G. M. Functional Mapping of Cytotactin: Proteolytic Fragments Active in Cell-Substrate Adhesion. *J. Cell Biol.* **1988**, *107* (6 Pt 1), 2329–2340.

(124) Receptors, I. Cell Attachment to Thrombospondin : The Role of. **1988**, *107* (6).

(125) Zheng, W.; Wang, Z.; Song, L.; Zhao, Q.; Zhang, J.; Li, D.; Wang, S.; Han, J.; Zheng, X.-L.; Yang, Z.; Kong, D. Endothelialization and Patency of RGD-Functionalized Vascular Grafts in a Rabbit Carotid Artery Model. *Biomaterials* **2012**, *33* (10), 2880–2891.

(126) Hoesli, C. a; Garnier, A.; Juneau, P.-M.; Chevallier, P.; Duchesne, C.; Laroche, G. A Fluorophore-Tagged RGD Peptide to Control Endothelial Cell Adhesion to

Micropatterned Surfaces. *Biomaterials* **2014**, *35* (3), 879–890.

(127) Jun, H.-W.; West, J. Development of a YIGSR-Peptide-Modified Polyurethaneurea to Enhance Endothelialization. *J. Biomater. Sci. Polym. Ed.* **2004**, *15* (1), 73–94.

(128) Jun, H.-W.; West, J. L. Endothelialization of Microporous YIGSR/PEG-Modified Polyurethaneurea. *Tissue Eng.* **2005**, *11* (7–8), 1133–1140.

(129) Jun, H.-W.; West, J. L. Modification of Polyurethaneurea with PEG and YIGSR Peptide to Enhance Endothelialization without Platelet Adhesion. *J. Biomed. Mater. Res. B. Appl. Biomater.* **2005**, *72* (1), 131–139.

(130) Taite, L. J.; Yang, P.; Jun, H.; West, J. L. Nitric Oxide-Releasing Polyurethane – PEG Copolymer Containing the YIGSR Peptide Promotes Endothelialization With Decreased Platelet Adhesion. **2007**, 25–29.

(131) Moruno, C. M.-; Espanol, M.; Montufar, E. B.; Mestres, G.; Aparicio, C.; Gil, F. J.; Ginebra, M. P. *BIOMATERIALS SURFACE SCIENCE. Bioactive Ceramic and Metallic Surfaces for Bone Engineering*; Wiley Online Library, 2013.

(132) Kantlehner, M.; Finsinger, D.; Meyer, J.; Schaffner, P.; Jonczyk, A.; Diefenbach, B.; Nies, B.; Kessler, H. Selective RGD-Mediated Adhesion of Osteoblasts at Surfaces of Implants. *Angew. Chemie Int. Ed.* **1999**, *38* (4), 560–562.

(133) Mas-Moruno, C.; Dorfner, P. M.; Manzenrieder, F.; Neubauer, S.; Reuning, U.; Burgkart, R.; Kessler, H. Behavior of Primary Human Osteoblasts on Trimmed and Sandblasted Ti6Al4V Surfaces Functionalized with Integrin αvβ3-Selective Cyclic RGD Peptides. *J. Biomed. Mater. Res. A* **2013**, *101* (1), 87–97.

(134) Banerjee, I.; Pangule, R. C.; Kane, R. S. Antifouling Coatings: Recent Developments in the Design of Surfaces That Prevent Fouling by Proteins, Bacteria, and Marine Organisms. *Adv. Mater.* **2011**, *23* (6), 690–718.

(135) Hirano, Y.; Mooney, D. J. Peptide and Protein Presenting Materials for Tissue Engineering. *Adv. Mater.* **2004**, *16* (1), 17–25.

(136) Lewis, J. A.; Smay, J. E.; Stuecker, J.; Cesarano, J. Direct Ink Writing of Three-Dimensional Ceramic Structures. *J. Am. Ceram. Soc.* **2006**, *89* (12), 3599–3609.

(137) Smay, J. E.; Cesarano, J.; Lewis, J. a; Iii, J. C. Colloidal Inks for Directed Assembly of 3-D Periodic Structures Colloidal Inks for Directed Assembly of 3-D Periodic Structures. *East* **2002**, *18* (June), 5429–5437.

(138) Franco, J.; Hunger, P.; Launey, M. E.; Tomsia, A. P.; Saiz, E. Direct Write Assembly

of Calcium Phosphate Scaffolds Using a Water-Based Hydrogel. *Acta Biomater.* **2010**, *6* (1), 218–228.

(139) Lode, A.; Meissner, K.; Luo, Y.; Sonntag, F.; Glorius, S.; Nies, B.; Vater, C.; Despang, F.; Hanke, T.; Gelinsky, M. Fabrication of Porous Scaffolds by Three-Dimensional Plotting of a Pasty Calcium Phosphate Bone Cement under Mild Conditions. *J. Tissue Eng. Regen. Med.* **2010**, *4* (8), 682–693.

(140) Guo, S. Z.; Gosselin, F.; Guerin, N.; Lanouette, A. M.; Heuzey, M. C.; Therriault, D. Solvent-Cast Three-Dimensional Printing of Multifunctional Microsystems. *Small* **2013**, *9* (24), 4118–4122.

Chapter II: Aims and scope of the work

Stenting is the most commonly performed procedure for the treatment of coronary atherosclerotic lesions and, according to medical diagnostic, BMSs, DESs or BRSs will be implanted. Both bare-metal CoCr and polymeric PLLA stents are widely used thanks to their excellent biocompatibility and optimal mechanical and corrosion properties. However, serious clinical complications remain, such ISR and LST, mainly due to delayed and poor reendothelialization of the surface. Surface modification is an excellent strategy to improve stent clinical results by enhancing endothelialization. Within this context, the global aim of this PhD thesis is to investigate new strategies of CoCr alloy and PLLA surface modification in order to control ECs and platelet response, and consequently, reduce ISR and LST rates after stent implantation. We believe that nano- and micro- patterning, biofunctionalization and chemical functionalization of stent surface could be potential strategies to induce an accelerated reendothelization of the stents. To that end, it will be studied different surface modification strategies on flat CoCr samples and on PLLA films. Moreover, the feasibility to fabricate BRSs by 3D printing will be also considered. The thesis has been divided into the three following strategies.

Strategy 1: Design of different linear patterns using DLIP technique on CoCr alloy for cardiovascular applications and study their effect on ECs and platelets response. The following subgoals were considered:

- **Fabrication of nano-micro patterned CoCr alloy surfaces** with DLIP technique. Creation of linear patterned CoCr surfaces with different periodicities and depths. Characterization of the topographical, chemical and physical properties of the obtained surfaces.
- **Biological characterization of the patterned CoCr surfaces.** Study of the ECs and platelets adhesion response.

Strategy 2: Modification of CoCr alloy surfaces with a combination of linear patterning obtained by DLIP technique and biofunctionalization with RGD and YIGSR peptides to study the effect of both treatments in ECs adhesion, migration and proliferation. The following subgoals were considered:

- **Biofunctionalization of flat CoCr surfaces.** Activation and biofunctionalization with RGD and YIGSR by covalent bonding through silanization. Characterization of the topographical, chemical and physical properties of the obtained surfaces.
- **Biological characterization of the biofunctionalized CoCr surfaces.** Study of the ECs adhesion, proliferation and migration response.
- **Biofunctionalization of patterned CoCr surfaces.** Activation and biofunctionalizion of the DLIP patterned CoCr surfaces with RGD and YIGSR by covalent bonding through silanization.
- **Biological characterization of the biofunctionalized and patterned.** Study of the ECs adhesion, proliferation and migration response.

Strategy 3: Elaboration of solvent-casted PLLA functionalized surfaces to enhance ECs adhesion and to assess the use of this process and biomaterial to fabricate 3D-printed BRS.

The following subgoals were considered:

- **Fabrication of PLLA films by solvent casting with enhanced mechanical properties.** Optimization of the composition and the thermal treatments to fabricate PLLA films by solvent casting with mechanical and degradation properties comparable to actual BRSs. Characterization of the chemical, physical, mechanical and degradation properties.
- **Functionalization of PLLA surface.** Optimization and generation of carboxyl groups on PLLA surface by oxygen plasma, NaOH etching and cutinase enzyme hydrolysis. Characterization of the chemical, physical and degradation properties.
- **Biological characterization of the functionalized PLLA surfaces.** Study of the ECs adhesion response.
- **Fabrication of PLLA BRSs by 3D printing.** Feasibility assessment of the fabrication of PLLA BRSs by the solvent-cast direct writes technique.

Chapter III: Direct Laser Interference Patterning of CoCr Alloy Surfaces to Control Endothelial Cell and Platelet Response for Cardiovascular Applications

1. Introduction

DLIP is a one-step technique that offers the possibility to obtain nano- depth (< 40 nm) patterns [1]. Patterns are generated by the interaction of multiple laser beams onto the sample's surface. In the case of metals, photothermal interaction is the responsible for the pattern formation. This results in the production of precise and distinct topographical and/or chemical surface patterns. DLIP has already shown promising results by inducing cells spreading and alignment on various biomaterials [2,3]. We hypothesize that DLIP could be a useful strategy to produce modified stents that would promote faster endothelium recovery without increasing thrombus formation.

The aim of this work is to obtain different linear patterns using DLIP on CoCr alloy for cardiovascular applications and study their effect on ECs and platelets response. Different pattern periodicities were designed according to ECs dimensions when adhering to metallic surfaces [4–7]. Moreover, two different pattern depths were produced to evaluate their effect on platelet adhesion. The properties of modified CoCr surfaces were thoroughly characterized and EC and platelet response were examined *in vitro*.

2. Materials and methods

2.1. Materials

CoCr discs of 10 mm diameter and 2 mm thick were obtained from a cylindrical bar of CoCr alloy ASTM F90 (51 % Co, 20% Cr, 15% W,10% Ni, 3% Fe) (Technalloy, Spain), abraded with silicon carbide grinding papers (P240, P600, P1200, P2500 and P4000 from Neuertek S.A., Spain) and finally polished with suspensions of 1 µm and 0.05 µm alumina in distilled water (Buehler, Germany), until achieving smooth mirror-like surfaces (Ra < 10 nm). All polished samples were ultrasonically cleaned with cyclohexane, isopropanol, ethanol, Milli-Q® water and acetone for 5 min. Finally, samples were dried with nitrogen.

Human umbilical vein endothelial cells (HUVECs) (Lonza Group Ltd., Switzerland) were grown in EC basal medium (EBM®) supplemented with 4% (v/v) fetal bovine serum (FBS), 0.1% (v/v) gentamicin sulphate amphotericin (GA-1000), 0.4% (v/v) recombinant human fibroblast growth factor (rhFGF), 0.1% (v/v) recombinant human epidermal growth factor (rhEGF), 0.1% (v/v)

ascorbic acid, 0.1% (v/v) vascular endothelial growth factor (VEGF), 0.1% (v/v) recombinant Long R insulin (R3-IGF-1) and 0.04% (v/v) hydrocortisone (EBM and all supplements were obtained from Lonza). Cells were maintained at 37°C, in a humidified atmosphere containing 5% (v/v) CO_2. The culture medium was changed every 2 days. Cell culture was performed in Nunc cell flasks (Thermo Fisher Scientific, USA) in completed medium. Upon reaching 70% confluence, cells were detached by trypsin/EDTA (Sigma-Aldrich), centrifuged and subcultured into a new flask or re-suspended in a serum-free medium and used for cell assays. All experiments were conducted using HUVECs at passages 4 to 8 [8,9].

Whole blood samples were obtained from three healthy volunteers who had not taken any drugs affecting platelet function in the previous 10 days and minimally anticoagulated with citrate/phosphate/dextrose solution at a final citrate concentration of 19 mM (100 mM sodium citrate, 16 mM citric acid, 18 mM sodium hydrogen phosphate and 130 mM dextrose).

2.2. DLIP technique

A Nd:YAG laser (Spectra Physics Quanta-Ray PRO 290, Germany) with a fundamental wavelength of 1064 nm was used to modify the CoCr surfaces topography. Samples were structured at λ = 355 nm (third harmonic generation) in order to increase the energy absorbed by the CoCr surface. Repetition rate and pulse duration of the laser were 10 Hz and 10 ns. A mechanical shutter (Uniblitz Electronic, USA) was used for pulse number adjustment and a Solo 2 laser power & energy meter (Gentec-eo, Canada) was placed on the laser beam trajectory to control and measure the power, from which fluency was calculated. A beam splitter was used to split the primary laser beam into two sub-beams. Three mirrors were used in different positions to make the 2 laser beams interfere on the sample surface with different angles (**Figure III.1**). Interfering two coherent beams results in a line-like interference pattern with a periodicity P related to the angle 2α between the two beams through the equation: $P = \lambda / (2 * \sin(\alpha))$. A 1×1 mm^2 quadratic mask was placed just before the sample in order to use only the central part of the laser spot. The complete sample surface was structured with multiple, adjacent spots of 1×1 mm^2. The laser treatment was performed at

normal atmospheric conditions using a single laser pulse. Further details of the experimental setup have already been published elsewhere [10].

Patterns with four different periodicities 3 µm (3), 10 µm (10), 20 µm (20) and 32 µm (32) were generated by modifying the angle. Also, laser fluency was varied to induce differences in the structure depth. Fluencies inferior to 1 J/cm^2 were applied to generate low depth structures < 40 nm (L-pattern) and fluencies superior to 1.65 J/cm^2 were used to obtain high depth structures > 600 nm (H-pattern). Thus, eight different surfaces with linear patterns were obtained: 3L, 10L, 20L, 32L, 3H, 10H, 20H and 32H.

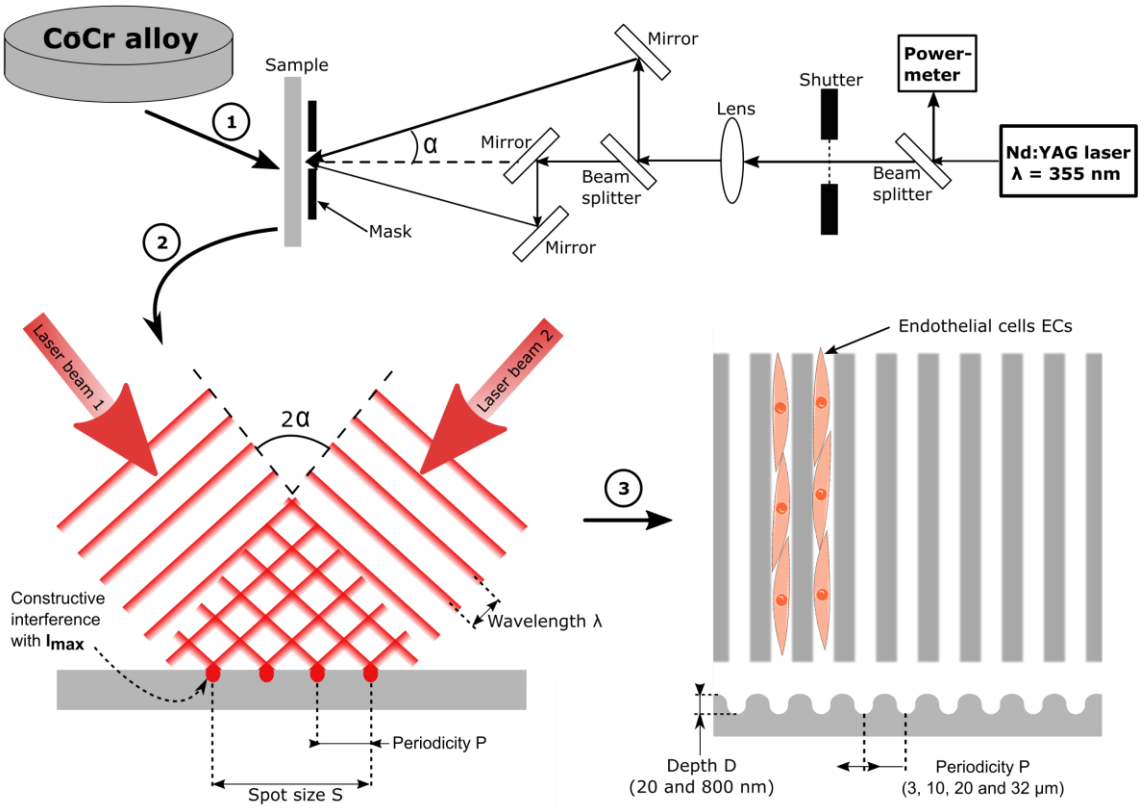

Figure III.1: *Fabrication steps of patterned CoCr surfaces by DLIP: 1) Configuration of the experimental DLIP setup; 2) Schema of the interference of the two laser beams onto CoCr flat surfaces; 3) Front- and top-view of the modified CoCr surfaces and simulation of the expected ECs adhesion orientation following the patterning.*

2.3. Physico-chemical characterization

2.3.1. Surface topography

Surface morphology of the samples was analyzed by scanning electron microscopy (SEM) with a Zeiss Neon40 FE-SEM microscope (Carl Zeiss NTS

GmbH, Germany) with an acceleration voltage of 5 kV and at a working distance of 6 mm. For each series, fifteen images from three different samples were obtained at 5000x magnification.

Topography was evaluated with white light interferometry (WLI) (Optical interferometer VeecoWyko 9300NT, Veeco Instruments, USA) in vertical scanning interferometry mode (VSI) at 100x magnification. Data analysis was performed with Wyko Vision 4.10 software (Veeco Instruments). Curvature and tilt were eliminated from every surface analysis with a Gaussian filter. Different parameters were quantified: periodicity (P); depth (D); aspect ratio P/D, roughness parameter $S_{a\text{-micro}}$ (the arithmetic average height at a micro scale) and percentage of resolified surface.

Also, nano-roughness of CoCr samples were analyzed by atomic force microscopy (AFM) (Dimension 3100, Veeco Digital Instruments, Bruker, Germany). Height and amplitude images were recorded simultaneously in tapping-mode in air using a silicon Tap150al-G cantilever (NanoWorld Group, Neuchâtel, Switzerland) at a scan rate of 1 Hz. Peaks and valleys areas of 1x1 μm^2 were analysed for CTR and patterned CoCr surfaces to obtain $S_{a\text{-nano-peak}}$ and $S_{a\text{-nano-valley}}$, respectively.

2.3.2. Chemical characterization

The chemical composition of CoCr surfaces before and after the topographical modification was analysed by X-ray photoelectron spectroscopy (XPS) (SPECS Surface NanoAnalysis GmbH, Berlin, Germany). The XPS spectra were obtained using an Mg anode XR50 operating at 150W and a Phoibos 150 MCD-9 detector to record high resolution spectra at a pressure below 7.5×10^{-9} mbar. The elements present on the surface were evaluated by low-resolution survey spectra, whereas high-resolution of some elements (C 1s, O 1s, Cr 2p, Co 2p) were recorded with detector pass energy fixed at 25 eV with 0.1 eV step at a pressure below 7.5×10^{-9} mbar. Casa XPS software (Version 2.3.16, Casa Software Ltd., Teignmouth, UK) was used to do fitting, peak integration of spectra and peaks deconvolution. Binding energies were referred to the C 1s signal at 284.8 eV.

To determine metallic oxide layer thickness, TEM lamellae for CTR, 10L and 10H samples were prepared with the aid of a dual beam workstation, consisting

of a focused ion beam (FIB, Carl Zeiss NTS GmbH, Germany) used for site-specific milling, and a SEM to image the samples. For TEM lamellae preparation, a Platinum-band (Pt) was deposited in-situ on the surface, first by electron and then by ion beam. The Pt-band aims to protect the surface during the ion milling steps, thereby ensuring the preservation of the original condition of the surfaces. The TEM investigations were carried out using a Jeol JEM 2010 at 200kV.

Raman spectra were recorded with a Renishaw Qontor invia Raman microscope (Renishaw plc,Gloucestershire, UK) at 532 nm and 2400 $l.mm^{-1}$ grid. A 100x magnifying microscope objective was used. For CTR, 3L and 3H eleven Raman spectra were taken along a line perpendicular to the laser patterning with a distance of 1 µm between each spot. In order to remove the background the remove background tool of Crystal Sleuth software was applied to all the spectra.

2.3.3. Surface wettability

Static contact angle was measured by sessile drop method with the video-based system Contact AngleSystem OCA15plus (Dataphysics, Germany). Drops were generated with a micrometric syringe and deposited on the substrate surface. Milli-Q® water contact angle was measured on modified CoCr surfaces following the perpendicular (Θx_{eq}) and parallel (Θy_{eq}) directions to the patterns. For each condition, it was measured 20-25 drops of 3 µl each and the contact angle values were obtained after applying Laplace-Young fitting of the drop profile with SCA 20 software (Dataphysics). Since the samples were not smooth, Wenzel equation was applied to obtain the intrinsic contact angle (θ): $\cos(\theta_{eq})=r*\cos(\theta)$ where r is the index area: real surface area / projected surface area. Finally, the difference between the parallel and the perpendicular contact angle was calculated as $\Delta\theta = |\theta x - \theta y|$, as a parameter to quantify the surface anisotropy.

2.4. Biological characterization

2.4.1. Blood perfusion assay

Platelet adhesion studies were carried out using a flat chamber perfusion system [11–13], where two samples can be tested in parallel. CoCr samples of ≈170 µm thickness were prepared for each perfusion and patterned CoCr surfaces were aligned with the blood flow. Blood from 3 volunteer donors, was circulating

through the perfusion chamber at a shear rate of 800 s^{-1} during 5 min at 37ºC [13]. After perfusion, samples were rinsed thrice with 0.15 M PBS. To stain the platelets by fluorescence, adherent platelets were fixed with 2.5% glutaraldehyde in 0.15 M PBS at 4ºC during 24 h. Then, blocking step was performed with a solution of 1 % BSA (w/v) in PBS for 15 min at room temperature (RT) with orbital agitation at 100 rpm. Primary antibody monoclonal mouse anti-human CD36 (1:2000) (Clone 185-1G2, Lifespan, Biosciences, USA) was incubated in 1 % BSA (w/v) in PBS for 1 h. Samples were washed thrice with PBS during 5 min and then, the surfaces were incubated with secondary antibody donkey anti-mouse IgG- AF 594 (1:500) in 1 % BSA (w/v) in PBS for 1 h in dark. Finally, samples were washed with PBS and Milli-Q® water and mounted on microscope slides with Prolong Gold Antifade reagent (Thermo Fisher Scientific, USA). Surfaces were examined by AF7000 fluorescence microscopy (Leica). Images at 10 X magnification from the entire sample surface were acquired and analysed with FIJI Image J software by measuring the percentage of the surface covered with platelets and the average size of the aggregates. Finally, platelets were fixed with glutaraldehyde (G400-4, Sigma-Aldrich) and dehydrated through immersion in different solutions of ethanol in order to observe platelet aggregates with more details by scanning electron microscopy (SEM) with a Zeiss Neon40 FE-SEM microscope (Carl Zeiss NTS GmbH, Germany). For each sample, five images were taken at a working distance of 6 mm and a potential of 5 kV.

2.4.2. Cell adhesion

Cell adhesion assay was performed by seeding HUVEC at a density of 5 x 10^4 cells/disk with serum-free medium and cellular analyses were carried out at 12 h after cell seeding. The different CoCr samples were previously sterilised in ethanol 70% during 15 min at RT. Polished CoCr was used as a control.

To quantify the density of adhered HUVECs the release of lactate dehydrogenase (LDH) enzyme was measured at the specified culture time. For that purpose, cells were lysed with 350 µl/disk of mammalian protein extraction reagent (M-PER) (Thermo Fisher Scientific, USA) and the activity of LDH was measured by means of a conventional colorimetric assay (Cytotoxicity Detection Kit, Roche Diagnostics, Mannheim, Germany). The reduction in tetrazolium salts into formazan dye, an enzymatic reaction coupled to LDH activity, was measured

spectrophotometrically at 490 nm using the microplate reader Infinite M200 PRO (Tecan Group Ltd., Switzerland). A calibration curve with decreasing number of cells was performed to express the obtained absorbance results as cell number. To characterize HUVECs alignment and spreading, staining of nuclei and actin fibers was performed by immunofluorescence. Briefly, adhered cells were fixed with 4% (w/v) paraformaldehyde (PFA) for 30 min and permeabilized with 0.05% (w/v) Triton X-100 in PBS at room temperature for 20 min and washed with 20 mM glycine in PBS (×3). Samples were blocked with 1% BSA (w/v) in PBS for 30 min. Next, cells were dark incubated with phalloidin-rhodamine (1:300; Invitrogen, USA) for one hour. After, samples were washed with 20 mM glycine in PBS (×3) and nuclei were counterstained with DAPI (1:1000; Invitrogen) in dark during 2 min. Finally, samples were mounted in Mowiol 4−88 (Sigma-Aldrich) on microscope slides before visualizing in an AF7000 fluorescence microscope (Leica, Germany). Images at 10 X magnification from the entire sample surface were stitched and cell spreading and morphology was determined by measuring three different characteristics: cells mean area, cells aspect ratio (maximum ratio of length and width of a bounding rectangle for the cell) and percentage of aligned cells (percentage of cells with an angle inferior to 30 % between the cell orientation and the pattern lines) using FIJI ImageJ software [14]. Once analyzed, CoCr samples were ultrasonically cleaned in PBS and adhered cells were fixed with glutaraldehyde (G400-4, Sigma-Aldrich) and dehydrated through immersion in different solutions of ethanol in order to observe in more in detail the cells shape by SEM. For each sample, five images were taken at a working distance of 6 mm and a potential of 5 kV.

2.4.3. Cell migration

To evaluate the process of wound healing and cell migration onto CTR, 10L and 10H CoCr surfaces, HUVECs were stained with the cell membrane fluorescent linker PKH67 (PKH67-GL, Sigma-Aldrich) 24 h prior to wound healing assays. Before cell culture, CoCr samples were sterilized in ethanol 70% for 20 min at RT. The wound healing processes were reproduced by placing an Ibidi culture-insert (Ibidi, Germany) on top of each sample. On the patterned surfaces the Ibidi insert was placed in order to have the gap perpendicular to the patterns lines. Thus, a suspension of 20 000 labelled cells/disk were placed at both chambers of the

insert with complete medium, and incubated for 24 h until reaching a confluent HUVEC adhesion. After, the insert was removed creating a cell-free gap of 500 µm ± 50 µm. The surfaces were cleaned twice with PBS to remove non-adhered cells and thus, filled with complete medium. HUVEC cell migration was recorded using a fluorescence stereomicroscope (Leica MZ16F, Leica microsystems, Germany) combined with the camera DFC 300 FX (Leica Microsystems). Gap images were acquired for all the samples at 0 h and 48 h. The non-covered area for each CoCr disk was calculated with FIJI Image J software and the percentage of gap recovery was calculated for each series.

2.5. Statistical analysis

The experimental data collected in this chapter are reported as mean ± standard deviation. A one-way analysis of variance (ANOVA) was used to determine the statistical significance of difference at $p<0.05$ (Minitab 16.2.2 Statistical Software, Minitab Inc.). Unless previously specified, all physicochemical characterization and cell culture experiments were performed with n=3 samples for each specimen group for each assay used in this study. In addition, each experiment was repeated at least twice.

3. Results and discussion

3.1. Physico-chemical characterization

3.1.1. Surface topography

For the first time, CoCr surfaces were modified creating controlled patterns of different widths and depths by DLIP technique as observed by SEM (**Figure III.2**) and analysed by white light interferometry (WLI) (**Figure III.3** and **Table III.1**). Modifying laser beams incident angle and fluency allowed to obtain four different periodicities 3 µm (3), 10 µm (10), 20 µm (20) and 32 µm (32) and two different depths: low depth structures < 40 nm (L-pattern) and high depth structures > 600 nm (H-pattern). Thus, eight different surfaces with linear patterns were obtained: 3L, 10L, 20L, 32L, 3H, 10H, 20H and 32H. In order to minimize platelet adhesion and aggregation, L-pattern surfaces were designed to have a very low depth and roughness while H-pattern series were intended to enhance HUVECs alignment and adhesion. As reported by other authors, when the surface

roughness is sufficiently low, it is expected that platelets do not sense roughness and do not adhere to these substrates [15,16]. In contrast, H-patterned surfaces are considerably rougher than CTR and L-pattern series and its depth is higher than 600 nm which was expected to control ECs adhesion [17,18].

Generally, the modified surfaces present a linear pattern except for 32L which shows linear circular waves. As expected, H-pattern series present higher depths compared to L-pattern and peaks and valleys are well defined and homogeneous; whereas L-pattern series present less defined structures than H-pattern.

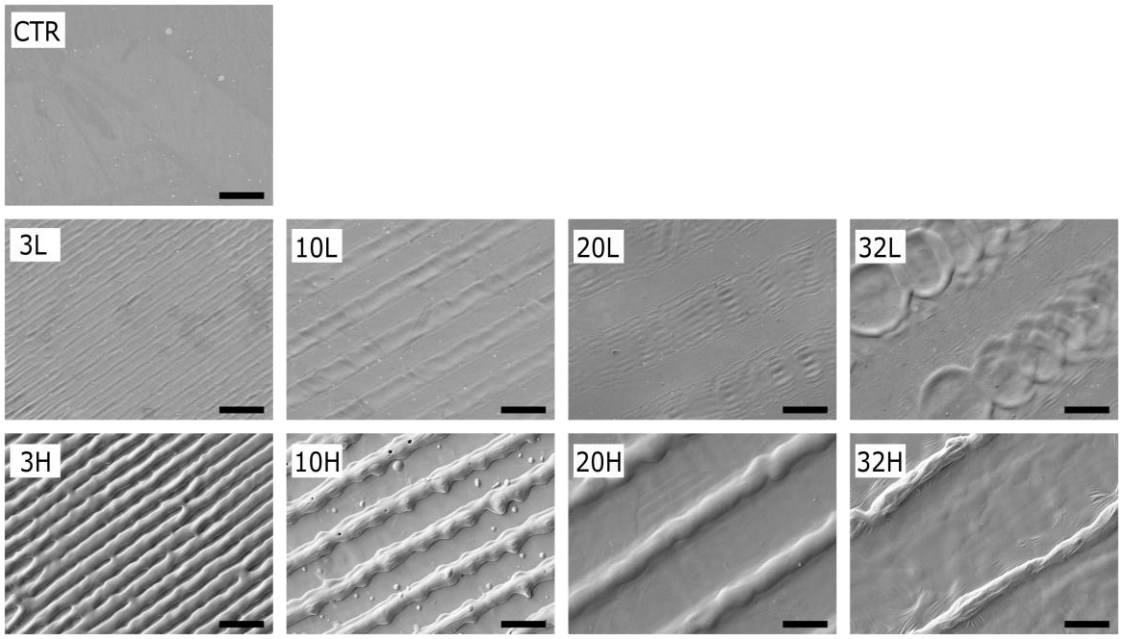

Figure III.2: *SEM images of plain CoCr (CTR) and the different patterned structures obtained by DLIP. Scale bar = 10 µm.*

To understand the generation of peaks by DLIP technique onto CoCr surfaces, **Figure III.3** shows the cross-section WLI profile of surfaces 32H and 32L as an example that can be translated to the others surface patterns. The profile of 32H surfaces presents one valley in front of the constructive interference and one single peak in front of the destructive interference. H-pattern surfaces present only a peak for each periodicity, as confirmed by SEM and WLI, and the overall surface is composed of melted CoCr. On the other hand, L-pattern series are composed of a small valley at the constructive interferences area, accompanied by small peaks at both sides of this valley, and a non-modified and non-melted flat area at the destructive interference areas.

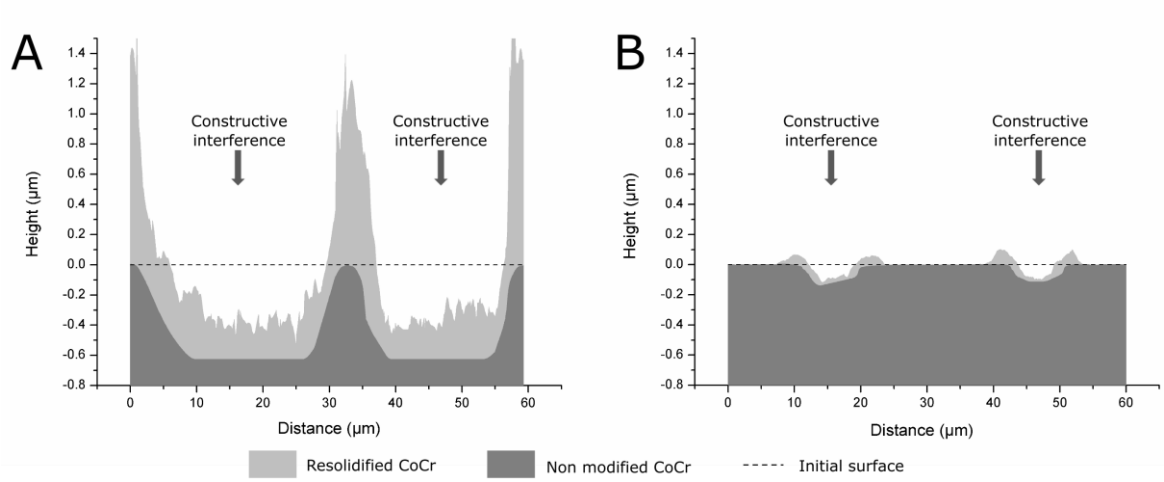

Figure III.3: *WLI cross-section profiles superposition of 32H (A) and 32L (B) surfaces: i) initial surface (dot line); ii) final patterned surface (light grey); iii) estimated non-modified CoCr (dark grey). Constructive interferences are indicated with arrows.*

Table III.1: *Surface topography and wettability parameters of CTR and patterned CoCr surfaces measured by WLI, AFM and contact angle. Different columns correspond to: Laser fluency, periodicity (P), depth (D), aspect ratio (P/ D), arithmetic roughness average ($S_{a\text{-}micro}$, $S_{a\text{-}nano\text{-}peak}$, $S_{a\text{-}nano\text{-}valley}$), percentage of resolidified surface, intrinsic contact angle perpendicular to pattern direction (Θx), intrinsic contact angle parallel to pattern (Θy) and ΔΘ = |Θx - Θy|.*

			Surface topography							Wettability		
	Surfaces	Laser Fluency	P	D	Aspect Ratio P/D	$S_{a\text{-}micro}$	$S_{a\text{-}nano\text{-}peak}$	$S_{a\text{-}nano\text{-}valley}$	Resolidified surface	Θx	Θy	ΔΘ
		J/cm2	µm	nm	-	nm	nm	nm	%	º	º	º
	CTR	-	-	-	-	7.4 ± 5.3	0.63 ± 0.32		0	70.3 ± 3.0		0.0
Low	3L	0.91	3.4 ± 0.1	5.6 ± 0.7	614.3	27.4 ± 6,3	0.60 ± 0.17	0.67 ± 0.25	68 ± 9	80.2 ± 3.8	78.9 ± 6.1	1.3
Low	10L	0.81	10.0 ± 0.1	30.1 ± 9.3	330.8	28.2 ± 12.5	0.70 ± 0.33	0.50 ± 0.15	65 ± 7	78.5 ± 8.8	79.4 ± 9.3	0.9
Low	20L	0.93	19.5 ± 0.1	25.8 ± 9.6	757.5	15.8 ± 1.1	0.57 ± 0.20	0.68 ± 0.22	64 ± 6	81.1 ± 4.6	81.3 ± 3.6	0.2
Low	32L	0.93	32.5 ± 0.3	34.1 ± 11.0	925.3	33.4 ± 11.9	0.69 ± 0.15	0.63 ± 0.20	68 ± 11	80.4 ± 6.9	79.8 ± 6.4	0.6
High	3H	1.65	3.4 ± 0.0	636.8 ± 132.3	5.4	174.9 ± 28.0	0.72 ± 0.21	0.51 ± 0.14	100 ± 0	80.1 ± 5.0	76.7 ± 8.8	3.4
High	10H	2.42	10.0 ± 0.1	733.6 ± 104.6	13.4	299.8 ± 35.9	0.68 ± 0.21	0.69 ± 0.19	100 ±0	93.0 ± 7.0	82.6 ± 6.1	10.4
High	20H	3.21	19.5 ± 0.1	963.0 ± 109.2	20.3	279.0 ± 31.6	0.62 ± 0.27	0.67 ± 0.19	97 ± 2	93.7 ± 4.5	84.6 ± 5.4	9.1
High	32H	5.00	32.4 ± 0.4	997.8 ± 124.8	32.5	264.9 ± 65.7	0.55 ± 0.18	0.58 ± 0.15	98 ± 2	99.4 ± 6.8	88.8 ± 7.1	10.6

Table III.1 summarizes the analysed parameters of the different surfaces with WLI and AFM technique. For L-pattern, it has been used a low laser fluency, between 0.81 and 0.93 J/cm^2, whereas, for H-patterns it was necessary a higher fluency between 1.65 and 5 J/cm^2. WLI confirmed the modification of CoCr surfaces to be very reproducible for each of the generated periodicities (3, 10, 20

and 32 µm). As expected, the different series show extreme depths ranging from 5.6 to 34.1 µm for L-pattern surfaces and from 636.8 to 997.8 µm for H-pattern. These depth differences on L- and H-patterns lead to a very different aspect ratio P/D around 800 and 20, respectively. Concerning $S_{a\text{-micro}}$ parameter, L-pattern surfaces show a roughness slightly higher to CTR and H-pattern presented, at least, values of $S_{a\text{-micro}}$ 20 times higher than CTR. On the contrary, $S_{a\text{-nano-peak}}$ and $S_{a\text{-nano-valley}}$ obtained from AFM images (**Figure III.4** and **Table III.1**) on all patterned surfaces presented no statistical differences compared to $S_{a\text{-nano}}$ on CTR, indicating that DLIP technique did not modify the nano-roughness at peaks or valleys of the studied surfaces.

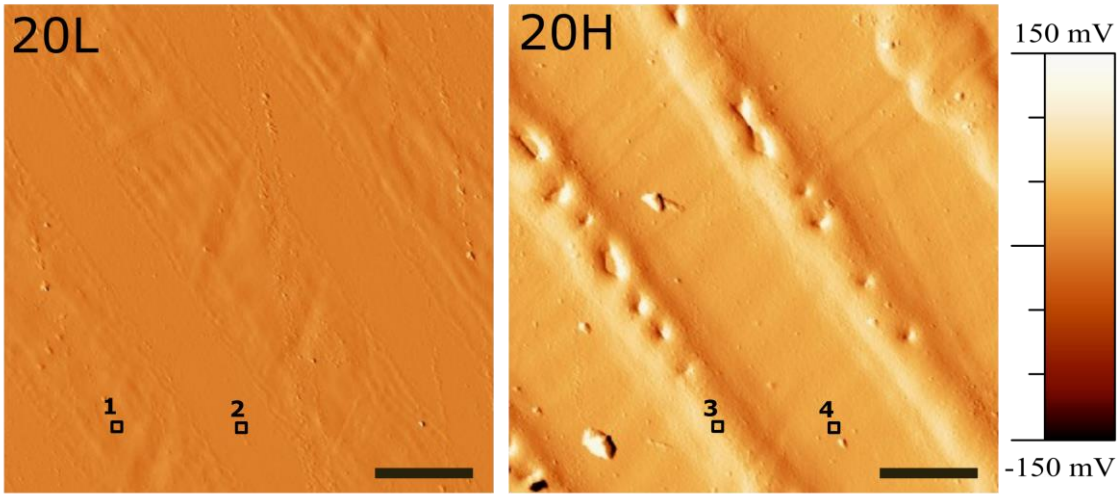

Figure III.4: *AFM analysis of 20L and 20H surfaces to characterize the patterns topographical properties. AFM amplitude images of 20L and 20H surfaces. Scale bar = 10 µm. Black squares 1, 2, 3 and 4 represent the studied 1x1 µm areas to obtain $S_{a\text{-nano-peak}}$(10L), $S_{a\text{-nano-valley}}$(10L), $S_{a\text{-nano-peak}}$(10L), $S_{a\text{-nano-valley}}$(10L), respectively.*

The analysis of the percentage of resolidified surface indicates that L-patterns have between 64 and 68%, while, H-patterns present values higher than 97%. Specifically, 3H and 10H surfaces have 100% of resolidified surface and 20H and 32H, only present, respectively, 3 and 2% of non-modified surface. DLIP technique applied to metals generates melting of the surface layer at the constructive interference and the molten metal flows to the destructive interference zone due to the surface tension gradient induced by the difference of temperatures [19,20]. If the applied fluency is enough, two consecutive constructive interferences can melt enough material to form a single peak between them and consequently, cover the entire surface with molten and

resolidified material. According to SEM images and WLI profiles, this is the process that occurred with the H-patterned series. Indeed, these structures presented a clear single-peak pattern associated with a surface almost fully covered by resolidified metal. On the other hand, as observed by SEM images and WLI profile, the low fluency used for the L-surface series generated lower metal melting fronts, which did not join in a single peak. Then, two peaks were obtained as a result from two consecutive constructive interferences and less than 68% of the surface was covered by resolidified metal.

3.1.2. Chemical characterization

Surface chemical composition of the studied CoCr surfaces is shown in **Table III.2**. XPS analysis revealed the presence of Co 2p, Cr 2p, C 1s and O 1s. The atomic percentage of C 1s increased while O 1s decreased for patterned surfaces compared to CTR. The relatively high percentage of C 1s detected in all studied surfaces was associated with the presence of organic contaminants from the air. All patterned surfaces present higher content in Co 2p compared to CTR, whereas, Cr 2p element increased only for L-pattern and 3H. The relationship between the two principal elements was measured by the ratio Co/Cr, which increased from 0.37, for CTR up to 2.02 in the case of 32H. This increase of the Co/Cr ratio was correlated to the laser fluency used to obtain the patterned surfaces. Indeed for the surfaces patterned with the lowest fluency (0.91 J/cm^2) Co/Cr ratio increased up to two times compared to CTR (i.e. 0.8 and 0.4 for 10L and CTR respectively) and up to five times (2.0 for 32H) for the surfaces patterned with the highest fluency (5 J/cm^2). This higher amount of Co found at the surface could be explained by the higher diffusivity of Co compared to Cr at high temperatures generated by DLIP [21].

The deconvolution of the high-resolution Co 2p and Cr 2p peaks has been applied for all the samples. The ratios between the metallic fraction and the oxide fraction for Co and Cr elements, Co/Co_xO_y and Cr/Cr_2O_3 can be visualized in **Table III.2**. Co_xO_y corresponds to CoO or Co_3O_4 oxides, which have equal energy binding peaks at 779.7 eV [22,23]. **Figure III.5** shows the comparison between the deconvolution of the Co 2p peak of CTR, 20L and 20H.

Table III.2: *Analysis of the atomic composition percentage at the CTR and patterned surfaces by XPS. Values of O 1s, C 1s, Co 2p, Cr 2p and ratio between Co/Cr and metallic/oxide fraction for Co 2p (Co/Co_xO_y) and Cr 2p (Cr/Cr_2O_3) obtained from the deconvolution of Co 2p and Cr 2p peaks. Co_xC_y corresponds to CoO or Co_3O_4 oxides.*

	Surfaces	Elemental composition (atomic %)				Co/Cr	Co/Co_xO_y	Cr/Cr_2O_3
		O 1s	C 1s	Co 2p	Cr 2p			
	CTR	52.4	36.5	3.0	8.1	0.4	1.09	0.09
Low	**3L**	25.2	51.4	9.3	14.1	0.7	0.29	0.05
	10L	24.9	49.9	11.6	13.7	0.8	0.27	0.06
	20L	35.1	46.8	7.6	10.5	0.7	0.25	0.07
	32L	24.9	51.4	13.2	10.5	1.3	0.15	0.05
High	**3H**	26.3	53.4	9.1	11.3	0.8	0.17	0.04
	10H	52.8	39.4	4.5	3.3	1.4	0.00	0.00
	20H	44.0	45.9	6.1	4.0	1.5	0.00	0.00
	32H	33.9	52.0	9.5	4.7	2.0	0.00	0.00

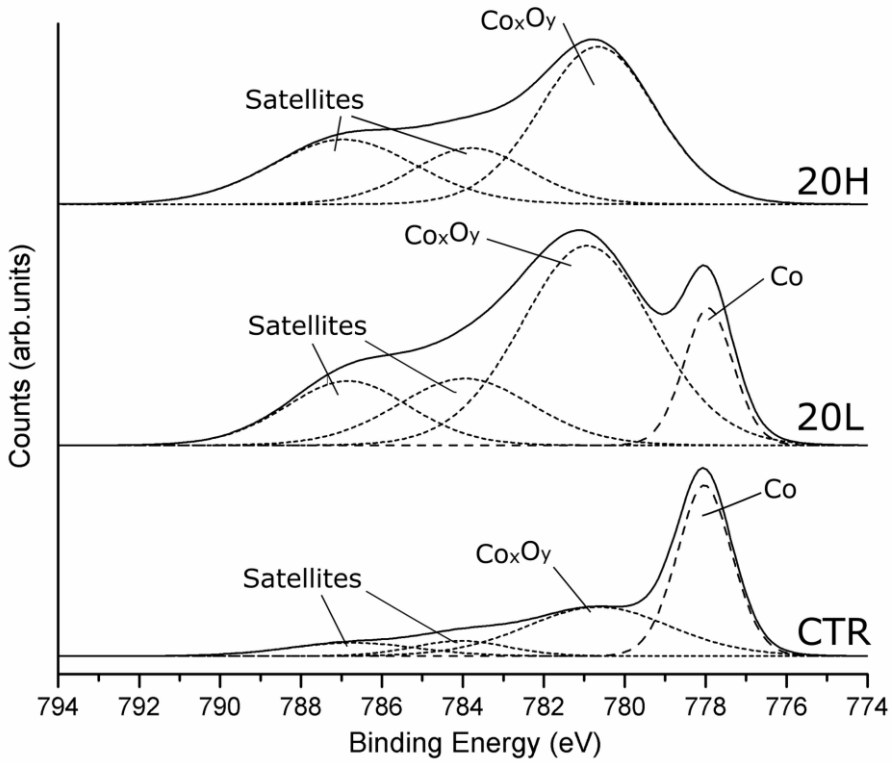

Figure III.5: *High-resolution spectra of Co 2p for CTR, 20L and 20H surfaces obtained by XPS. Dashed lines represent the deconvoluted peaks.*

When determining changes in the ratio Co/Co_xO_y, XPS showed an increase of this parameter depending on the used laser fluency. XPS analyses a 10 nm layer

of the material, and therefore the Co/Co_xO_y ratio of 1.09 observed for the CTR sample means that there is approximately the same amount of metallic cobalt and cobalt. For 10H, 20H and 32H the ratio was 0 meaning that the oxide layer of these surfaces was thicker than 10 nm. Finally, on L-pattern surfaces, an intermediate situation was found with Co/Co_xO_y ratio around 0.2, suggesting that L-series had an oxide layer thicker than CTR and thinner than H-pattern surfaces. Similar tendencies were obtained with Cr 2p . Indeed, Cr/Cr_2O_3 decrease on L-patterns and 3H compared to CTR and on 10H, 20H and 32H the ratio is null.
Transmission electron microscope (TEM) lamellae were prepared from CTR, 10L and 10H samples to characterize the oxide layer thickness (**Figure III.6**). CTR presented a homogeneous oxide layer of 2.1 nm thickness. After DLIP technique, oxide layer thickness increased slightly on 10L, between 3.1 and 3.9 nm, and, more significantly on 10H, > 11.4 nm. Both 10L and 10H surfaces, did not present differences between peaks and valleys of the topography, suggesting that the oxidation consequence of DLIP technique was homogeneous.

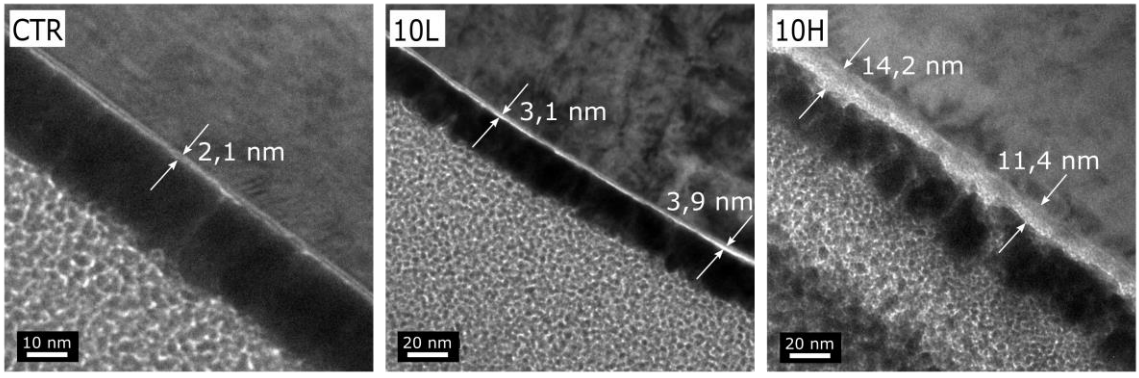

Figure III.6: *TEM investigation of the oxide layer modification during laser structuring of CoCr alloy. High magnification of oxide layer thickness for CTR, 10L and 10H surfaces. The upper part of the images correspond to the CoCr alloy, the black layer correspond to the Pt-band and the bright layer in-between is the oxide layer.*

Raman spectrum profiles were obtained for CTR, 3L and 3H series, by performing the analysis perpendicularly to patterns direction in order to have information about peaks and valleys oxide layer properties (**Figure III.7**). Generally, the analyzed spectrums presented the following peaks: Co_3O_4 at around 190, 470, 510 and 670 cm^{-1} [24,25] and Cr_2O_3 at 250, 510 and 540 cm^{-1} [26,27]. Differences on the intensity of the peaks were detected between the different series. As expected, CTR Raman spectrums presented sharp Co_3O_4 and Cr_2O_3 peaks

indicating that these oxides were crystalline. On 3L and 3H surfaces a significant reduction or disappearance of the previous peaks was observed. As XPS and TEM indicated an increase of the oxide layer thickness on patterned surfaces compared to CTR, the reason for such peaks intensity decrease could be associated with a partial transformation of the crystalline Co_3O_4 and Cr_2O_3 oxide layer to a thicker amorphous oxide layer. As the sample surface is submitted to extremely high temperatures for a short period of time during DLIP [28], it was reasonable to observe amorphous oxide layer on L- and H-pattern surface. Both surfaces, 3L and 3H, did not present significant differences of the Raman spectra between peaks and valleys, confirming the homogeneity of the oxide layer composition all over the surfaces.

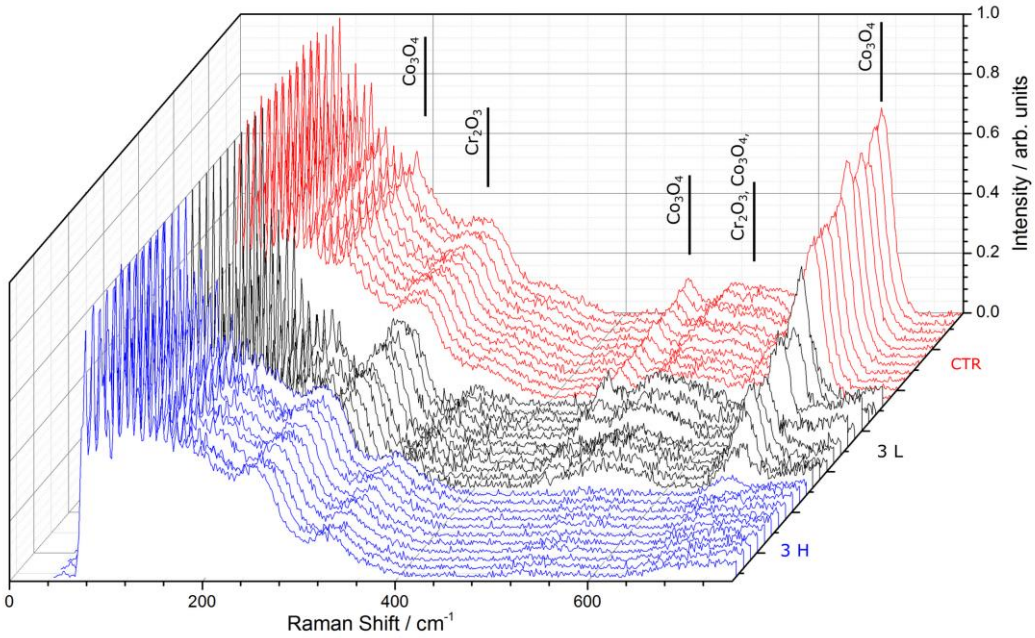

Figure III.7: *Raman spectra measurements results for the CTR (red), 3L (black) and 3H (blue) samples. For all studied conditions, each line corresponds to a Raman spectrum taken along a line perpendicular to the laser patterning with a distance of 1 µm between each spot.*

3.1.3. Surface wettability

The sessile drop method was used to measure the static contact angle of distilled water (Milli-Q®, Merck Millipore, USA) onto patterned CoCr at two orientations, perpendicular and parallel to the patterns lines. Then, the Wenzel equation was used to calculate the intrinsic contact angles of the different surfaces with a surface area index r of 1.0 for CTR and L-patterns and of 1.1 for

H-patterns. **Table III.1** shows the results obtained for both directions and the difference between these two angles.

As observed, CTR surfaces have a contact angle of 70.3 ± 3.0º whereas, all patterned surfaces are more hydrophobic and show values ranging from 76.7º up to 99.4º in both directions. The contact angle increased as the pattern periodicity and depth increased. A previous study demonstrated that a titanium amorphous oxide surface had a more hydrophobic behavior than its respective crystalline oxide structure [29]. In accordance, the hydrophobic effect of CoCr surfaces modified by DLIP technique was a consequence of the generation of an amorphous oxide layer.

$\Delta\theta$, as an indicator of heterogeneity, is null for CTR and very low for L-pattern series; while for H-pattern it is > 3.4º and particularly 10H, 20H and 32H have a significantly higher θx than θy indicating anisotropic wettability on H-pattern.

This effect was visually confirmed through the optical microscopy images (**Figure III.8**). Indeed, on 32L the water droplet is perfectly circular whereas on 10H the drop shows an oval shape depending on the direction of the pattern. The enlarged image of a deposited drop on 10H showed that peaks blocked the water deposition when it was perpendicular to the pattern lines, resulting in oval drop geometry. This anisotropic wettability on laser modified samples was already reported by other authors with Cu and Ti substrates [20,30], suggesting that DLIP topographical patterns induced, in general, an anisotropic wettability on metals which could influence protein adsorption [31] and, indeed, cell spreading.

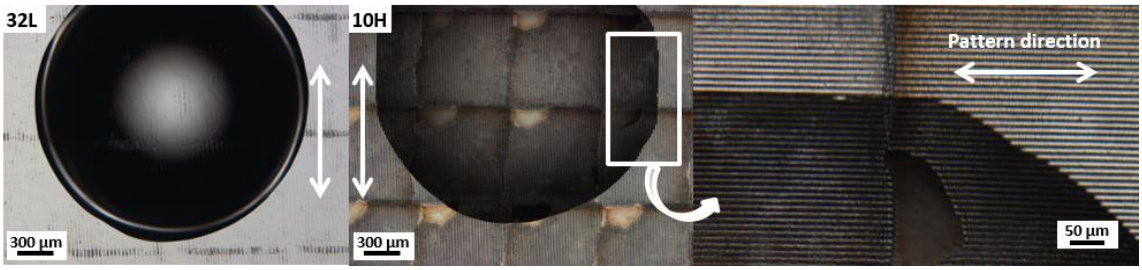

Figure III.8: *Optical microscope images of the deposition of a distilled water drop on 32L and 10H surfaces and an enlarged rotated image of deposited drop on 10H.*

These results prove that DLIP technique allows obtaining surface modification onto metals with very different characteristics. Both, L- and H-pattern surfaces, presented surface modifications such as changes in the oxide chemical

composition, a partial transformation of the structure from a crystalline to a thicker amorphous oxide layer and an increased hydrophobicity. Overall, H-pattern series presented a controlled topographical pattern while L-pattern surfaces had negligible topographical modifications. In fact, L-pattern surfaces can be used as a model of chemical surface modifications without topographic changes for DLIP studies, when it is desired to study separately the effect of chemical properties and topography. In this study, it helped to understand the biological response of HUVECs and platelets on DLIP modified surfaces.

3.2. Biological characterization

3.2.1. Platelet adhesion and aggregation

To evaluate platelet adhesion and aggregate size, all surfaces were placed into a flat perfusion chamber circulating donor's blood at a shear rate of 800 s^{-1} during 5 minutes. Attached platelets were visualized by fluorescent labeling the membrane and also, after dehydration, with SEM (**Figure III.9**). As it is well known, roughness increases platelet adhesion and aggregation [16,32,33]. Thus, it was expected to observe a higher platelet adhesion on DLIP surfaces, particularly on H-pattern. Surprisingly, both H- and L- pattern surfaces presented a statistically significant lower area covered by platelets and lower platelet aggregation size than CTR, irrespective of pattern periodicity. Indeed, CTR showed 33.0 ± 3.7 % of the area covered by platelets whereas all patterned surfaces obtained values lower than 17.4 ± 6.6 %. All patterned CoCr surfaces showed platelets aggregates size lower than 96.7 ± 19.1 μm^2 compared to CTR, 200.6 ± 33.3 μm^2. This behavior was confirmed by SEM images (**Figure III.9**C) where it is observed that platelet aggregates were bigger on CTR than on 10L and 10H, respectively. This behavior was a consequence of chemical or/and topographical surface modifications induced by DLIP onto both, L- and H-patterned surfaces. As DLIP induced negligible topographical modifications, at the nano- and micro-scales, on L-pattern series compared to CTR, topographical modifications cannot explain the reduced platelet adhesion. This was confirmed by SEM images where platelets adhered randomly on peaks and valleys on all patterned surfaces. Consequently, chemical modifications on L- and H-pattern surfaces, in particular changes in oxide layer properties and increased wettability were probably the reasons for such reduction. This was in agreement with

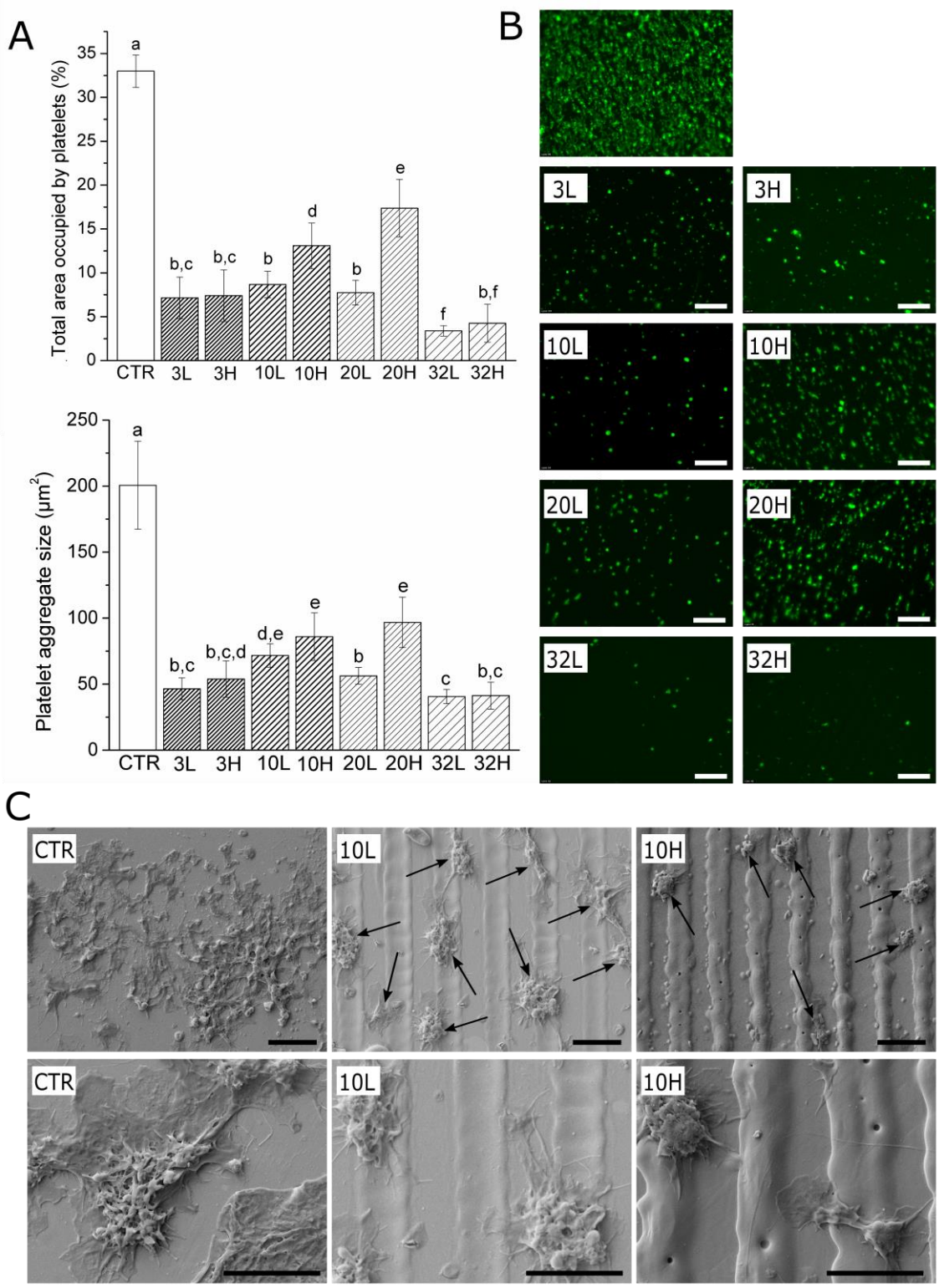

Figure III.9: *Platelet adhesion study on CTR and DLIP patterned surfaces by circulating donor's blood flow during 5 minutes in a flat perfusion chamber at shear rate of 800 s^{-1}. (A) % of the area occupied by platelets and platelet aggregates size measured by fluorescent microscopy. Images were analysed with FIJI software. Columns with different letters belong to statistically different groups (p-value < 0.05). (B) Fluorescence microscopy images of adhered platelets on CTR and patterned surfaces. Bar = 75 µm. (C) SEM images of platelet aggregates on CTR, 10L and 10H surfaces. Black arrows indicate platelet aggregates. Bar = 10 µm.*

previous studies that demonstrated a lower platelet adhesion when the oxide layer thickness increased [34,35] as occurred for patterned surfaces compared to CTR. Oxide layer modifications modulate proteins adsorption onto the biomaterial surface, i.e. fibrinogen and kininogen adsorption and determine platelet adhesion [34,36]. Also, other studies suggested that titanium amorphous oxide could improve blood compatibility or reduce the activation of the clotting cascade compared to a more crystalline metallic oxide [37,38]. Moreover, it was described that for surfaces with a wettability range between 60-100º, platelets adhered preferentially on surfaces with a contact angle around 60º than onto surfaces with 100º wettability [39–41] . This was the behavior of CTR, with a contact angle of 70º compared to patterned series with a higher hydrophobicity, 80-100º. Consequently, the transformation of a CoCr alloy crystalline oxide layer to a thicker amorphous oxide layer and the associated increased hydrophobicity could explain the decrease of platelet adhesion and aggregation onto patterned CoCr surfaces compared to non-modified and smooth surfaces.

3.2.2. Cell adhesion

To characterize the effect of the different DLIP nano-patterned CoCr surfaces on HUVECs adhesion, the number and spreading of adhered HUVECs after overnight incubation was studied by quantifying the LDH activity (**Figure III.10A**) and by immunofluorescence (**Figure III.10B** and **10C**). Cell number and cell area showed no significant differences between all the different surface conditions. Thus, DLIP technique did not affect cell adhesion, confirming the published results of Raimbault et al. [30] on laser modified surfaces. The fact that DLIP technique did not modify the nano-roughness of the surface and, consequently, did not affect protein adsorption could explain the similar adhesion and spreading of HUVEC on the patterned surfaces compared to plain ones. On the other hand, cell aspect ratio was clearly affected by the depth of the patterning. H-patterned surfaces increased HUVECs elongation since a significantly higher aspect ratio (≥ 2.6 ± 0.5) was obtained compared to CTR (1.9 ± 0.2), whereas, L-structures showed no significant differences compared to CTR. Cell elongation is related with the number of HUVECs aligned onto the patterns lines finding a percentage ≥ 67.2 % for H-pattern series and < 36.0 % for CTR and L-pattern. Cells were considered aligned if the angle between the pattern and the cell

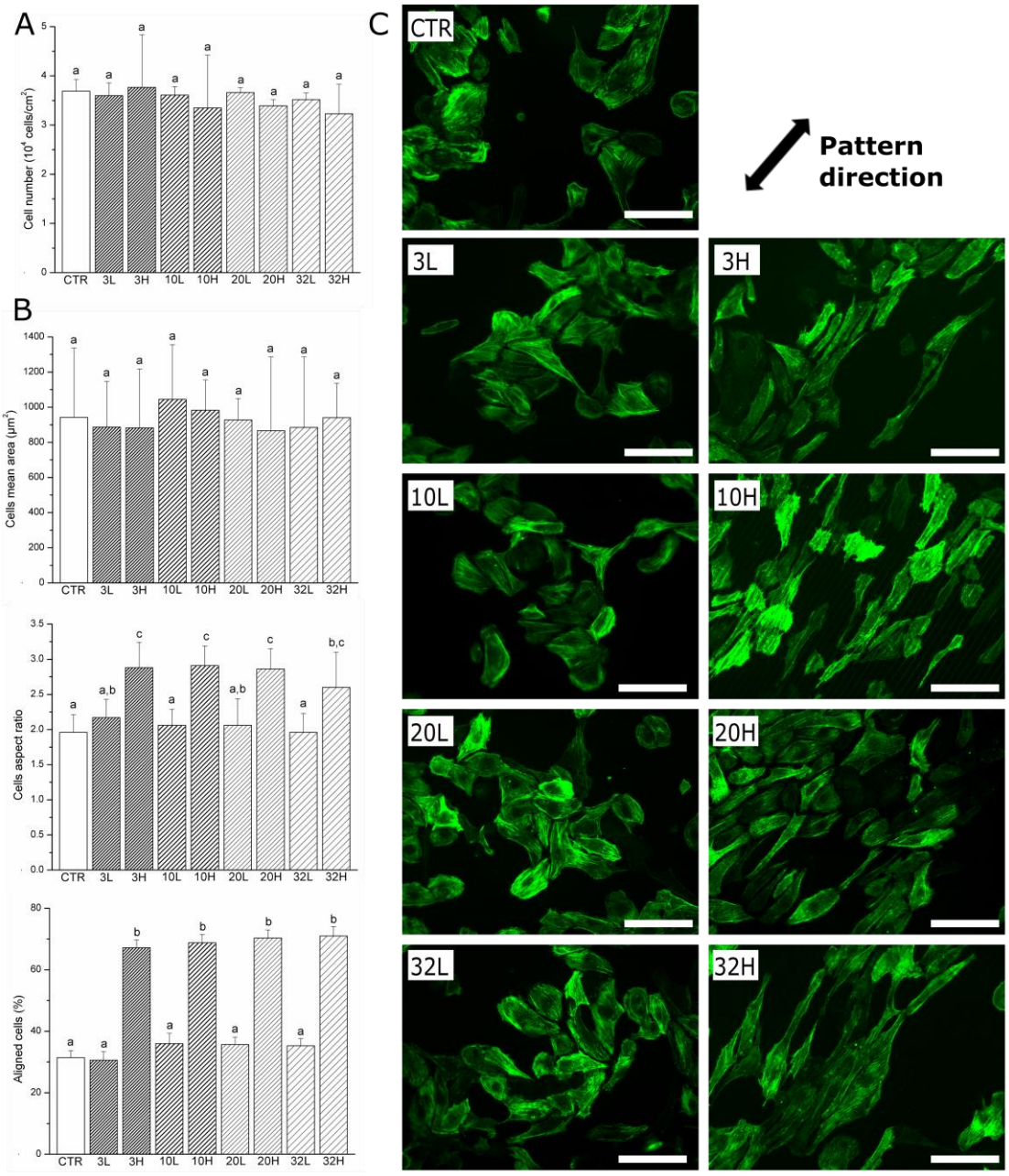

Figure III.10: *HUVECs adhesion and spreading of CTR and patterned CoCr surfaces after 12h of cell culture. (A) Cell number quantified by means of LDH enzymatic assay. Columns with different letters belong to statistically different groups (p-value < 0.05). (B) Cells mean area, cells aspect ratio and % of aligned cells obtained by fluorescent microscopy. Images were analysed with FIJI software. Columns with different letters belong to statistically different groups (p-value < 0.05). (C) F-actin immunostaining of HUVECs on CTR and patterned CoCr surfaces. Black arrow indicates patterns direction. Scale bar = 100 µm.*

preferred direction was less than 30º. Fluorescence images for all conditions confirmed the differences in aspect ratio and number of aligned cells on H-pattern, whereas, L-pattern surfaces presented values similar to CTR. Thus,

despite changes in chemical properties on L-pattern surfaces generated by DLIP, no changes were detected in cell adhesion, spreading and alignment compared to CTR. Consequently, the elongation and alignment of HUVECs observed on H-pattern was attributed to the topographical pattern and to the associated anisotropic wettability. Biela et al. [4] reported similar conclusions showing in particular a higher cell elongation only on linear patterns deeper than 100 nm. Also, Dalby *et al.* demonstrated that cell filopodias can sense topography and act as a trigger for cells alignment onto patterned surfaces with depths down to 50 nm [42]. However, the origin of cells alignment on linear patterned surfaces remains controversial and Fujita *et al.* associated this cell behavior to a faster retraction of cell protrusions perpendicular to pattern direction compared to parallel ones [43]. Also, SEM images (**Figure III.11**) showed HUVECs adhered randomly onto peaks and valleys of L- and H-pattern surfaces.

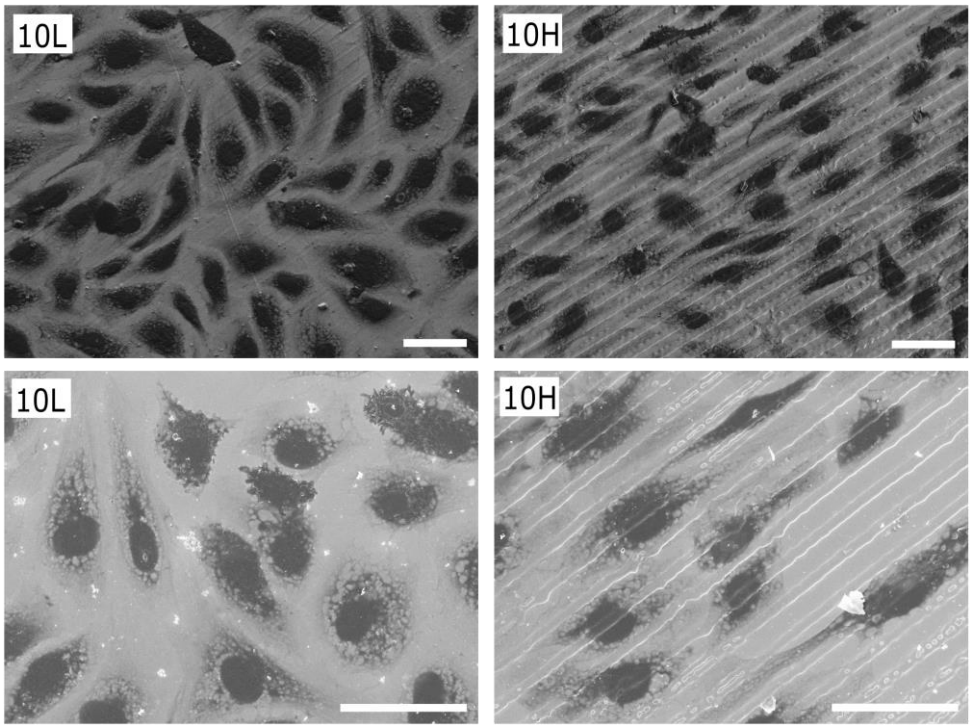

Figure III.11: *HUVECs adhesion and spreading on CoCr surfaces after 12h of incubation. SEM images of HUVECs on 10L and 10H surfaces. Scale bar = 40 µm. Upper images are secondary electron images, whereas lower images were obtained in backscatter electron mode.*

3.2.3. Cell migration

Cell migration was evaluated for CTR, 10L and 10H surfaces through the injury coverage ratio, which was defined as the percentage of injury area covered by HUVEC's after 48 h (**Figure III.12**).

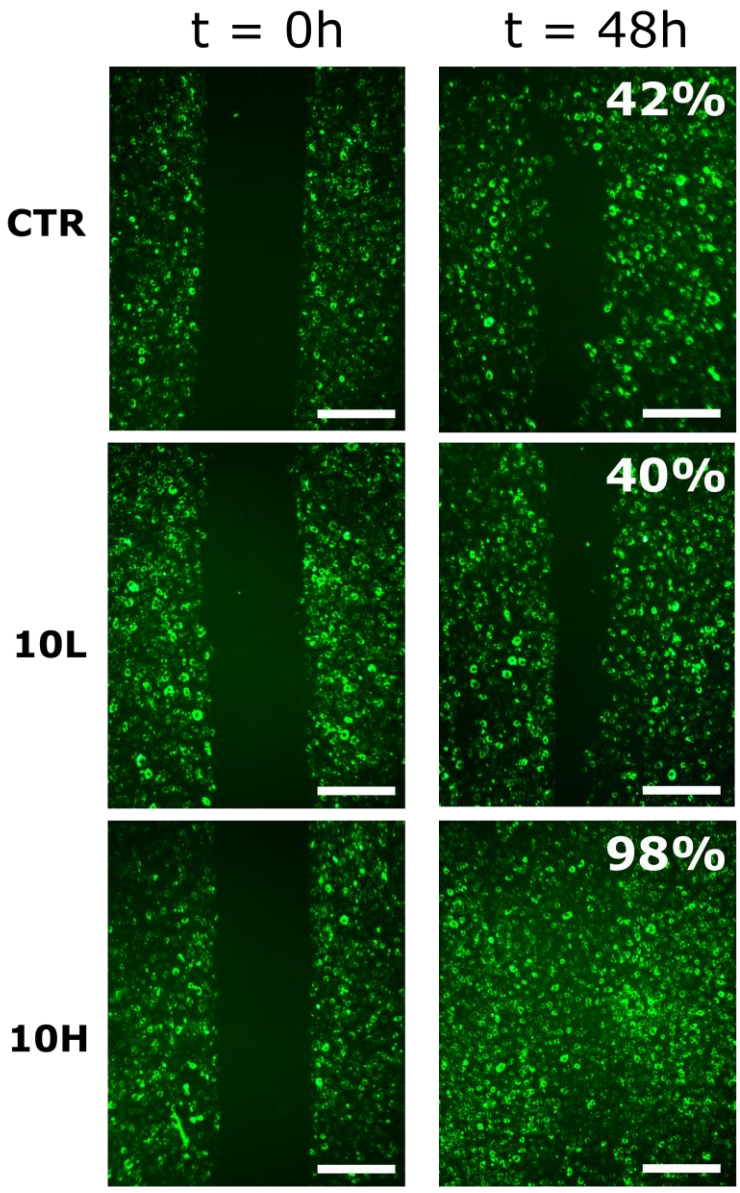

Figure III.12: *HUVECs migration on CTR, 10L and 10H surfaces at 0 h and 48 h timepoints. The percentage indicates the percentage of the respective initial injury area covered by HUVECs at 48 h. Initial gap width = 500 ± 50 µm. Scale bar = 400 µm.*

After 48 h, it was detected significant differences in the migration of HUVECs onto studied surfaces. CTR and 10L series obtained similar values of cell migration with 42 % and 40 %, respectively, suggesting that L-pattern did not have any

effect on HUVECs migration. This result is in agreement with HUVECs adhesion assay where L-pattern surfaces did not have influence on HUVECs adhesion, elongation and alignment due to the negligible micro-roughness of the surface. On the contrary, 10H presented a value of 98% of recovery, indicating an accelerated HUVECs migration due to the pattern topography which enhances HUVECs alignment. Many studies have demonstrated that elongation and alignment of ECs are generally associated with a faster cell migration [4,44–46]. Consequently, CoCr H-pattern surfaces seem to be a promising surface to enhance ECs migration from the healthy artery at the extremities of the stent and a possible candidate to recover a functional endothelium.

To conclude, H-pattern series presented, on one side, topographic patterning, which induces HUVECs elongation, alignment and migration; and, on the other side, chemical modification, which generates low platelet adhesion and aggregation. Consequently, H-pattern CoCr surfaces obtained by DLIP technique could be used as a promising stent surface with a faster artery reendothelialization associated with a reduced platelet aggregation.

4. Conclusions

In this work, we reported a reliable and flexible one-step protocol to, simultaneously, produce a linear pattern and modify the oxide layer properties onto metallic surfaces with the capacity to influence ECs adhesion, alignment and migration as well as platelet adhesion and agglomeration. The DLIP technique allowed us to obtain topographical patterned CoCr surfaces with different periodicities and depths by modifying laser fluency. As a consequence of the very high temperature generated during DLIP, the initial crystalline oxide layer was modified to a thicker amorphous oxide layer more hydrophobic. The L-pattern series presented negligible topographical modification whereas the H-pattern series presented significant topographical pattern. While the L-pattern series did not show a significant effect on HUVECs response, H-pattern series induced HUVECs elongation, alignment and migration due to the topographical pattern. All patterned surfaces reduced platelet adhesion compared to plain CoCr surfaces which indicated that oxide layer structure transformation affected surface thrombogenicity. DLIP H-pattern series with an adequate combination of

topographic and chemical features can influence ECs and platelets response and could be a promising approach to accelerate endothelium recovery and avoid surface thrombosis.

References

(1) Roitero, E.; Lasserre, F.; Anglada, M.; Mücklich, F.; Jiménez-Piqué, E. A Parametric Study of Laser Interference Surface Patterning of Dental Zirconia: Effects of Laser Parameters on Topography and Surface Quality. *Dent. Mater.* **2016**, 10–14.

(2) Günther, D.; Scharnweber, D.; Hess, R.; Wolf-Brandstetter, C.; Grosse Holthaus, M.; Lasagni, A. F. 1 – High Precision Patterning of Biomaterials Using the Direct Laser Interference Patterning Technology. In *Laser Surface Modification of Biomaterials*; 2016; pp 3–33.

(3) Fayou Yu, Frank Mucklich, Ping Li, Hao Shen, S. M.; Claus-Michael Lehr, and U. B. In Vitro Cell Response to a Polymer Surface Micropatterned by Laser Interference Lithography. *Biomacromolecules* **2005**, *6*, 1160–1167.

(4) Biela, S. a; Su, Y.; Spatz, J. P.; Kemkemer, R. Different Sensitivity of Human Endothelial Cells, Smooth Muscle Cells and Fibroblasts to Topography in the Nano-Micro Range. *Acta Biomater.* **2009**, *5* (7), 2460–2466.

(5) Palmaz, J. C.; Benson, A.; Sprague, E. A. Influence of Surface Topography on Endothelialization of Intravascular Metallic Material. *J. Vasc. Interv. Radiol.* **1999**, *10* (4), 439–444.

(6) Castellanos, M. I.; Mas-Moruno, C.; Grau, A.; Serra-Picamal, X.; Trepat, X.; Albericio, F.; Joner, M.; Manero, J. M.; Pegueroles, M. Functionalization of CoCr Surfaces with Cell Adhesive Peptides to Promote HUVECs Adhesion and Proliferation. *Appl. Surf. Sci.* **2016**, *393*, 82–92.

(7) Liu, H.; Pan, C.; Zhou, S.; Li, J.; Huang, N.; Dong, L. Improving Hemocompatibility and Accelerating Endothelialization of Vascular Stents by a Copper-Titanium Film. *Mater. Sci. Eng. C* **2016**, *69*, 1175–1182.

(8) Heng, B. C.; Bezerra, P. P.; Meng, Q. R.; Chin, D. W.-L.; Koh, L. B.; Li, H.; Zhang, H.; Preiser, P. R.; Boey, F. Y.-C.; Venkatraman, S. S. Adhesion, Proliferation, and Gene Expression Profile of Human Umbilical Vein Endothelial Cells Cultured on Bilayered Polyelectrolyte Coatings Composed of Glycosaminoglycans. *Biointerphases* **2010**, *5* (3), 53–62.

(9) Andukuri, A.; Minor, W. P.; Kushwaha, M.; Anderson, J. M.; Jun, H.-W. Effect of

Endothelium Mimicking Self-Assembled Nanomatrices on Cell Adhesion and Spreading of Human Endothelial Cells and Smooth Muscle Cells. *Nanomedicine* **2010**, *6* (2), 289–297.

(10) Mucklich, F.; Lasagni, A.; Daniel, C. Laser Interference Metallurgy – Using Interference as a Tool for Micro/nano Structuring. *Int. J. Mater. Res* **2006**, *97*, 1337–1344.

(11) Muggli, R.; Baumgartner, H. R.; Tschopp, T. B. Automated Microdensitometry and Protein Assays as a Measure for Platelet Adhesion and Aggregation on Collagen-Coated Slides under Controlled Flow Conditions. *J. Lab. Clin. Med.* **1980**.

(12) Sakariassen, K. S.; Aarts, P. A.; de Groot, P. G.; Houdijk, W. P.; Sixma, J. J. A Perfusion Chamber Developed to Investigate Platelet Interaction in Flowing Blood with Human Vessel Wall Cells, Their Extracellular Matrix, and Purified Components. *J. Lab. Clin. Med.* **1983**, *102* (4), 522–535.

(13) Arderiu, G.; Díaz-Ricart, M.; Buckley, B.; Escolar, G.; Ordinas, A.; Arderiu; G; Diaz-Ricart; M; B. Primary Arrest of Circulating Platelets on Collagen Involves Phosphorylation of Syk, Cortactin and Focal Adhesion Kinase: Studies under Flow Conditions. *Biochem. J.* **2002**, *364* (Pt 1), 65–71.

(14) Schindelin, J.; Arganda-Carreras, I.; Frise, E.; Kaynig, V.; Longair, M.; Pietzsch, T.; Preibisch, S.; Rueden, C.; Saalfeld, S.; Schmid, B.; Tinevez, J.-Y. J.-Y.; White, D. J.; Hartenstein, V.; Eliceiri, K.; Tomancak, P.; Cardona, A.; Liceiri, K.; Tomancak, P.; A., C. Fiji: An Open Source Platform for Biological Image Analysis. *Nat. Methods* **2012**, *9* (7), 676–682.

(15) Park, J. Y.; Gemmell, C. H.; Davies, J. E. Platelet Interactions with Titanium: Modulation of Platelet Activity by Surface Topography. *Biomaterials* **2001**, *22* (19), 2671–2682.

(16) Hecker, J. F.; Scandrett, L. A. Roughness and Thrombogenicity of the Outer Surfaces of Intravascular Catheters. *J. Biomed. Mater. Res.* **1985**, *19* (4), 381–395.

(17) Pries, a R.; Secomb, T. W.; Gaehtgens, P. The Endothelial Surface Layer. *Pflugers Arch.* **2000**, *440* (5), 653–666.

(18) Kuwahara, M.; Sugimoto, M.; Tsuji, S.; Matsui, H.; Mizuno, T.; Miyata, S.; Yoshioka, A. Platelet Shape Changes and Adhesion under High Shear Flow. *Arterioscler. Thromb. Vasc. Biol.* **2002**, *22* (2), 329–334.

(19) von Allmen, M.; Blatter, A. *Laser-Beam Interactions with Materials. Physical Principles and Applications*, Springer S.; 1995.

(20) Hans, M.; Müller, F.; Grandthyll, S.; Hüfner, S.; Mücklich, F. Applied Surface Science Anisotropic Wetting of Copper Alloys Induced by One-Step Laser Micro-Patterning. **2012**, *263*, 416–422.

(21) Fowler, D. E.; Rogozik, J.; David E. Fowler and Juergen Rogozik. Oxidation of a Cobalt Chromium Alloy: An X-Ray Photoemission Spectroscopy Study. *J. Vac. Sci. Technol. A* **1988**, *6* (3), 928.

(22) Hagelin-Weaver, H. A. E.; Hoflund, G. B.; Minahan, D. M.; Salaita, G. N. Electron Energy Loss Spectroscopic Investigation of Co Metal, CoO, and Co3O4 before and after Ar+ Bombardment. *Appl. Surf. Sci.* **2004**, *235* (4), 420–448.

(23) Tan, Y. L.; Gao, Q. M.; Yang, C. X.; Yang, K.; Tian, W. Q.; Zhu, L. H. One-Dimensional Porous Nanofibers of Co3O4 on the Carbon Matrix from Human Hair with Superior Lithium Ion Storage Performance. *Sci Rep* **2015**, *5* (February), 15–17.

(24) Jiang, J.; Li, L. Synthesis of Sphere-like Co3O4 Nanocrystals via a Simple Polyol Route. *Mater. Lett.* **2007**, *61* (27), 4894–4896.

(25) Jakubek, T.; Kaspera, W.; Legutko, P.; Stelmachowski, P.; Kotarba, A. Surface versus Bulk Alkali Promotion of Cobalt-Oxide Catalyst in Soot Oxidation. *Catal. Commun.* **2015**, *71* (August), 37–41.

(26) Sousa, P. M.; Silvestre, A. J.; Popovici, N.; Conde, O. Morphological and Structural Characterization of CrO 2 / Cr 2 O 3 Films Grown by Laser-CVD. **2005**, *247*, 423–428.

(27) Shim, S.-H.; Duffy, T. S.; Jeanloz, R.; Yoo, C.-S.; Iota, V. Raman Spectroscopy and X-Ray Diffraction of Phase Transitions in Cr2O3 to 61 GPa. *Phys. Rev. B* **2004**, *69* (14), 144107.

(28) Lasagni, a.; Mücklich, F. FEM Simulation of Periodical Local Heating Caused by Laser Interference Metallurgy. *J. Mater. Process. Technol.* **2009**, *209* (1), 202–209.

(29) Kern, T.; Yang, Y.; Glover, R.; Ong, J. L. Effect of Heat-Treated Titanium Surfaces on Protein Adsorption and Osteoblast Precursor Cell Initial Attachment. *Implant Dent.* **2005**, *14* (1), 70–76.

(30) Raimbault, O.; Benayoun, S.; Anselme, K.; Mauclair, C.; Bourgade, T.; Kietzig, A. M.; Girard-Lauriault, P. L.; Valette, S.; Donnet, C. The Effects of Femtosecond

Laser-Textured Ti-6Al-4V on Wettability and Cell Response. *Mater. Sci. Eng. C* **2016**, *69*, 311–320.

(31) Pegueroles, M.; Aparicio, C.; Bosio, M.; Engel, E.; Gil, F. J.; Planell, J. A.; Altankov, G. Spatial Organization of Osteoblast Fibronectin Matrix on Titanium Surfaces: Effects of Roughness, Chemical Heterogeneity and Surface Energy. *Acta Biomater.* **2010**, *6* (1), 291–301.

(32) Milleret, V.; Hefti, T.; Hall, H.; Vogel, V.; Eberli, D. Influence of the Fiber Diameter and Surface Roughness of Electrospun Vascular Grafts on Blood Activation. *Acta Biomater.* **2012**, *8* (12), 4349–4356.

(33) Hecker, J. F.; Edwards, R. O. Effects of Roughness on the Thrombogenicity of a Plastic. *J. Biomed. Mater. Res.* **1981**, *15* (1), 1–7.

(34) Milleret, V.; Ziogas, A.; Buzzi, S.; Heuberger, R.; Zucker, A.; Ehrbar, M. Effect of Oxide Layer Modification of CoCr Stent Alloys on Blood Activation and Endothelial Behavior. *J. Biomed. Mater. Res. - Part B Appl. Biomater.* **2015**, *103* (3), 629–640.

(35) Huang, N.; Chen, Y. R.; Luo, J. M.; Yi, J.; Lu, R.; Xiao, J.; Xue, Z. N.; Liu, X. H. In Vitro Investigation of Blood Compatibility of Ti with Oxide Layers of Rutile Structure. *J Biomater Appl* **1994**, *8* (4), 404–412.

(36) Milleret, V.; Buzzi, S.; Gehrig, P.; Ziogas, A.; Grossmann, J.; Schilcher, K.; Zinkernagel, A. S.; Zucker, A.; Ehrbar, M. Protein Adsorption Steers Blood Contact Activation on Engineered Cobalt Chromium Alloy Oxide Layers. *Acta Biomater.* **2015**, *24*, 343–351.

(37) Nan, H.; Ping, Y.; Xuan, C.; Yongxang, L.; Xiaolan, Z.; Guangjun, C.; Zihong, Z.; Feng, Z.; Yuanru, C.; Xianghuai, L.; Tingfei, X. Blood Compatibility of Amorphous Titanium Oxide Films Synthesized by Ion Beam Enhanced Deposition. **1998**, *19*, 771–776.

(38) Maitz, M. F.; Tsyganov, I.; Pham, M.-T.; Wieser, E. Blood Compatibility of Titanium Oxides with Various Crystal Structure and Element Doping. *J Biomater Appl* **2003**, *17* (4), 303–320.

(39) Takemoto, S.; Yamamoto, T.; Tsuru, K.; Hayakawa, S.; Osaka, A.; Takashima, S. Platelet Adhesion on Titanium Oxide Gels: Effect of Surface Oxidation. *Biomaterials* **2004**, *25* (17), 3485–3492.

(40) Chen, L.; Liu, M.; Bai, H.; Chen, P.; Xia, F.; Han, D. Antiplatelet and Thermally

Responsive Poly (N -Isopropylacrylamide) Surface with Nanoscale. **2009**, No. 18, 10467–10472.

(41) Sun, T.; Tan, H.; Han, D.; Fu, Q.; Jiang, L. No Platelet Can Adhere-Largely Improved Blood Compatibility on Nanostructured Superhydrophobic Surfaces. *Small* **2005**, *1* (10), 959–963.

(42) Dalby, M. J.; Gadegaard, N.; Riehle, M. O.; Wilkinson, C. D. W.; Curtis, A. S. G. Investigating Filopodia Sensing Using Arrays of Defined Nano-Pits down to 35 Nm Diameter in Size. *Int. J. Biochem. Cell Biol.* **2004**, *36* (10), 2015–2025.

(43) Fujita, S.; Ohshima, M.; Iwata, H. Time-Lapse Observation of Cell Alignment on Nanogrooved Patterns. *J. R. Soc. Interface* **2009**, *6* (Suppl 3), S269-77.

(44) Song, K. H.; Kwon, K. W.; Song, S.; Suh, K.-Y.; Doh, J. Dynamics of T Cells on Endothelial Layers Aligned by Nanostructured Surfaces. *Biomaterials* **2012**, *33* (7), 2007–2015.

(45) Teichmann, J.; Morgenstern, A.; Seebach, J.; Schnittler, H.-J.; Werner, C.; Pompe, T. The Control of Endothelial Cell Adhesion and Migration by Shear Stress and Matrix-Substrate Anchorage. *Biomaterials* **2012**, *33* (7), 1959–1969.

(46) Bouta, E. M.; McCarthy, C. W.; Keim, A.; Wang, H. B.; Gilbert, R. J.; Goldman, J. Biomaterial Guides for Lymphatic Endothelial Cell Alignment and Migration. *Acta Biomater.* **2011**, *7* (3), 1104–1113.

Chapter IV: Synergistic effect of surface biofunctionalization and nanopatterning of CoCr alloy for cardiovascular applications: endothelial cell adhesion, migration and proliferation

1. Introduction

At the artery, endothelialization is mainly achieved through ECs migration from the healthy endothelium situated at both extremities of the stent. Different approaches have tried to modify the stent topography with a linear patterning in order to mimic the orientation of ECs at the coronary artery lumen [1–5]. A large number of techniques have been applied to modify the surface topography of cardiovascular implants: metallographic grinding, plasma etching, photolithographic etching, and UV lithography, among others [6–9]. However, most of the mentioned processing techniques involve multiple steps of preparation and, sometimes, including coatings steps. On the contrary, direct laser interference patterning (DLIP) requires only one single processing step and it can be applied to a wide range of materials [10]. In Chapter III, we demonstrated that 600 nm depth linear patterns obtained by DLIP on CoCr alloy surfaces induced the alignment and migration of ECs. Moreover, by modifying the chemical properties of these surfaces, DLIP technique induced a beneficial reduction of platelet adhesion.

Within this context, the aim of this chapter is to modify CoCr alloy surfaces with a combination of linear patterning obtained by DLIP and bio-functionalization with RGD and YIGSR peptides to study the synergistic effect of both treatments in ECs adhesion, migration and proliferation. Linear patterned CoCr surfaces were characterized topographically by atomic force microscopy (AFM) and electrochemical assays were applied to determine the corrosion resistance properties. RGD and YIGSR peptides were covalently immobilized by silanization and the obtained coating characterized by Fourier transform infrared spectroscopy (FTIR), X-ray photoelectron microscopy (XPS), AFM and fluorescence microscopy. Finally, the effect of surface modifications on the biological response was evaluated by ECs adhesion, migration and proliferation on the patterned and biofunctionalized surfaces.

2. Materials and methods

2.1. CoCr alloy surfaces

CoCr alloy ASTM F90 was polished and cleaned as explained in Chapter III section 2.1. to obtain smooth mirror-like surfaces (Ra < 10 nm).

2.2. DLIP technique

A Nd:YAG laser was used to modify the CoCr surfaces topography in conditions similar to Chapter III section 2.2. As a difference, the angle 2α between the two laser beams was fixe. As a result, the laser beams interfere onto the sample surface and generate a line-like interference pattern with a fixe periodicity (P) of 10 µm (**Figure IV.1**). Laser fluency was varied to generate different pattern depths (D). A 0.81 $J.cm^{-2}$ fluence was used to obtain low depth pattern (coded as **10L** with D < 100 nm) and a 2.42 $J.cm^{-2}$ fluence was used to obtain high depth pattern (coded as **10H** with D > 700 nm). **FLAT** samples referred to polished and non-patterned ones.

2.3. Functionalization of CoCr surfaces

2.3.1. Solid-phase peptide synthesis

The linear peptides RGDS and YIGSR were synthesized in solid-phase following the Fmoc/tBu strategy using Fmoc-Rink amide 4-methylbenzhydrylamine (MBHA resin) as solid support (300 mg, loading of 1.0 mmol/g), according to previously reported methods [11]. The two functional sequences were synthesized containing three 6-aminohexanoic acid (Ahx) units as spacer system and two lysines (Lys), which served as anchors (**Figure IV.1A**). Moreover, the two peptides were synthesized with an additional 5(6)-carboxyfluorescein (CF) at their N-termini for characterization with fluorescence microscopy. The peptides were purified by semi-preparative HPLC (Waters, Milford, MA, USA) (XBridge C18 column, 19 x 150 mm, 5 µm) and characterized by analytical HPLC (Waters) (XBridge C18 column, 4.6 x 100 mm, 3.5 µm) and MALDI-TOF Voyager DE RP spectrometer (Applied Biosystems, Foster City, CA, USA). The characterization of the purified peptides is shown in **Table IV.1**. All chemicals required for the synthesis, including resins, Fmoc-L-amino acids and coupling reagents, were obtained from Iris Biotech GmbH (Germany) and Sigma-Aldrich (USA).

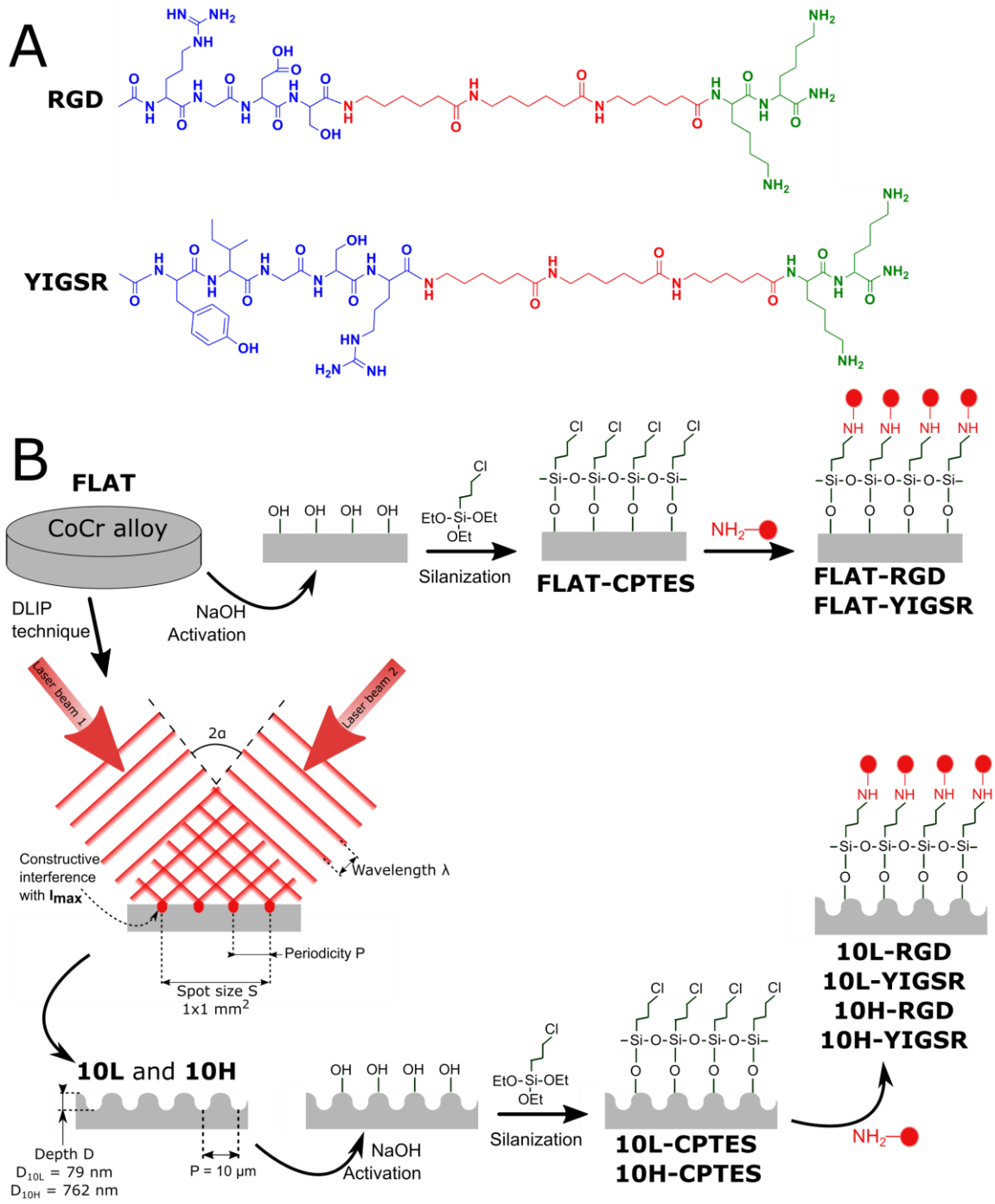

Figure IV.1: *(A) Chemical structure of RGD and YIGSR peptides. Green: anchoring sequence (Lys-Lys); Red: spacer units (Ahx-Ahx-Ahx); Blue: functional sequences (Arg-Gly-Asp-Ser and Tyr-Ile-Gly-Ser-Arg) (B) Scheme of the DLIP and biofunctionalization steps to obtain the different patterned and/or biofunctionalized CoCr surfaces (FLAT: polished CoCr; 10L: low depth linear patterned CoCr surfaces; 10H: high depth linear patterned CoCr surfaces; FLAT-CPTES, 10L-CPTES and 10H-CPTES: FLAT, 10L and 10H followed by CPTES silanization; FLAT-RGD, 10L-RGD and 10H-RGD: FLAT, 10L and 10H followed by CPTES silanization and biofunctionalization with RGD; FLAT-YIGSR, 10L-YIGSR and 10H-YIGSR: FLAT, 10L and 10H followed by CPTES silanization and biofunctionalization with YIGSR).*

Table IV.1: *RGD, RGD-CF, YIGSR and YIGSR-CF peptides sequences, retention time (t_R), purity and molecular masse (m/z) obtained by analytical HPLC and MALDI-TOF.*

Code	Sequence	t_R (min)[a]	Purity (%)[a]	Calculated m/z	Experimental m/z[d] $[M+H]^+$
RGD	Lys-Lys-(Ahx)3-Ser-Asp-Gly-Arg-OH	2.955[b]	93	1069.66	1069.68
RGD CF	Lys-Lys-(Ahx)3-Ser-Asp-Gly-Arg-CF	4.345[b]	98	1385.70	1385.66
YIGSR	Lys-Lys-(Ahx)3-Arg-Ser-Gly-Ile-Tyr-OH	5.228[c]	98	1230.78	1230.75
YIGSR CF	Lys-Lys-(Ahx)3-Arg-Ser-Gly-Ile-Tyr-CF	5.503[c]	99	1546.82	1546.80

[a)] Retention time (t_R) and purity were calculated by analytical HPLC using a reversed-phase XBridge BEH130 C-18 column (4.6 mm x 100 mm, 3.5 µm) (Waters, Milford, MA, USA) and a photodiode array detector (Waters 2998). [b)] Linear gradient: 0 to 60 % MeCN over 8 min; flow: 1.0 mL/min. [c)] Linear gradient: 5 to 100 % MeCN over 8 min; flow: 1.0 mL/min. [d)] Mass spectra were recorded on a MALDI-TOF Voyager DE RP spectrometer (Applied Biosystems, Foster City, CA,USA).

2.3.2. Protocol of immobilization

The peptides were covalently immobilized on the CoCr surfaces through a three-step strategy consisting of activation, silanization and peptide immobilization (**Figure IV.1B**).

First, surfaces were activated with 5 M NaOH solution during 2 h at room temperature (RT) under ultrasonication to generate hydroxyl groups. Treated samples were then cleaned twice in distilled water under ultrasonication for 30 min. Afterwards, activated samples were silanized in 10 ml solution of 0.5 M 3-chloropropyltriethoxysilane (CPTES) (Sigma-Aldrich) and 0.05 M N,N-diisopropylethylamine (DIEA) in anhydrous toluene at 90 °C for 1 h under nitrogen atmosphere and vigorous stirring. Silanized samples were ultrasonically rinsed in cyclohexane, isopropanol, Milli-Q distilled water and acetone for 15 min each, and finally dried with nitrogen. Silanized samples were coded as **FLAT-CPTES**, **10L-CPTES** and **10H-CPTES**. Finally, silanized samples were immersed overnight in 100 µM peptide solutions (samples coded as **FLAT-RGD**, **10L-RGD**, **10H-RGD, FLAT-YIGSR, 10L-YIGSR** and **10H-YIGSR**) in phosphate-buffered saline (PBS) with a pH 10.0 at RT and washed three times with distilled water.

2.4. Physico-chemical characterization of the patterned surfaces

Surface morphology and roughness of CoCr samples were analyzed by atomic force microscopy (AFM) (Dimension 3100, Veeco Digital Instruments, Bruker,

Germany). Topographic, error signal mode, and phases images were recorded simultaneously in tapping-mode in air using a silicon Tap150al-G cantilever (NanoWorld Group, Neuchâtel, Switzerland) at a scan rate of 1 Hz. Five areas of 50x50 μm^2 were analyzed for FLAT, 10L and 10H CoCr surfaces. Obtained images were studied by WSxM software [12]. The topographical profile as well as the root mean square roughness (R_q) were obtained from topographic images: $R_{q\text{-micro}}$ from areas of 50x50 μm^2 and $R_{q\text{-nano}}$ from areas of 1x1 μm^2.

To evaluate the effect of surface modification with the DLIP technique on the corrosion of CoCr alloy surfaces, electrochemical characterization was performed with a potentiostat PARSTAT 2273 (Princeton Applied Research, USA) with a Faraday cage. Measurements were controlled with the software PowerSuite Electrochemical (Princeton Applied Research). A saturated calomel electrode (SCE, Koslow Scientific Company, USA) was used as reference electrode and a Hank's balanced salt solution (Sigma-Aldrich) was used as electrolyte solution. Open circuit potential assays were done following the standard ISO 10993-15 [13] in order to determine the corrosion potential of patterned CoCr surfaces. Degradation products of FLAT and patterned CoCr samples were evaluated after immersion in the Hank's balanced salt solution at 37 ºC during seven days. Released ions to the medium were measured by mass spectroscopy ICP-MS (Agilent 7500CE, USA) as indicated by the standard ISO 10993-15.

A streaming potential instrument (Surpass Electrokinetic Analyzer, Anton Paar, Austria) with an adjustable gap cell was used to obtain the zeta-potential of FLAT, 10L and 10H surfaces. Measurements were performed with a 1 mM KCl solution as electrolyte and the pressure ramp run up to a maximum pressure of 400 mbar. The initial electrolyte solution was adjusted to pH 9.0 using 0.1 M KOH solution and titrated by adding 0.1 M HCl down to pH 3.0. The isoelectric point (IEP) and the surface charge at pH 7.4 were obtained using the VisioLab software (Anton Paar).

2.5. Physico-chemical characterization of the biofunctionalized surfaces

Silanized and biofunctionalized CoCr surfaces were chemically characterized with attenuated total reflectance Fourier transform infrared (ATR-FTIR) spectroscopy using a Nicolet 6700 FTIR spectrometer (Thermo Fisher Scientific, USA) combined with the ATR Smart Saga furnished with a diamond crystal.

Sampling area was set to a 1 mm diameter circle, scan resolution was 0.482 cm^{-1} and each sample analysis was the result of the average of 512 scans. All samples spectra were analysed with OMNIC 8 software (Thermo Fisher Scientific).

To characterize the silane and peptides layers, FLAT and biofunctionalized CoCr surfaces were analyzed by AFM. AFM conditions were similar to the previously described at Chapter IV section 2.4. Only the scanning velocity and area were changed to 0.5 Hz and 2x2 μm^2, respectively. Topographical profile and roughness $R_{q\text{-}nano}$ were obtained from height images. Phase images were used to extract the phases distribution and calculate the percentage of area covered by non-metallic substances.

X-ray photoelectron spectroscopy (XPS) was used to analyse chemical composition of CoCr surfaces before and after functionalization. Measurements were performed with a SPECS Surface Nano Analysis GmbH (Berlin, Germany) equipped with a Mg anode X50 source operating at 150 W and a Phoibos 150 MCD-9 detector. The elements present on the surface were evaluated by low-resolution survey spectra, whereas high-resolution of some elements (C 1s, O 1s, Cr 2p, Co 2p, N 1s and Cl 2p) were measured with a pass energy of 25 eV at 0.1 eV steps at a pressure below 7.5×10^{-9} mbar. All binding energies were referred to the C1s signal at 284.8 eV. Casa XPS software (Version 2.3.16, Casa Software Ltd., Teignmouth, UK) was used to do fitting and peak integration of spectra.

The stability of the peptide layer toward sterilization and ultrasonication treatments was analysed by fluorescence. To this end, samples were functionalized with fluorescent peptides RGD-CF and YIGSR-CF, and subsequently subjected to either sterilization by gamma radiation (AragoGamma, Spain) using a 25 kGy dose (samples **FLAT-RGD-RG** and **FLAT-YIGSR-RG**) or ultrasonication during 1h in PBS (samples **FLAT-RGD-US** and **FLAT-YIGSR-US**). Then, the fluorescent immobilized peptides before and after stability treatments were extracted with 500 µl of 0.2 M NaOH during 2 h at RT [14]. The fluorescence of the extracted solution was measured with a spectrofluorophotometer (Infinite M200 PRO NanoQuant Microplate reader, Tecan, Switzerland) at 492 nm excitation and 517 nm emission wavelengths. The quantity of attached peptides was determined by comparison with a standard

curve, which was prepared under identical conditions with peptides concentration ranging from 0 up to 1000 ng·ml^{-1}.

2.6. Biological characterization

2.6.1. Endothelial cells

Cellular experiments were conducted using HUVECs in the exact same conditions as in Chapter III (section 2.1.). All cellular studies were done using triplicates and repeated at least in two independent assays to ensure reproducibility.

2.6.2. Cell adhesion

Previous to cell adhesion assay, CoCr samples were sterilised in ethanol 70% for 20 min at RT. Next, samples were placed in 48-well plates and 30,000 cells/disk were seeded and allowed to attach in serum free medium. Samples were incubated overnight at 37 °C and rinsed thrice with PBS to remove non-adherent cells. To characterize the number and spreading of adhered HUVECs, nuclei and actin fibers were stained by immunofluorescence following the protocol explained in Chapter III section 2.4.2. Cell number and morphology parameters were studied by FIJI software [15] obtaining the cell number, cell mean area, and percentage of aligned cells for each surface. Cells were considered aligned if the angle between the long axis and the pattern was < 30°. Once analysed, CoCr samples were ultrasonically cleaned in PBS and adhered cells were fixed with glutaraldehyde (G400-4, Sigma-Aldrich) and dehydrated through immersion in different solutions of ethanol in order to observe in more detail the cells shape by field emission scanning electron microscopy (FE-SEM) with a Zeiss Neon40 FE-SEM microscope (Carl Zeiss NTS GmbH, Germany). For each sample, five images were taken at a working distance of 6 mm and a potential of 5 kV.

2.6.3. Wound healing migration study

To evaluate the process of wound healing and cell migration onto patterned and functionalized CoCr surfaces, HUVECs were stained with the cell membrane fluorescent linker PKH67 (PKH67-GL, Sigma-Aldrich) 24 h prior to wound healing assays. Before cell culture, CoCr samples were sterilized in ethanol 70% for 20 min at RT. The wound healing processes were reproduced by placing an Ibidi culture-insert (Ibidi, Germany) on top of each sample. On the patterned surfaces

the Ibidi insert was placed keeping the gap perpendicular to the patterns lines. Thus, a suspension of 20,000 labeled cells were placed at both chambers of the insert with complete medium, and incubated for 24 h until reaching a confluent HUVEC adhesion. After, the insert was removed creating a cell-free gap of 500 ± 50 µm. The surfaces were cleaned twice with PBS to remove non-adhered cells and then, filled with serum free medium. HUVEC cell migration was recorded using a fluorescence stereomicroscope (Leica MZ16F, Leica microsystems, Germany) combined with the camera DFC 300 FX (Leica Microsystems). Gap images were acquired for all the samples at 0 h and 24 h. The non-covered area for each CoCr disk was calculated with FIJI software and the percentage of recovery was calculated for each series.

2.6.4. Cells proliferation

To study the proliferation of cells on the substrates, 10,000 HUVECs/well were plated on samples in serum-free medium and incubated as previously described for cell adhesion assays. 4 h post seeding, medium was aspired and replaced with complete medium. After 2, 5, and 8 days of incubation, cell number was evaluated with the Alamar Blue assay (Invitrogen Life Technologies, Merelbeke, Belgium). Briefly, Alamar Blue-containing medium (10% (v/v)) was added for 2 h, and fluorescence of the dye was quantified according to the manufacturer instructions with a multimode microplate reader (Infinite M200 PRO, Tecan GroupLtd., Männedorf, Switzerland).

2.7. Statistical analysis

Statistical significance between means was analyzed by ANOVA test followed by post-hoc pair-wise comparison using Tukey's test at $p \leq 0.05$ (Minitab 16.2.2 Statistical Software, Minitab Inc.). All experiments data presented in this study are given as mean value ± standard deviations.

3. Results and discussion

3.1. Fabrication of linear patterned CoCr and surface characterization

CoCr surfaces were topographically modified by DLIP technique. Linear patterns with a periodicity of 10 µm were obtained. Its size was slightly smaller than ECs nucleus, in order to induce ECs elongation and migration following the pattern

direction. **Figure IV.2** and **Table IV.2** summarize the measured topographical parameters directly measured by AFM.

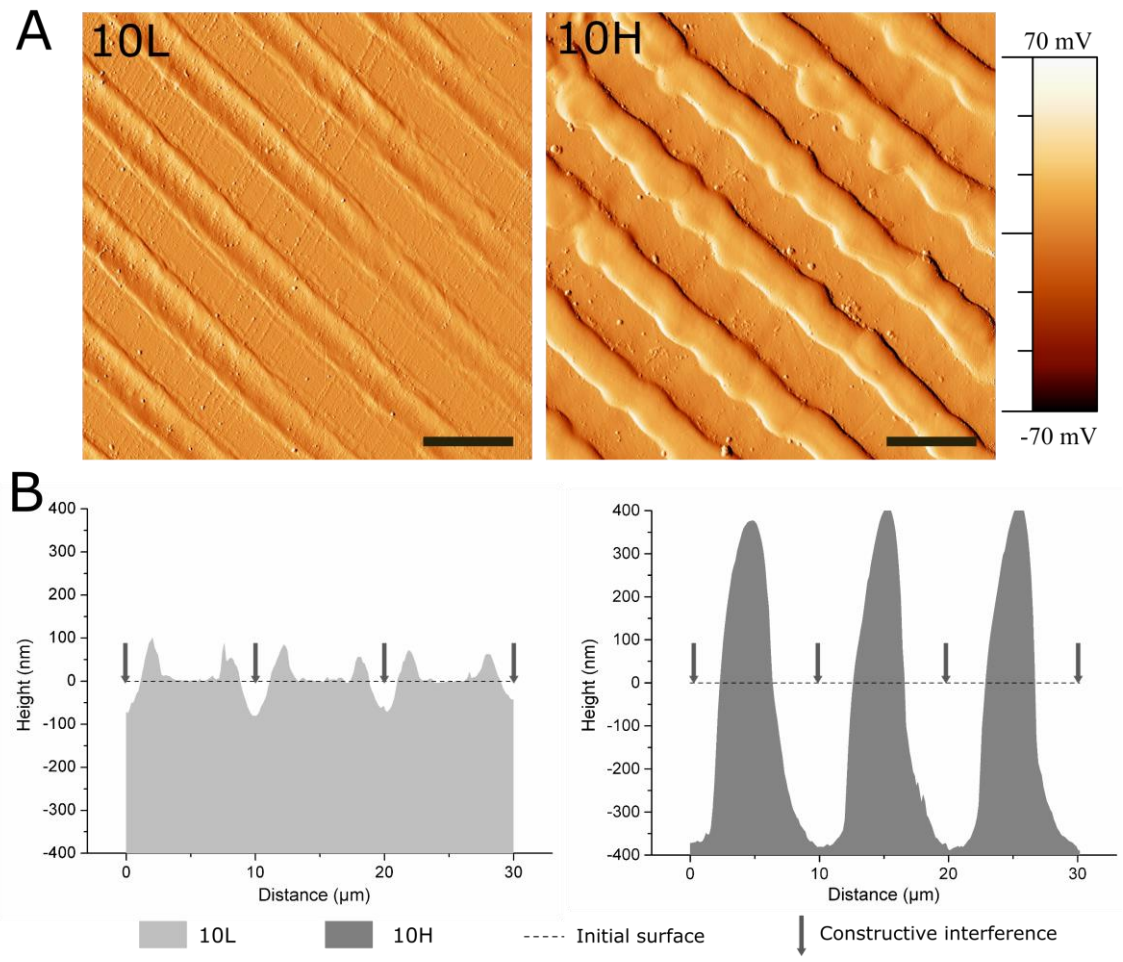

Figure IV.2: *AFM analysis of 10L and 10H surfaces to characterize the patterns topographical properties. (A) AFM error signal mode images of 10L and 10H surfaces. Scale bar = 10 µm. (B) AFM topographical profiles of 10L and 10H surfaces in the direction perpendicular to the patterns lines. Dot line indicate the estimated initial surface.*

Table IV.2: *Topographical parameters of the FLAT, 10L and 10H surfaces. $R_{q\text{-}micro}$ is the root mean square roughness measured on a 50x50 µm² area. $R_{q\text{-}nano}$ is the root mean square roughness measured on a 1x1 µm² area.*

	Periodicity P	Depth D	$R_{q\text{-}micro}$		$R_{q\text{-}nano}$
	µm	nm	nm		nm
FLAT	-	-	7 ± 1	-	0.66 ± 0.23
10L	10.0 ± 0.1	79 ± 12	33 ± 4	Valley	0.54 ± 0.17
				Peak	0.78 ± 0.31
10H	10.0 ± 0.1	762 ± 83	304 ± 25	Valley	0.79 ± 0.22
				Peak	0.79 ± 0.17

By modifying the laser fluence, two different structures were obtained, low depth patterned 10L (D ≈ 79 nm) and high depth patterned 10H (D ≈ 762 nm) surfaces. As expected, the topographical modifications increased the micro-roughness, $R_{q\text{-micro}}$, of non-modified surfaces (FLAT) from 7.4 ± 1.3 nm up to 33.2 ± 3.7 nm for 10L surfaces and 303.6 ± 24.9 nm for 10H series. However, nano-roughness of FLAT samples and patterned surfaces, either at peaks or valleys, showed no statistical differences. AFM error signal mode images (**Figure IV.2A**) for the two different patterned surfaces confirmed that 10H surfaces presented homogenous grooves with clearly identifiable peaks and valleys; in contrast, on 10L surfaces the low depths hindered the identification of peaks compared to valleys. **Figure IV.2B** presents the cross-section profiles of 10L and 10H surfaces directly extracted from the AFM topographic images, which allowed characterizing the shape of the peaks. Indeed, 10H is characterized by a sinusoidal shape with valleys, where constructive interference occurs, and peaks, where destructive interference takes place and thus, two melted material fronts joint. On the contrary, 10L surfaces is composed of a low depth valley where the constructive interferences met creating two small peaks at both sides and a non-modified flat area where the beams interacted destructively. These two different configurations, called respectively single and double-peak pattern surfaces, are usual for metallic surfaces modified by DLIP, as described in Chapter III and in previous studies [1,16]. Such differences can be explained by the applied laser fluencies: high fluencies, used for 10H series, provided enough energy to melt a considerable amount of metal that flowed outside the constructive interference spots towards the destructive interference spots, due to the surface tension gradient resulting from the temperature gradient [16–18]. At the destructive interference spots the advancing melt fronts join, creating the characteristic peaks. In the case of 10L series, the applied low fluence melted a lower quantity of CoCr alloy and the two fronts could not joint together, generating two small peaks surrounding the spots where the beams interfered constructively. In both surfaces, 10L and 10H, the high temperatures applied during DLIP transformed the crystalline oxide layer into a thicker amorphous oxide layer overall the surface, as demonstrated in the Chapter III. Thus, considering the low roughness of 10L surfaces, 10L series could be considered mainly as surfaces with chemical changes, and a negligible topographical pattern.

CoCr alloy ASTM F-90 is extensively used as stent material mainly due to its capacity of forming a naturally passive oxide layer that confers very good corrosion resistance properties to the material. As surface patterning by DLIP could generate changes in the corrosion behaviour of the materials, electrochemical assays and ion release tests were performed (**Table IV.3**). All studied series presented statistically equal corrosion potentials of approximately 1000 mV, suggesting that DLIP did not modify the corrosion resistance of the CoCr surfaces. Moreover, no corrosion pits were observed on the tested surfaces (not shown), validating DLIP as a treatment that do not-modify the corrosion resistance observed in FLAT surfaces. Ion release assays were performed in Hank's balanced salt solution at 37ºC during 7 days. The release of Ni ions, susceptible to allergy, was not significantly higher on 10L and 10H surfaces, compared to FLAT surface. The release of Co and Cr ions, on 10L surfaces was slightly lower than on FLAT, indicating that 10L series are not toxic just as the CoCr alloys used in the current stents. On the other hand, the release of ions significantly increased on 10H series (Cr: 4.3 ± 0.3 ng; Co: 77.8 ± 8.6 ng) compared to FLAT (Cr: 1.6 ± 0.3 ng; Co: 47.5 ± 16.0 ng). However, such higher release should not be detrimental for the biological performance of these materials. Firstly, the high toxicity and carcinogenic properties of Cr are associated to its hexavalent form (chromium VI) [19], and we have shown in Chapter III that DLIP generated only Cr (III) at the CoCr alloy oxide layer. Secondly, it should be taken into consideration that stents are placed in the artery and release metallic ions under blood flow conditions. Thus, if we consider 5 liters as the normal blood quantity for an adult and the stent surface area being half of the area of the studied samples, the release of Cr and Co from 10H surfaces would be equivalent to $4.3x10^{-4}$ ng/ml and $7.8x10^{-3}$ ng/ml, respectively. These values are 100,000 and 15,000 times lower, for Cr and Co, respectively, than the maximum concentrations recommended by the World Health Organization (Cr: 50 ng/ml; Co: 150 ng/ml) [20,21]. Consequently, even if the released ions were increased on 10H series compared to FLAT, the release of metallic ions after DLIP patterning is kept at non-toxic levels.

Table IV.3: *Detailed results of corrosion resistance, ion release and zeta potential on CoCr surfaces before and after DLIP patterning. Corrosion potential and ion release were obtained according to the standard ISO 10993-15. Isoelectric point (IEP) and zeta potential (ζ) at pH 7.4 were measured.*

		Ion release			Zeta potential	
	Corrosion potential	Co ions	Cr ions	Ni ions	IEP	ζ at pH 7.4
	mV	ng	ng	ng	pH	mV
FLAT	1014.3 ± 10.1	47.5 ± 16.0	1.6 ± 0.3	12.4 ± 3.8	4.9 ± 0.0	- 34.5 ± 2.9
10L	1017.6 ± 9.5	23.3 ± 6.3	1.5 ± 0.2	9.4 ± 2.8	4.8 ± 0.0	- 39.7 ± 0.2
10H	1031.7 ± 6.1	77.8 ± 8.6	4.3 ± 0.3	17.5 ± 1.0	4.5 ± 0.0	- 11.5 ± 1.0

The zeta potential studies indicated that the IEP of the FLAT and the patterned surfaces is around pH ~ 4.7. As the solution was more alkaline, the surfaces showed a steadily more negative zeta potential. The ζ at pH 7.4 is very similar on FLAT and 10L surfaces mainly because the roughness of 10L surfaces is negligible. For 10H surfaces it was found a less negative surfaces charge compared to FLAT due to the effect of the linear pattern. The effect of peaks and valleys onto zeta potential measurements have been already described [22]. The fact that linear pattern retains charges inside the valleys prevents their detection at the end of the channel and possibly generates an opposite flow, leading to a decrease in measured zeta potential.

3.2. Biofunctionalization of CoCr and surface characterization

The studied peptides were synthesized with the structure and the characteristics presented in **Figure IV.1** and **Table IV.1**. As previously mentioned, both peptides are composed of three distinct parts. First, the bioactive sequences, RGD and YIGSR (in blue in Figure IV.1), which determine the biological functionality of the biomolecule. The RGD sequence was chosen for its well-known effect on cell adhesion [23–26] and YIGSR was selected for its ability to bind specifically to ECs [27–31]. Secondly, the spacer units, three aminohexanoic acid (Ahx) (in red), which ensure the appropriate accessibility of the functional sequences to interact with cells. Indeed, in previous studies, it has been demonstrated that peptides with spacer molecules shorter in length failed to influence the biological activity on the coated surfaces [31,32]. And finally, two lysines (in green) which contain primary

amines in their side chains as anchoring groups, to covalently attach the peptides to the silanized surface.

The effectiveness of silanization and functionalization of CoCr surfaces was evaluated by ATR-FTIR (**Figure IV.3**), AFM (**Figure IV.4**) and XPS (**Figure IV.5**). ATR-FTIR spectra of FLAT-CPTES, FLAT-RGD and FLAT-YIGSR surfaces are presented in **Figure IV.3**.

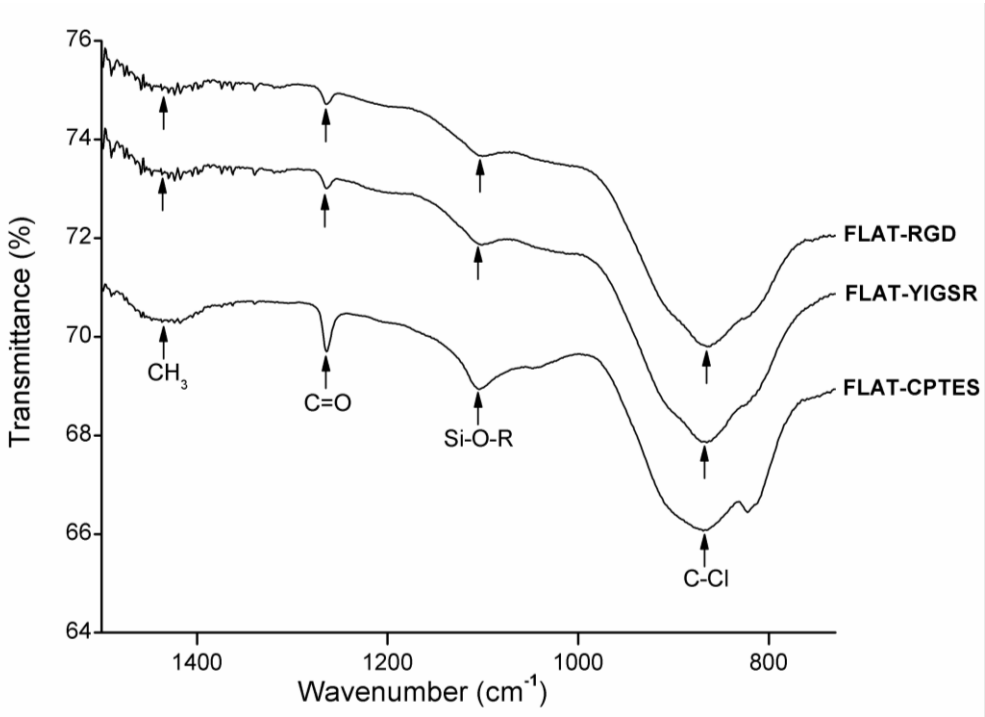

Figure IV.3: *ATR-FTIR of FLAT-CPTES, FLAT-RGD and FLAT-YIGSR surfaces from 700 to 1600 cm^{-1}. Arrows indicate significant peaks.*

On all the surfaces, the peak observed at 1267 cm^{-1}, which corresponds to C = O bonding, was the result of atmospheric contamination. On CPTES samples, Si-O-R peaks, at 1100 cm^{-1}, were related to the covalent bonding of the silane on the surface [33,34]. Also, the terminal chlorine group from the CPTES silanes was detected at a wavelength of 870 cm^{-1}. Finally, as CoCr alloys did not contain CH_3 group, the CH_3 peak, at 1430 cm^{-1}, confirmed the presence of CPTES on FLAT-CPTES surfaces. The spectra of RGD and YIGSR-coated surfaces displayed exactly the same peaks detected on CPTES samples. In particular, no N bonding peaks were detected, as it would be expected in the presence of peptides. This observation could be due to the low sensitivity of the surface technique, which would be not adequate to detect a low amount of biomolecule.

AFM characterization was done to analyze the layer of silane and peptides immobilized onto CoCr surfaces (**Figure IV.4**). As expected, FLAT surface showed a smooth surface with some scratches from polishing, while CPTES series presented small clusters of 6 nm height approximately (**Figure IV.4A**). Similar differences were observed by T. Sargeant *et al.* [35] after silanization on NiTi alloy surfaces. Moreover, FLAT-RGD, FLAT-YIGSR, 10L-CPTES and 10H-CPTES surfaces presented roughness values very similar to those measured in the CPTES samples (**Figure IV.4C**). Indeed, all these five conditions had $R_{q\text{-}nano}$ values of about 2.5 nm with no statistical differences; whereas FLAT samples presented values 4 times lower ($R_{q\text{-}nano}$ = 0.66 ± 0.23 nm). The increment of the $R_{q\text{-}nano}$ roughness for silanized and functionalized surfaces, compared to FLAT, can be thus attributed to the coating layer. Since no statistical differences were found between silanized and functionalized surfaces, we can assume that the peptide layer is very thin and not observable with AFM. Also, the similar roughness observed on FLAT and patterned silanized surfaces suggested that the efficiency of silanization is not affected by the DLIP process.

Figure IV.4B exhibits the phase map for the region of interest. It is found a single phase for FLAT surfaces while CPTES series showed a bimodal phases distribution at -33º and 8º. AFM phase imaging in tapping mode is directly related to the viscoelastic properties of the analysed surface and, consequently, to the surface hardness of the material. Thus, CPTES surfaces seemed to have different materials properties, presumably related to the immobilization of silanes onto CoCr surface. Also, the percentage of covered area by the coating was calculated (**Figure IV.4D**). All functionalized surfaces presented an 85 % of surface coverage and no statistical differences were observed between silanized and functionalized surfaces onto both polished and patterned CoCr surfaces.

The increased roughness and the presence of two different phases on FLAT-CPTES compared to FLAT confirmed the attachment of CPTES silane on the surface. Since the same results were observed on 10L-CPTES and 10H-CPTES, we can conclude that the silanization process occurred with the same efficiency on FLAT and patterned surfaces. However, as FLAT-RGD and FLAT-YIGSR presented similar roughness and surface coverage than CPTES surfaces, we could not ascertain whether the peptides were present or not.

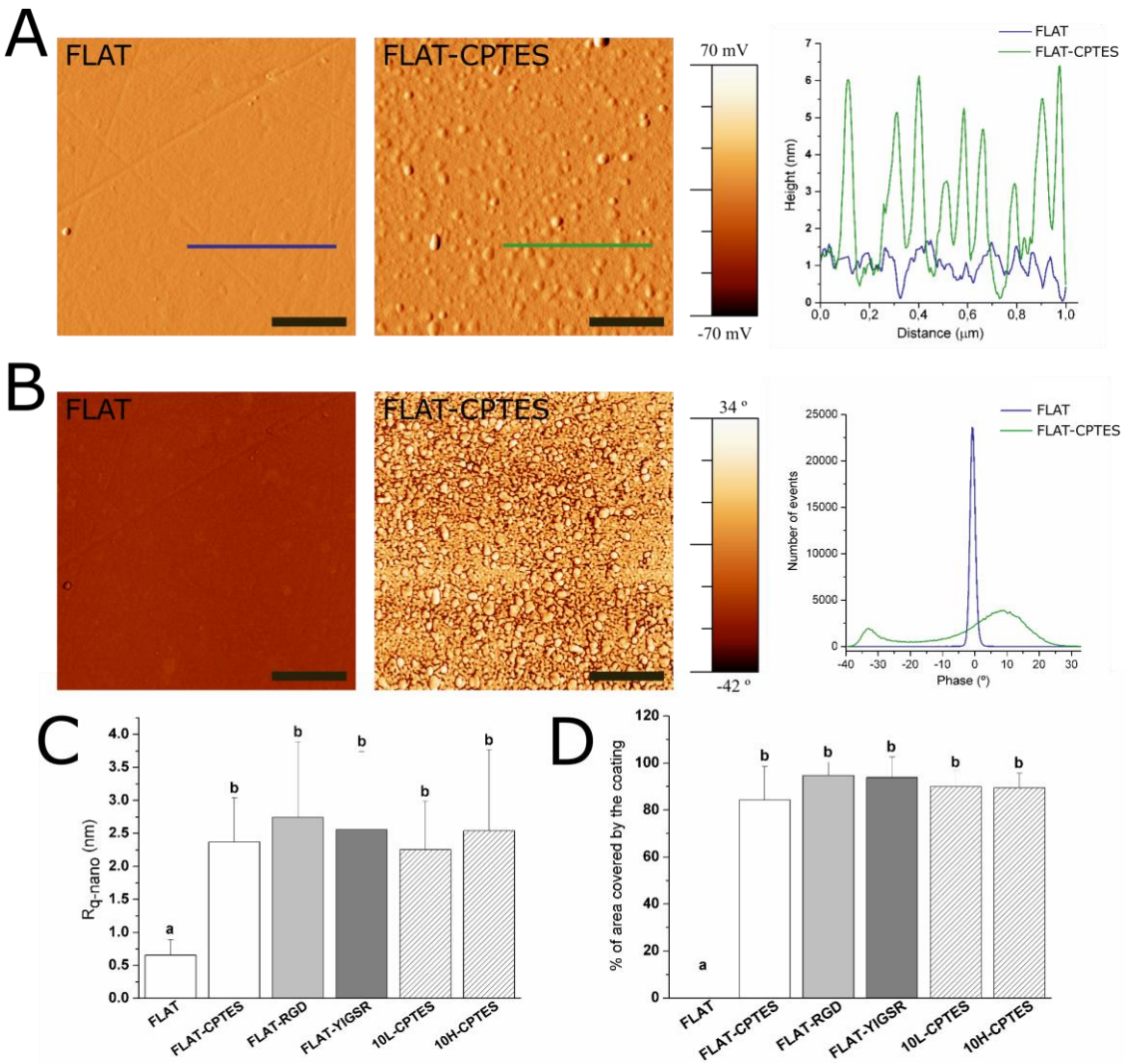

Figure IV.4: *AFM analysis of FLAT, FLAT-CPTES, FLAT-RGD, FLAT-YIGSR, 10L-CPTES and 10H-CPTES surfaces to characterize the silane and peptides layers. Scale bar = 500 nm. Columns marked with different letters belong to statistically different groups (p-value < 0.05). (A) AFM error signal mode images and topographical profiles of FLAT and CPTES surfaces. (B) Tapping-mode AFM phase images and phases distributions of FLAT and CPTES surfaces. (C) Roughness $R_{q\text{-}nano}$ calculated from AFM height images. (D) % of area covered by the coating calculated from AFM phase images.*

To evaluate the presence of immobilized peptides onto functionalized surfaces, FLAT, FLAT-RGD and FLAT-YIGSR surfaces were characterized by XPS (**Figure IV.5**). Untreated CoCr alloys displayed characteristic peaks of C 1s, O 1s, Co 2p and Cr 2p. The presence of carbon is attributed to atmospheric organic contaminants [36]. A small amount of nitrogen (N 1s) and silicon (Si 2p) contaminations was also detected. On FLAT-RGD and FLAT-YIGSR surfaces the percentage of Si 2p was increased due to the presence of CPTES.

A significant increase in N 1s was also detected for functionalized surfaces compared to FLAT (FLAT: 0.66 ± 0.05 %; FLAT-RGD: 1.56 ± 0.28 %; FLAT-YIGSR: 1.53 ± 0.03 %). This presence of nitrogen was attributed to the amide groups and other amino functionalities characteristic of the peptide sequences [37], thereby confirming the attachment of the RGD and YIGSR peptides onto the surfaces. However, the fact that Cl 2p was detected as well after the functionalization indicates that not all the electrophilic points of CPTES (i.e. $–CH_2$-Cl) reacted with the peptides. This observation suggests a limited coverage of the silane layer by the peptides, in agreement with the low % of N 1s quantified and FTIR data. Finally, it is worth to mention that no statistical differences were observed in N 1s, Si 2p and Cl 2p signals between FLAT-RGD and FLAT-YIGSR surfaces, suggesting that the functionalization occurred with the same effectiveness and the amount of immobilized peptides was very similar.

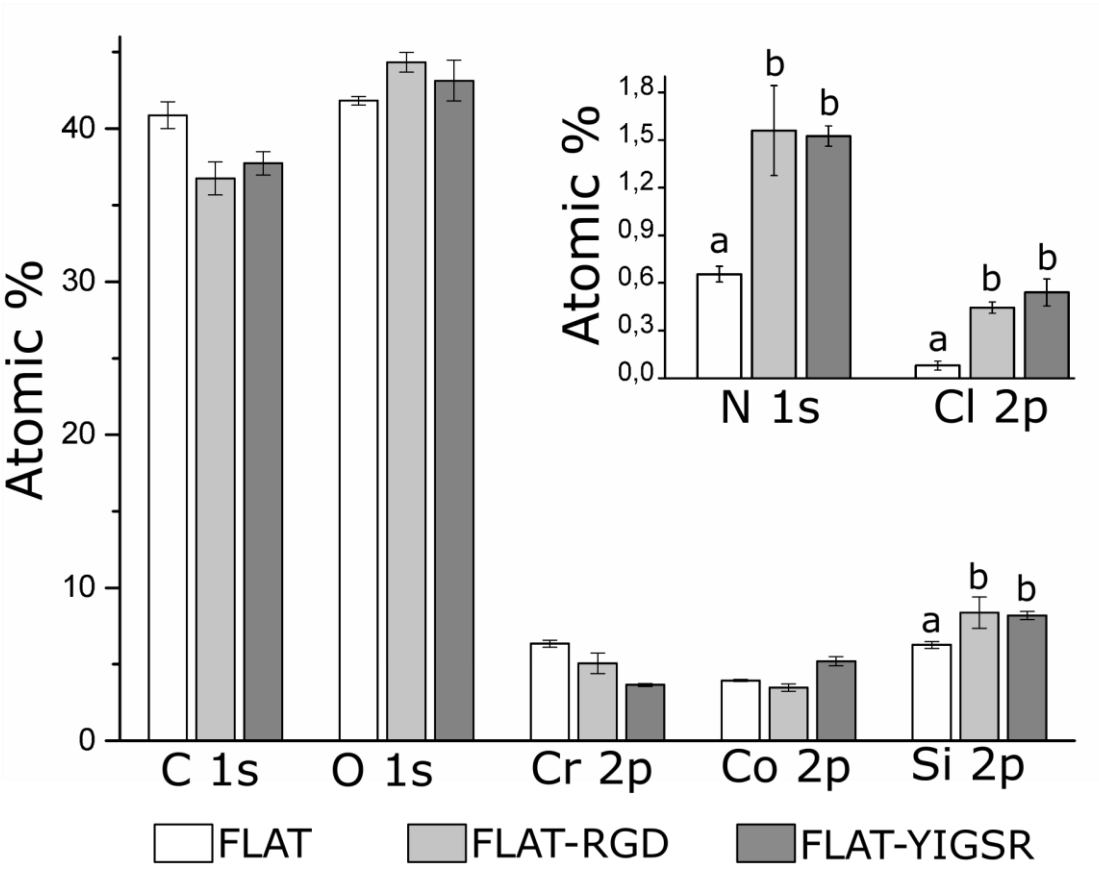

Figure IV.5: *Analysis of the chemical composition (atomic %) of FLAT, FLAT-RGD and FLAT-YIGSR surfaces by XPS. For Si 2p, N 1s and Cl 2p, bars designated with different letters belong to statistically different groups (p-value < 0.05).*

To evaluate the stability of the covalent immobilization of the different peptides FLAT-RGD and FLAT-YIGSR surfaces were subjected to either gamma radiation sterilization or ultrasound sonication with MilliQ water (**Figure IV.6**). The amount of immobilized fluorescent peptide onto FLAT-RGD and FLAT-YIGSR was calculated before the stability treatments and was statistically the same, confirming the results observed with XPS. The amount of immobilized peptide slightly decreased for both peptides after the stability tests, although the percentages of peptide loss were very moderate and overall, 74% or more of the peptides remained on the surface (FLAT-RGD-RG: 95.2%; FLAT-RGD-US: 81.5%; FLAT-YIGSR-RG: 74.2% and FLAT-YIGSR-US: 75.7%). Ultrasonication represents an aggressive mechanical challenge and may remove physisorbed peptides attached through weak bonds [38].Gamma radiation could affect chemical covalent or weak bonding and, consequently, remove a piece or the entire peptide [39]. It should be noted that the CF fluorescent molecule was coupled at the N-terminus of the peptide sequence, i.e. at the opposite of the anchoring regions of the C-terminus, thus, the detection of fluorescence after the RG sterilization indicates that more than 74 % of attached peptides remained entire. These results suggest that the majority of the peptide coatings are stable to RG sterilization and mechanical stress, which both occur during stent implantation.

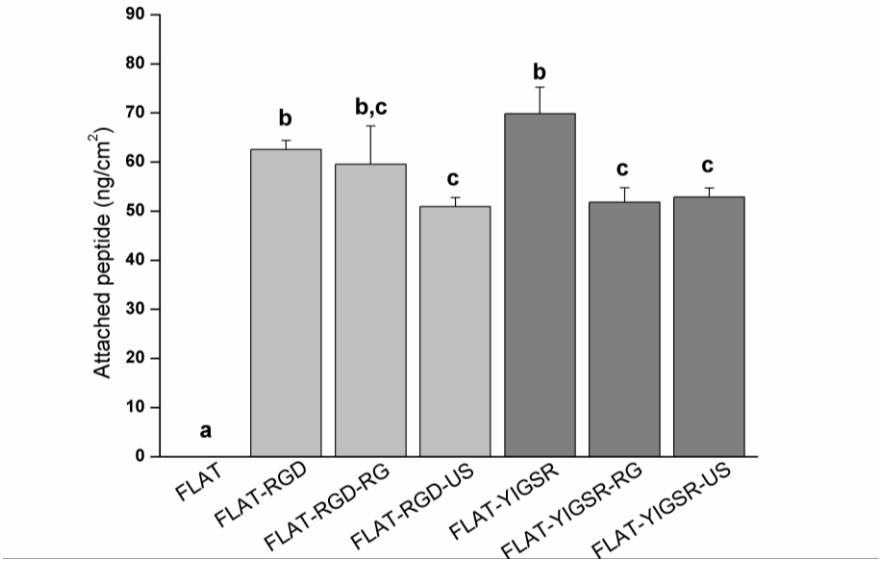

Figure IV.6: *Quantification by indirect fluorescence of the amount of immobilized peptides onto FLAT and biofunctionalized surfaces before (FLAT-RGD and FLAT-YIGSR) and after sterilization with gamma radiation (FLAT-RGD-RG and FLAT-YIGSR-RG) or after ultrasound sonication (FLAT-RGD-US and FLAT-YIGSR-US). Bars designated with different letters belong to statistically different groups (p-value < 0.05).*

3.1. HUVECs adhesion and alignment

The number of adhered HUVECs onto modified CoCr surfaces was evaluated by fluorescent microscopy (**Figure IV.7A**). Polished and patterned non-functionalized surfaces presented the same number of adherent cells, proving that the nanotopography, alone, did not influence HUVECs adhesion onto CoCr surfaces. Previous studies have reported higher cell adhesion on linear patterned surfaces with the same periodicity (i.e. around 10 µm) [3,8,40–42]. However, the investigations on DLIP patterned surfaces described no changes in cell adhesion [1,43], possibly as a result of the relatively low pattern depth (< 1 µm) introduced by this technique and the non-sharp shape of the patterns peaks. Differences in cell area were neither observed between FLAT and 10L surfaces. In contrast, this parameter was statistically reduced on 10H. The reason for such behavior probably relied on the effect of the peaks geometry that acted as a barrier for cellular spreading. Thus, we considered that high depth DLIP patterning had no effect on cell number but reduced slightly the spreading of attached HUVECs.

On the contrary, surface functionalization with the peptides did not modify the cell mean area but significantly increased the number of attached HUVECs, with YIGSR functionalization yielding the highest values of cell adhesion. Indeed, onto RGD and YIGSR functionalized surfaces cell numbers increased approximately 80% and 120%, respectively, compared to the non-functionalized surfaces. The observed increased amount of adhered cells for YIGSR, combined with the fact that this peptide sequence specifically targets ECs [27,29,44], indicates that CoCr functionalization with YIGSR peptides is a feasible way to promote ECs adhesion while avoiding the adhesion of SMCs or platelets [31].

Next, HUVECs alignment was characterized by fluorescent staining of actin fibers (**Figure IV.7A**) and FE-SEM visualization (**Figure IV.7B**). A cell was considered aligned if the angle between the patterned lines and the longest segment of the cell was inferior to 30º. Consequently, a surface having no effect on the ECs orientation should present around 33% of aligned cells. HUVECs alignment was directly related to the pattern dimension. FLAT series and 10L-patterned series, functionalized or not, produced a percentage of HUVECs alignment between 31 and 40 %, and thus had little impact on cellular alignment. The designed patterning of 10H surfaces, however, induced a remarkable alignment of HUVECs, of 79 ± 7 %, 81 ± 12 % and 75 ± 12 % for 10H, 10H-RGD and

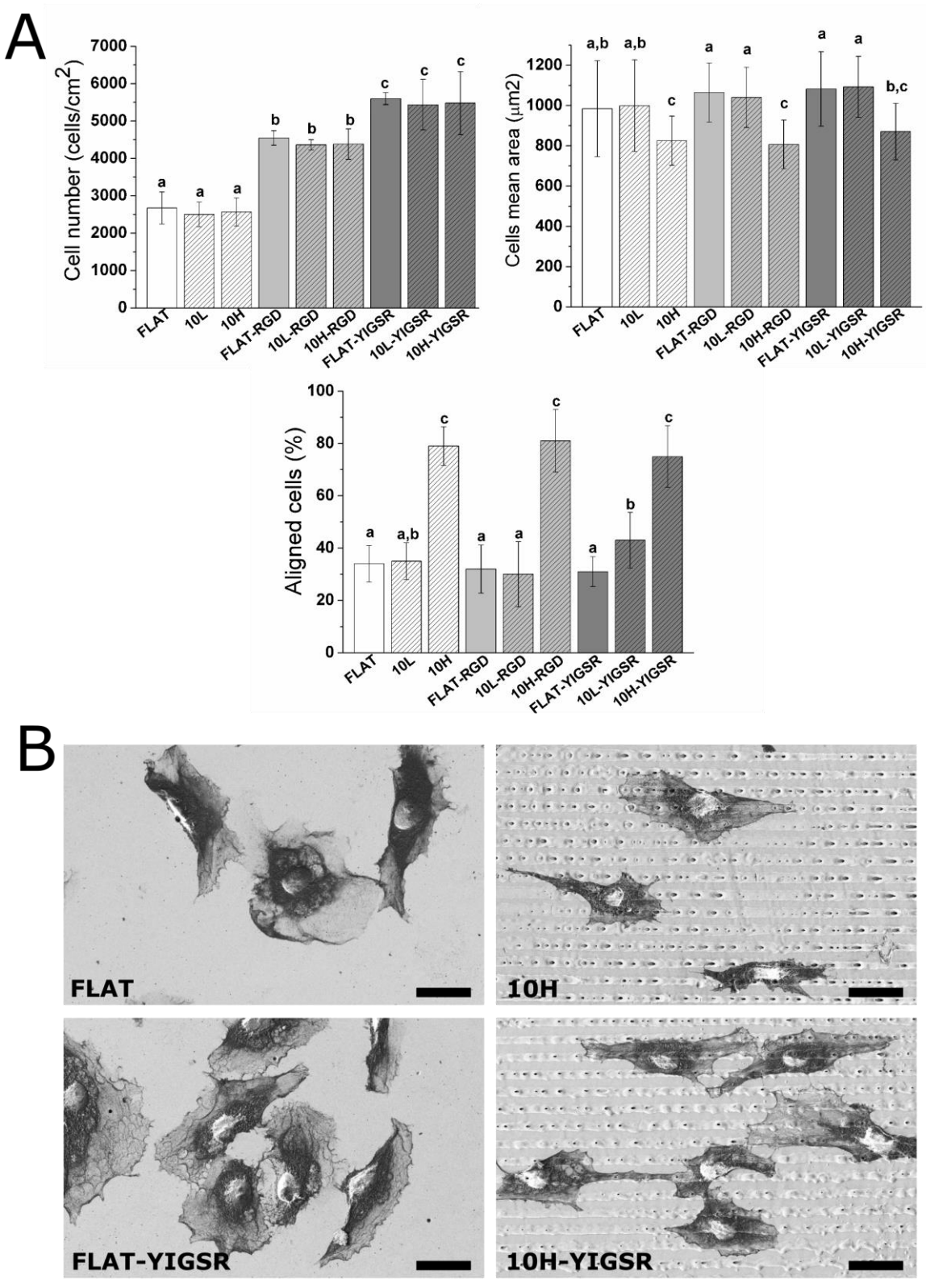

Figure IV.7: *HUVECs adhesion and spreading on FLAT, patterned or/and functionalized CoCr surfaces after 12 h of incubation. (A) Cell number, cells mean area and % of aligned cells were obtained by fluorescent microscopy. Images were analysed with FIJI software. Bars designated with different letters belong to statistically different groups (p-value < 0.05). (B) FE-SEM images of HUVECs on FLAT, 10H, FLAT-YIGSR and 10H-YIGSR surfaces. Scale bar = 30 µm.*

10H-YIGSR, respectively, without statistical differences within tem. Thus, 10H series induced the alignment of HUVECs following the direction of the patterns and reduced HUVECs mean area due to the micro-level of the pattern. Patterns of 10L surfaces had grooves with a depth 10 times smaller than ECs thickness [45] and it is probable that they simply act as a pavement instead of a wall where the HUVECs can easily spread in all directions.

3.2. HUVECs migration

Cell migration was evaluated through the injury coverage ratio, which was defined as the percentage of injury area covered by HUVEC's after 24 h (**Figure IV.8**).

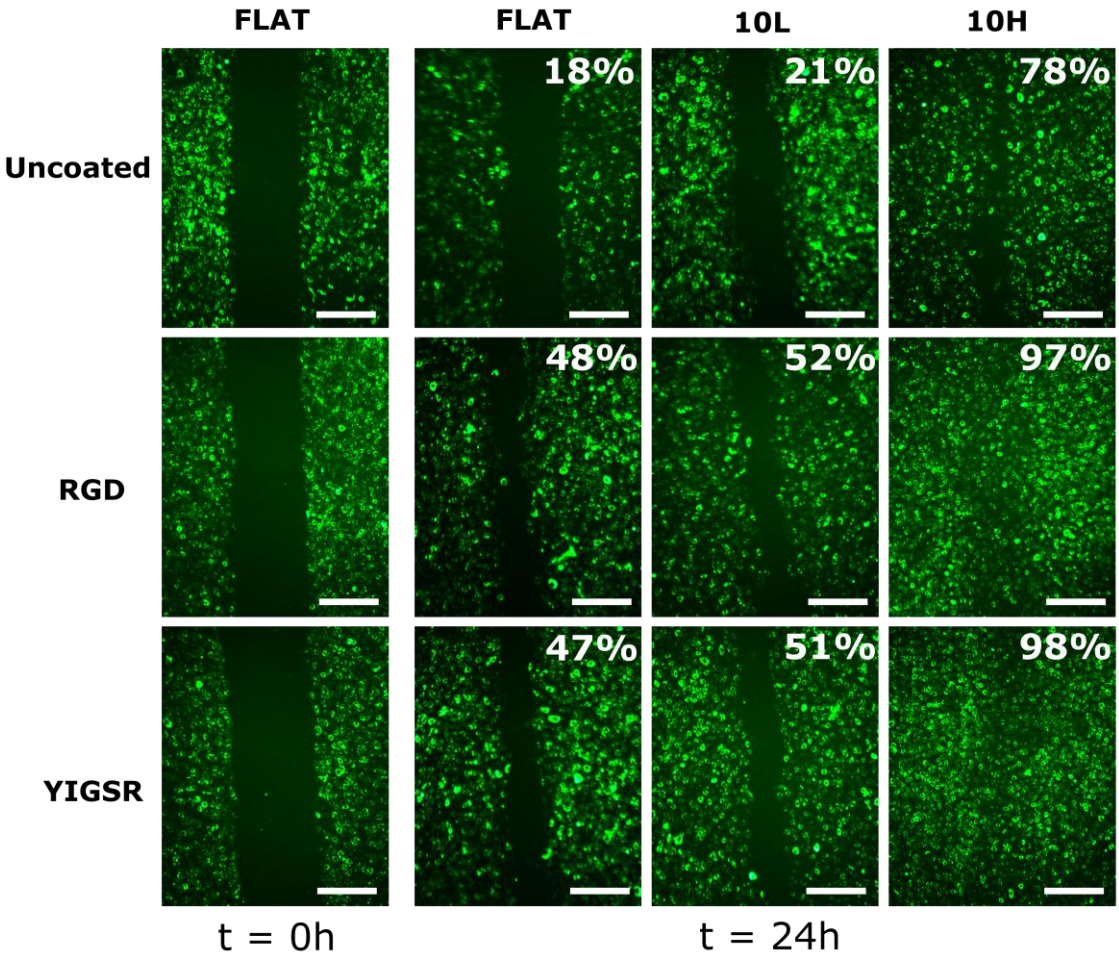

Figure IV.8: *HUVECs migration on FLAT, patterned and/or functionalized CoCr surfaces at 0 h and 24 h timepoints. The percentage indicates the percentage of the respective initial injury area covered by HUVECs at 24 h. Initial gap width = 500 ± 50 µm. Scale bar = 400 µm.*

The migration of HUVECs was observed on all CoCr surfaces. On non-functionalized FLAT and 10L surfaces series injury recovery was of only 18 %

and 21 %, respectively, demonstrating that 10L patterns did not have an effect on HUVECs migration. On the contrary, 10H nanopatterns presented a higher value of 78% of recovery, indicating an accelerated migration, probably due the alignment produced by the patterned topography [3,40,46,47]. When FLAT and 10L CoCr surfaces were functionalized with RGD and YIGSR peptides, HUVECs migration was significantly accelerated (more than 2-fold), with no differences detected between the two peptides. Noteworthy, the combination of 10H nanopatterns and functionalization with RGD and YIGSR peptides significantly improved HUVECs migration compared to all surfaces: 10H-RGD and 10H-YIGSR surfaces presented an almost complete healing of 97 % and 98 %, respectively. This result proves that combining DLIP patterning and functionalization with RGD or YIGSR peptides, which increase HUVECs alignment and adhesion, respectively, synergistically accelerates HUVECs migration after 24 h.

3.3. HUVECs proliferation

The effect of DLIP and RGD and YIGSR functionalization on HUVECs proliferation was assessed by an Alamar blue assay after 2, 5 and 8 days of cell culture (**Figure IV.9**). As expected, HUVECs proliferation increased on all surfaces over time. After 2 days, cell number was significantly higher on all peptide-functionalized surfaces compared to non-functionalized FLAT, 10L and 10H surfaces. After 5 and 8 days, this effect was emphasized. Also linear patterning had an effect and, at 5 and 8 days, a higher cell proliferation was observed on 10H series compared to the respective FLAT and 10L surfaces. This was probably induced by the faster cell migration observed on these nanopatterns. Indeed, when proliferating, cells have less space and are in close contact with other cells. Consequently, due the effect of contact inhibition of proliferation [48,49], proliferation slow down. On a surface generating a faster migration, like 10H surfaces, cells tend to separate from the others faster and consequently proliferation is accelerated compared to surfaces with a slower migration rate like FLAT and 10L surfaces. Finally, after 8 days, surfaces functionalized with YIGSR showed a higher cell number compared to the respective surfaces functionalized with RGD, corroborating the higher potential of YIGSR to direct HUVEC behavior.

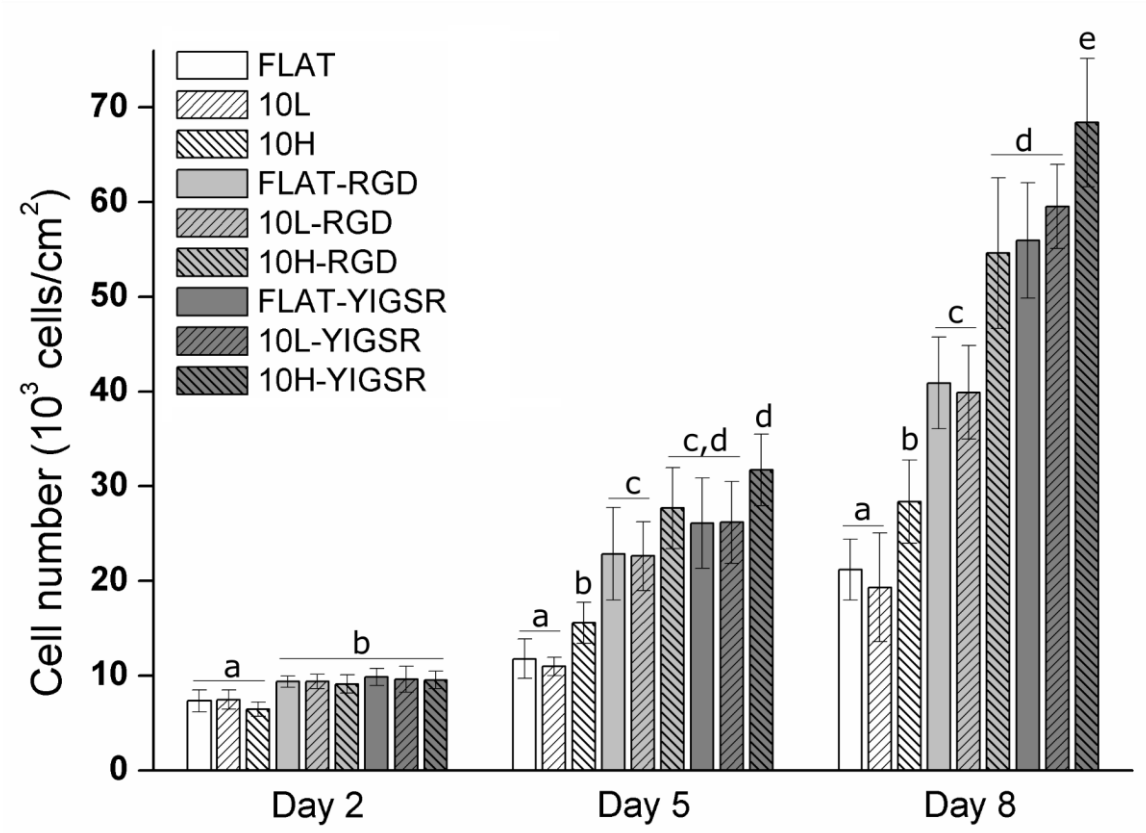

Figure IV.9: *HUVECs proliferation on FLAT, patterned and/or functionalized CoCr surfaces at 2, 5 and 8 days of cell culture obtained by Alamar blue assay. Bars designated with different letters belong to statistically different groups (p-value < 0.05).*

Overall, cell studies determined that peptide functionalization increased ECs adhesion and 10H DLIP patterning induced HUVECs alignment. Noteworthy, the synergy of these two effects on 10H-RGD and 10H-YIGSR surfaces accelerated HUVECs migration and proliferation. Blood circulating in the artery contains a low quantity of ECs. Consequently, the adhesion of ECs on the stent, which would be required to accelerate arterial regeneration, is limited, and, therefore, ECs migration from the surrounding healthy tissue plays a crucial role in the endothelialization process [50,51]. In addition, previous studies demonstrated that DLIP patterned CoCr surfaces are anti-thrombogenic [1] and that CoCr alloy functionalized with YIGSR do not promote high levels of SMC adhesion [31]. Therefore, CoCr alloys patterned by DLIP and functionalized with YIGSR seem to have a great potential to accelerate endothelium healing without generating platelet aggregation and SMC proliferation.

4. Conclusions

In this work, we explored the possibility to increase specifically ECs adhesion, migration and proliferation on CoCr surfaces by combining topographical modification and biofunctionalization techniques.

Flat CoCr surfaces were successfully modified by DLIP technique obtaining linear nanopatterned surfaces. These nanotopographies did not modify the corrosion properties and the surface charge of the CoCr alloy.

To evaluate the combined effect of topographical modifications with biofunctionalization, RGD and YIGSR cell adhesive peptides were covalently immobilized to the surfaces through CPTES silanization. The coatings were characterized by physico-chemical methods and, moreover, showed stability against gamma radiation sterilization and ultrasonication.

Cell studies indicated that RGD and YIGSR-coated surfaces induce a significant increase in ECs adhesion compared to non-functionalized surfaces. Moreover, 10H pattern surfaces aligned the 80 % of adhered ECs while 10L did not affect cell alignment. When 10H patterned surfaces were functionalized, an accelerated ECs migration and proliferation was observed. Consequently, a positive synergy between surface linear patterning and functionalization was described. Therefore, DLIP patterned surfaces functionalized with RGD or YIGSR hold great potential to overcome clinical limitations of current stents by enhancing surface endothelialization.

References

(1) Schieber, R.; Lassarre, F.; Hans, M.; Fernandez-Yague, M.; Diaz-Ricart, M.; Escolar, G.; Ginebra, M.-P.; Mucklich, F.; Pegueroles, M. Direct Laser Interference Patterning of CoCr Alloy Surfaces to Control Endothelial Cell and Platelet Response for Cardiovascular Applications. *Accept. Adv. Healthc. Mater.* **2016**.

(2) Zorlutuna, P.; Rong, Z.; Vadgama, P.; Hasirci, V. Influence of Nanopatterns on Endothelial Cell Adhesion: Enhanced Cell Retention under Shear Stress. *Acta Biomater.* **2009**, *5* (7), 2451–2459.

(3) Biela, S. a; Su, Y.; Spatz, J. P.; Kemkemer, R. Different Sensitivity of Human Endothelial Cells, Smooth Muscle Cells and Fibroblasts to Topography in the Nano-Micro Range. *Acta Biomater.* **2009**, *5* (7), 2460–2466.

(4) Liliensiek, S. J.; Wood, J. a; Yong, J.; Auerbach, R.; Nealey, P. F.; Murphy, C. J. Modulation of Human Vascular Endothelial Cell Behaviors by Nanotopographic Cues. *Biomaterials* **2010**, *31* (20), 5418–5426.

(5) Morgan, J. T.; Wood, J. a; Shah, N. M.; Hughbanks, M. L.; Russell, P.; Barakat, A. I.; Murphy, C. J. Integration of Basal Topographic Cues and Apical Shear Stress in Vascular Endothelial Cells. *Biomaterials* **2012**, *33* (16), 4126–4135.

(6) Falconnet, D.; Csucs, G.; Michelle Grandin, H.; Textor, M. Surface Engineering Approaches to Micropattern Surfaces for Cell-Based Assays. *Biomaterials* **2006**, *27* (16), 3044–3063.

(7) Guillem-Marti, J.; Delgado, L.; Godoy-Gallardo, M.; Pegueroles, M.; Herrero, M.; Gil, F. J. Fibroblast Adhesion and Activation onto Micro-Machined Titanium Surfaces. *Clin. Oral Implants Res.* **2013**, *24* (7), 770–780.

(8) Lu, J.; Rao, M. P.; MacDonald, N. C.; Khang, D.; Webster, T. J. Improved Endothelial Cell Adhesion and Proliferation on Patterned Titanium Surfaces with Rationally Designed, Micrometer to Nanometer Features. *Acta Biomater.* **2008**, *4* (1), 192–201.

(9) Li, Y.; Thouas, G. a; Chen, Q.-Z. Biodegradable Soft Elastomers: Synthesis/properties of Materials and Fabrication of Scaffolds. *RSC Adv.* **2012**, *2* (22), 8229–8242.

(10) Mucklich, F.; Lasagni, A.; Daniel, C. Laser Interference Metallurgy – Using Interference as a Tool for Micro/nano Structuring. *Int. J. Mater. Res* **2006**, *97*, 1337–1344.

(11) Mas-Moruno, C.; Fraioli, R.; Albericio, F.; Manero, J. M.; Gil, F. J. Novel Peptide-Based Platform for the Dual Presentation of Biologically Active Peptide Motifs on Biomaterials. *ACS Appl. Mater. Interfaces* **2014**, *6*, 6525–6536.

(12) Horcas, I.; Fernández, R.; Gómez-Rodríguez, J. M.; Colchero, J.; Gómez-Herrero, J.; Baro, A. M. WSXM: A Software for Scanning Probe Microscopy and a Tool for Nanotechnology. *Rev. Sci. Instrum.* **2007**, *78* (1).

(13) International Organization for Standardization. Biological Evaluation of Medical Devices - Part 15: Identification and Quantification of Degradation Products from Metals and Alloys, 2000.

(14) Tzoneva, R.; Heuchel, M.; Groth, T.; Altankov, G.; Albrecht, W.; Paul, D. Fibrinogen Adsorption and Platelet Interactions on Polymer Membranes. *J. Biomater. Sci. Polym. Ed.* **2002**, *13* (9), 1033–1050.

(15) Schindelin, J.; Arganda-Carreras, I.; Frise, E.; Kaynig, V.; Longair, M.; Pietzsch, T.; Preibisch, S.; Rueden, C.; Saalfeld, S.; Schmid, B.; Tinevez, J.-Y. J.-Y.; White, D. J.; Hartenstein, V.; Eliceiri, K.; Tomancak, P.; Cardona, A.; Liceiri, K.; Tomancak, P.; A., C. Fiji: An Open Source Platform for Biological Image Analysis. *Nat. Methods* **2012**, *9* (7), 676–682.

(16) Lasagni, a.; Mücklich, F. FEM Simulation of Periodical Local Heating Caused by Laser Interference Metallurgy. *J. Mater. Process. Technol.* **2009**, *209* (1), 202–209.

(17) von Allmen, M.; Blatter, A. *Laser-Beam Interactions with Materials. Physical Principles and Applications*, Springer S.; 1995.

(18) Hans, M.; Müller, F.; Grandthyll, S.; Hüfner, S.; Mücklich, F. Applied Surface Science Anisotropic Wetting of Copper Alloys Induced by One-Step Laser Micro-Patterning. **2012**, *263*, 416–422.

(19) Dayan, A. D.; Paine, A. J. Mechanisms of Chromium Toxicity, Carcinogenicity and Allergenicity: Review of the Literature from 1985 to 2000. *Hum. Exp. Toxicol.* **2001**, *20* (9), 439–451.

(20) Chen, Q.; Thouas, G. A. Metallic Implant Biomaterials. *Mater. Sci. Eng. R Reports* **2015**, *87*, 1–57.

(21) Madl, A. K.; Kovochich, M.; Liong, M.; Finley, B. L.; Paustenbach, D. J.; Oberdörster, G. Toxicology of Wear Particles of Cobalt-Chromium Alloy Metal-on-Metal Hip Implants Part II: Importance of Physicochemical Properties and Dose in Animal and in Vitro Studies as a Basis for Risk Assessment. *Nanomedicine Nanotechnology, Biol. Med.* **2015**, *11* (5), 1285–1298.

(22) Schnitzer, C.; Ripperger, S. Influence of Surface Roughness on Streaming Potential Method. *Chem. Eng. Technol.* **2008**, *31* (11), 1696–1700.

(23) Hersel, U.; Dahmen, C.; Kessler, H. RGD Modified Polymers: Biomaterials for Stimulated Cell Adhesion and beyond. *Biomaterials* **2003**, *24* (24), 4385–4415.

(24) Pierschbacher, M. D.; Ruoslahti, E. Cell Attachment Activity of Fibronectin Can Be Duplicated by Small Synthetic Fragments of the Molecule. *Nature* **1984**, *309* (5963), 30–33.

(25) Zheng, W.; Wang, Z.; Song, L.; Zhao, Q.; Zhang, J.; Li, D.; Wang, S.; Han, J.; Zheng, X.-L.; Yang, Z.; Kong, D. Endothelialization and Patency of RGD-Functionalized Vascular Grafts in a Rabbit Carotid Artery Model. *Biomaterials* **2012**, *33* (10), 2880–2891.

(26) Hoesli, C. a; Garnier, A.; Juneau, P.-M.; Chevallier, P.; Duchesne, C.; Laroche, G. A Fluorophore-Tagged RGD Peptide to Control Endothelial Cell Adhesion to Micropatterned Surfaces. *Biomaterials* **2014**, *35* (3), 879–890.

(27) Hubbell, J. A.; Massia, S.; Desai, N.; Drumheller, P. Endothelial Cell-Selective Materials for Tissue Engineering in the Vascular Graft via a New Receptor. *Narure Biotechnol.* **1991**, *9*, 568–572.

(28) Jun, H.-W.; West, J. Development of a YIGSR-Peptide-Modified Polyurethaneurea to Enhance Endothelialization. *J. Biomater. Sci. Polym. Ed.* **2004**, *15* (1), 73–94.

(29) Jun, H.-W.; West, J. L. Endothelialization of Microporous YIGSR/PEG-Modified Polyurethaneurea. *Tissue Eng.* **2005**, *11* (7–8), 1133–1140.

(30) Jun, H.-W.; West, J. L. Modification of Polyurethaneurea with PEG and YIGSR Peptide to Enhance Endothelialization without Platelet Adhesion. *J. Biomed. Mater. Res. B. Appl. Biomater.* **2005**, *72* (1), 131–139.

(31) Castellanos, M. I.; Mas-Moruno, C.; Grau, A.; Serra-Picamal, X.; Trepat, X.; Albericio, F.; Joner, M.; Manero, J. M.; Pegueroles, M. Functionalization of CoCr Surfaces with Cell Adhesive Peptides to Promote HUVECs Adhesion and

Proliferation. *Appl. Surf. Sci.* **2016**, *393*, 82–92.

(32) Mas-Moruno, C.; Dorfner, P. M.; Manzenrieder, F.; Neubauer, S.; Reuning, U.; Burgkart, R.; Kessler, H. Behavior of Primary Human Osteoblasts on Trimmed and Sandblasted Ti6Al4V Surfaces Functionalized with Integrin αvβ3-Selective Cyclic RGD Peptides. *J. Biomed. Mater. Res. A* **2013**, *101* (1), 87–97.

(33) Tan, G.; Zhang, L.; Ning, C.; Liu, X.; Liao, J. Preparation and Characterization of APTES Films on Modification Titanium by SAMs. *Thin Solid Films* **2011**, *519* (15), 4997–5001.

(34) Kim, J.; Seidler, P.; Wan, L. S.; Fill, C. Formation, Structure, and Reactivity of Amino-Terminated Organic Films on Silicon Substrates. *J. Colloid Interface Sci.* **2009**, *329* (1), 114–119.

(35) Sargeant, T. D.; Rao, M. S.; Koh, C.-Y.; Stupp, S. I. Covalent Functionalization of NiTi Surfaces with Bioactive Peptide Amphiphile Nanofibers. *Biomaterials* **2008**, *29* (8), 1085–1098.

(36) Healy, K. E.; Ducheyne, P. Oxidation Kinetics of Titanium Thin Films in Model Physiologic Environments. *J. Colloid Interface Sci.* **1992**, *150* (2), 404–417.

(37) Rezania, A.; Johnson, R.; Lefkow, A. R.; Healy, K. E. Bioactivation of Metal Oxide Surfaces. 1. Surface Characterization and Cell Response. *Langmuir* **1999**, *15* (20), 6931–6939.

(38) Godoy-Gallardo, M.; Mas-Moruno, C.; Yu, K.; Manero, J. M.; Gil, F. J.; Kizhakkedathu, J. N.; Rodriguez, D. Antibacterial Properties of hLf1-11 Peptide onto Titanium Surfaces: A Comparison Study between Silanization and Surface Initiated Polymerization. *Biomacromolecules* **2015**, *16* (2), 483–496.

(39) Yang, Y.; Porte, M. C.; Marmey, P.; El Haj, A. J.; Amedee, J.; Baquey, C. Covalent Bonding of Collagen on poly(L-Lactic Acid) by Gamma Irradiation. *Nucl. Instruments Methods Phys. Res. Sect. B Beam Interact. with Mater. Atoms* **2003**, *207* (2), 165–174.

(40) Song, K. H.; Kwon, K. W.; Song, S.; Suh, K.-Y.; Doh, J. Dynamics of T Cells on Endothelial Layers Aligned by Nanostructured Surfaces. *Biomaterials* **2012**, *33* (7), 2007–2015.

(41) Palmaz, J. C.; Benson, A.; Sprague, E. A. Influence of Surface Topography on Endothelialization of Intravascular Metallic Material. *J. Vasc. Interv. Radiol.* **1999**,

10 (4), 439–444.

(42) Ranjan, A.; Webster, T. J. Increased Endothelial Cell Adhesion and Elongation on Micron-Patterned Nano-Rough Poly(dimethylsiloxane) Films. *Nanotechnology* **2009**, *20* (30), 305102–305112.

(43) Fayou Yu, Frank Mucklich, Ping Li, Hao Shen, S. M.; Claus-Michael Lehr, and U. B. In Vitro Cell Response to a Polymer Surface Micropatterned by Laser Interference Lithography. *Biomacromolecules* **2005**, *6*, 1160–1167.

(44) Massia, S. P.; Hubbell, J. A. Convalent Surface Immobilization of Arg-Gly-Asp- and Tyr-Ile-Gly-Ser-Arg-Containing Peptides to Obtain Well-Defined Cell-Adhesive Substrates. *Anal. Biochem.* **1990**, *187* (2), 292–301.

(45) Alberts, B.; Johnson, A.; Lewis, J. *Molecular Biology of the Cell*, 4th editio.; Science, N. Y. G., Ed.; 2002.

(46) Teichmann, J.; Morgenstern, A.; Seebach, J.; Schnittler, H.-J.; Werner, C.; Pompe, T. The Control of Endothelial Cell Adhesion and Migration by Shear Stress and Matrix-Substrate Anchorage. *Biomaterials* **2012**, *33* (7), 1959–1969.

(47) Bouta, E. M.; McCarthy, C. W.; Keim, A.; Wang, H. B.; Gilbert, R. J.; Goldman, J. Biomaterial Guides for Lymphatic Endothelial Cell Alignment and Migration. *Acta Biomater.* **2011**, *7* (3), 1104–1113.

(48) McClatchey, A. I.; Yap, A. S. Contact Inhibition (of Proliferation) Redux. *Curr. Opin. Cell Biol.* **2012**, *24* (5), 685–694.

(49) Cho, E. H.; Dai, Y. SIRT1 Controls Cell Proliferation by Regulating Contact Inhibition. *Biochem. Biophys. Res. Commun.* **2016**, *478* (2), 868–872.

(50) Wei, Y.; Ji, Y.; Xiao, L. L.; Lin, Q. kui; Xu, J. ping; Ren, K. feng; Ji, J. Surface Engineering of Cardiovascular Stent with Endothelial Cell Selectivity for in Vivo Re-Endothelialisation. *Biomaterials* **2013**, *34* (11), 2588–2599.

(51) Kouvroukoglou, S.; Dee, K. C.; Bizios, R.; McIntire, L. V; Zygourakis, K. Endothelial Cell Migration on Surfaces Modified with Immobilized Adhesive Peptides. *Biomaterials* **2000**, *21* (17), 1725–1733.

Chapter V: Solvent-cast poly(L-lactic acid) surfaces functionalized by sodium hydroxide etching, oxygen plasma or cutinase enzyme hydrolysis for 3D-printed bioresorbable stent fabrication

1. Introduction

Surface modifications onto biomaterials are a common approach to control biological response and could be classified in three main categories. First, topographical modifications that obtain specific nano- or micro- patterned surfaces can accelerate ECs migration [1,2]. Second, physico-chemical modifications that generate suitable functional groups [3,4] and/or modulate surface energy [5,6] have demonstrated to modify ECs adhesion and spreading. Third, surface biofunctionalization by immobilizing specific biomolecules derived from extracellular matrix (ECM) proteins that have selectivity for ECs, could facilitate a cascade of biological events and eventually regenerate the damaged area with a functional endothelium [7–9]. A strong covalent bonding between the implant and the biomolecules is desired to obtain a stable biofunctionalization [10]. The most common chemical routes to obtain covalent bonding are the generation of functional groups at the surface, generally carboxyl (– COOH) or hydroxyl (– OH) groups, which react with a specific part of the biomolecule. Consequently, modifications that increase surface implant functional groups are of double interest since they could increase biocompatibility and enhance biofunctionalization. In that sense, surface treatments such as cold plasma treatment [11–13], ultraviolet irradiation [3], sodium hydroxide (NaOH) etching [14,15] or ozone irradiation [4] have shown to ameliorate surface functionalization. Also, enzymatic treatments have been proposed and successfully used for the surface modification of natural and synthetic polymers [9,16]. For polyesters, such as PLLA, the hydrolysis of the ester bond by applying cutinase enzymes generate new hydroxyl and carboxyl groups onto the surface [9,17].

Also, common stent fabrication processes do not allow to personalized stent shape. Consequently, in complex arteries stent implantation is impossible. 3D-printing could be a strategy to produce each stent with a shape fully complementary to the target damaged artery. In particular, solvent-cast direct write technique have shown promising results to obtain complex 3D-printed shapes with PLLA inks [18].

The aim of this work was to elaborate and characterize solvent-casted PLLA functionalized surfaces to enhance ECs adhesion and to assess the use of this

process and biomaterial to fabricate 3D-printed BRS. To assess biocompatibility, mechanical and degradation properties of the modified PLLA by solvent-casting it was evaluated cytotoxicity, crystallinity, molecular weight, Young modulus, ultimate tensile strength (UTS) and degradation rates. The effect of the different functionalization processes on PLLA properties was compared by characterizing surface roughness, surface wettability, films degradation, surface chemical properties and ECs adhesion. Finally, 3D-printed PLLA bioresorbable stent were obtained by the solvent-cast direct write technique to assess its feasibility.

2. Materials and methods

2.1. Materials

Medical grade poly-L-lactic acid (PLLA) pellets (PURASORB PL65, $M_w \approx 1650000$ g/mol) were obtained from Purac Biomaterials (Gorinchem, Netherlands). PLLA pellets were stored in a desiccator at room temperature (RT).

Commercial PLLA films of 50 µm thick with a 37 % crystallinity (ME331050, Goodfellow, Coraopolis, USA) were used as reference. Samples made of this commercial films were coded as **COM**.

Biodegradable PLLA peripheral stent REMEDY (Kyoto Medical Planning, Japan) was used in this study as positive control. Sample made of this commercial stent were coded as **STNT**.

Humicola insolens cutinase enzyme (HiC) was kindly provided by Novozymes (Beijing, China) and used as received without any purification steps.

Cellular experiments were conducted using HUVECs in the exact same conditions as in Chapter III (section 2.1.).

2.2. PLLA films by solvent casting

The PLLA films were manufactured by solvent-casting method [19]. Previously, PLLA pellets were dried in an oven with controlled argon atmosphere at 80ºC for 2 h. Then, PLLA pellets were dissolved in chloroform (Sigma-Aldrich, Germany) at a 3.6% weight versus volume (w/v) ratio. The dissolution took approximately 48 h on an orbital shaker at RT. Once the PLLA was completely dissolved, the obtained paste was spread on a 150 mm diameter glass petri dish and

maintained 48 h under a chloroform saturated atmosphere to decrease the solvent evaporation rate. The studied surface was the one in contact with the glass petri dish. The obtained films had a thickness of approximately ≈ 150 µm. The obtained films were coded as **SC**. To increase crystallinity, the films were thermally treated at 80ºC during 12 h and coded as **TT**. Finally, to characterize the films, they were cut into 10 mm diameter discs.

2.3. PLLA films surface activation

Three different techniques of surface activation were applied to the fabricated TT films:

- **Cold plasma:** Low pressure oxygen plasma in a 13.56 MHz radiofrequency reactor Diener Femto (Diener, Germany) was applied to TT films. At the center of the reactor an oxygen plasma was generated at 0.4 mbar pressure and 100 W discharge power during 2 min. Details on the experimental setting can be found in a previous study [20]. Obtained samples were coded as **PL**.
- **Chemical etching:** TT films were chemically activated by submerging the samples in a 1 M sodium hydroxide (NaOH) solution under sonication during 1 h at RT. After, treated samples were cleaned twice in distilled water during 30 min to remove NaOH residues and samples were coded as **NA**.
- **Enzyme treatment:** Previously to cutinase enzymes activation, TT films were prewashed as described in a previous study [21]. Briefly, samples were submerged successively in L-1 Triton X100, Na_2CO_3 solution and double distilled water (ddH_2O) for 30 min at 37°C and 130 rpm. After, cutinase enzymes were diluted in 100 mM Tris-HCl buffer with a pH=7 to obtain a 10 µM enzyme solution. The films were immersed in 1 ml of the enzyme solution at 37ºC on an orbital shaker at 100 rpm during 24 h. Finally, films were cleaned with the previous protocol and obtained samples were coded as **ENZ**.

2.4. PLLA films characterization

Gel permeation chromatography (GPC) analyses were performed in an Agilent HPLC chromatograph 1260 Infinity series (Agilent Technologies, USA). Separation was carried in a Waters Styragel HR 5E column (USA) using $CHCl_3$ (HPLC grade) as eluent. Samples with concentration between 0.2 to 0.4 mg/ml

were analyzed. The used flow was of 0.4 ml/min and the amount of injected samples was 20 µl. Molecular weights were calculated after calibration with PMMA standards from Sigma-Aldrich (Germany), molecular weight calibration range was between 2.7 million to 2 thousands Dalton. Calculations were performed with the Chemstation Software (Agilent Technologies).

Thermal analysis of the different PLLA samples were obtained by differential scanning calorimetry (DSC) with the instrument DSC 2920 Modulated (TA Instruments, USA) and following the ASTM D3418-03 standard [22]. An empty aluminum pan was used as reference. 10 ng samples were run in a nitrogen atmosphere at 10ºC.min^{-1} heating ramp from 20 to 220ºC. The enthalpy of fusion (ΔHm) and the enthalpy of crystallization (ΔHcc) were obtained from the scan and used to calculate the percentage of crystallinity through the equation $Xc = (\Delta Hm - \Delta Hcc) / \Delta H^0m$ where $\Delta H^0m = 93$ J/g is the enthalpy of fusion of a 100% crystalline PLLA [23,24].

Mechanical properties of PLLA films were determined by tensile test (DY 34, Adamel Lhomargy, France) according to the standard ASTM D882 – 02 [25] using a 100 N load cell. First, PLLA films were cut following the standard ASTM D6287 – 98 [26] to obtain for each studied condition 5 samples of 150 mm length and 10 mm width. The rate of grip separation was set to 15 mm/min and the curve load versus extension was recorded at RT. From the curve, Young modulus (E) and ultimate tensile strength (UTS) were obtained.

To detect residues of chloroform in the PLLA films energy-dispersive X-ray spectroscopy (EDX) was performed with a Zeiss Neon40 FE-SEM microscope (Carl Zeiss NTS GmbH, Germany). Five measurements at 7 kV were done for each condition.

The *in vitro* cytotoxicity of the PLLA films was evaluated by extracts using lactate dehydrogenase (LDH) enzyme measurement on HUVECs. The extracts were prepared according to ISO 10993-5 [27] submerging the different fabricated PLLA films in complete cell medium for 3 days at 37ºC. Then, the extracts were serially diluted into five concentrations as 1/1; 1/2; 1/10; 1/100 and 1/1000 with fresh complete cell medium. Previously, PLLA films were sterilized in ethanol 70% during 30 min. Cells were seeded in a 96-well tissue polystyrene (TCPS) cell

culture plate at a seeding density of 15000 HUVECs/well and incubated normally for 24 h to allow attachment. After, cell medium was replaced by 200 µl of the different extract dissolutions. Complete fresh medium was used as negative control and complete fresh medium without cells was used as positive control. After 24h, alive HUVECs were quantified by measuring lactate dehydrogenase (LDH) enzyme. Briefly, cells were rinsed with PBS and lysed with 350 µl of mammalian protein extraction reagent (M-PER) (Thermo Scientific, Germany). The activity of LDH was determined by measuring the spectrophotometrical absorbance with a commercial LDH kit (Cytotoxicity Detection Kit, Roche Diagnostics, Mannheim, Germany) by a microplate reader (Infinite M200 PRO, Tecan Group Ltd., Switzerland) at 490 nm. According to the standard, cell viability was calculated with the following equation: cell viability = $(Abs_{sample} - Abs_{C+}/(Abs_{C-} - Abs_{C+})$ where Abs_{sample} is the sample absorbance, Abs_{C+} is the positive control absorbance and Abs_{C-} is the negative control absorbance. The results were shown by the percentages. Morphological signs of cell death were visible when the values of cell survival were below the level of 80% which was referred to as a threshold to define a cytotoxic response.

2.5. Surface characterization

Topography was evaluated with white light interferometry (WLI) (Optical interferometer Veeco Wyko 9300NT, Veeco Instruments, USA) in vertical scanning interferometry mode (VSI) at 100x magnification. Data analysis was performed with Wyko Vision 4.10 software (Veeco Instruments) to obtain the roughness parameter Ra (the arithmetic average height). Curvature and tilt were eliminated with a Gaussian filter.

Water static contact angle was measured by the sessile drop method with a Contact Angle System OCA15plus (Dataphysics, Germany) [28]. Milli-Q® water drops of 3 µl were deposited on the PLLA films and the contact angle between water and the different PLLA films was measured. An average of 15 drops were studied for each condition. The contact angle values were obtained after applying Laplace-Young fitting of the drop profile with SCA 20 software (Dataphysics).

The chemical composition of PLLA films surface before and after topographical modification was analyzed by X-ray photoelectron spectroscopy (XPS) (SPECS

Surface NanoAnalysis GmbH, Berlin, Germany). The XPS spectra were obtained using an Mg anode XR50 operating at 150 W and a Phoibos 150 MCD-9 detector to record high resolution spectra at a pressure below 7.5×10^{-9} mbar. The elements present on the surface were evaluated by low-resolution survey spectra, whereas high-resolution of C 1s was recorded with detector pass energy fixed at 25 eV with 0.1 eV step at a pressure below 7.5×10^{-9} mbar. Casa XPS software (Version 2.3.16, Casa Software Ltd., Teignmouth, UK) was used to do fitting, peak integration of spectra and peaks deconvolution. Binding energies were referred to the C-C bond energy at 284.8 eV.

2.6. PLLA films degradation

To compare the rate of degradation of the different PLLA films compared to STNT an accelerated degradation assay was performed in alkaline solution [29–31]. First, in order to have the same ratio surface/volume for each condition, all the PLLA films were cut in fibers with the same diameter as STNT stent strut (≈ 150 µm). All samples (COM, STNT, SC, TT, PL, NA and ENZ) were dried in an argon atmosphere oven at 48ºC during 2 h and weighted with a Sartorius Quintix35-1S laboratory balance (Göttingen, Germany). Next, all samples were placed at 37ºC in a solution of 0.1 M NaOH. At 2, 4, 7 and 10 days samples were weighted in order to calculate the mass loss. Also, initial and final samples surface were observed by scanning electron microscopy (SEM) with a Zeiss Neon40 FE-SEM microscope (Carl Zeiss NTS GmbH, Germany). For each sample, five images were taken at a working distance of 6 mm and a potential of 5 kV. Finally, samples topography was characterized by WLI, as previously described (section 2.7), to evaluate changes between final (Ra_f) and initial (Ra_i) mean roughness, the ratio Ra_f/Ra_i was calculated.

2.7. HUVECs adhesion

Cell adhesion assay was performed by seeding HUVEC at a density of $5x10^4$ cells/sample with serum-free medium and cellular analyses were carried out at 12 h after cell seeding. The different PLLA samples were previously sterilized in ethanol 70% during 15 min at RT. To quantify the density of adhered HUVECs after 12 h, the release of LDH enzyme was measured as previously described for the indirect cytotoxicity assay (section 2.6). In parallel, cell adhesion was

observed by scanning electron microscopy (Zeiss Neon40 FE-SEM microscope, Carl Zeiss NTS GmbH, Germany). To that end, HUVECs were fixed with glutaraldehyde (G400-4, Sigma-Aldrich), dehydrated by immersion in different solutions of increasing ethanol % and, finally, sputtered with gold-palladium coating. For each sample, ten images were taken at a working distance of 6 mm and a potential of 5 kV. The percentage of area covered by HUVEC was determined using FIJI ImageJ software [32].

2.8. 3D-printed BRS obtained by solvent-cast direct write technique

The 3D-printed PLLA stent were obtained using a fused deposition modelling 3D printer (BCN 3D+, BCN 3D technologies, Barcelona, Spain). The printer was modified to solvent cast PLLA inks though a syringe micronozzle with a 250 µm inner diameter (Nordson®, USA). PLLA inks were prepared as described in section 2.2 and printing was realized at a (0.4) $mm^3.s^{-1}$ flux and 4 $mm.s^{-1}$ robot velocity. Also, the printer Y axe was modified by introducing a carbon fiber rotating mandrel in order to print cylindrical structures. The BRS shape was adjust from the Igaki-Tamai stent (Kyoto Medical Planning, Japan) design structure and dimensions were 5 mm diameter and 20 mm length.

2.9. Statistical analysis

The experimental data collected in this study are reported as mean ± standard deviation. A one way analysis of variance (ANOVA) was used to determine the statistical significance of difference at $p<0.05$ (Minitab 16.2.2 Statistical Software, Minitab Inc.). Unless otherwise specified, all experiments were performed with at least n=3 samples for each specimen group. In addition, each experiment was repeated at least twice.

3. Results and discussion

The aim of this study was to evaluate solvent-casted and functionalized PLLA to enhance ECs adhesion and its use as biomaterial for stent fabrication by 3D printing. To this end, the effect of solvent casting and functionalization processes onto PLLA biocompatibility, degradation and mechanical properties were evaluated. In parallel, surface functional groups density was measured to compare the effect of NaOH, oxygen plasma and cutinase enzymes activation

surface treatments. Finally, as a proof of concept, 3D-printed PLLA stent were obtained by the solvent-cast direct write technique.

3.1. PLLA film properties

To evaluate potential cytotoxic effects of the solvent employed for the synthesis of the PLLA films and/or the different activation treatments, an indirect cytotoxicity assay was performed (**Table V.1**). The standard specifies that a material is cytotoxic if the percentage of cell survival is inferior to 80 %. The results indicated that SC samples were cytotoxic but thermal treatment increased cell viability reaching values of non-cytoxicity, higher than 92%, as observed for TT samples. Activation treatments of oxygen plasma and enzyme treatment did not affect cytotoxicity of TT films. But, NA samples presented cytotoxicity in some cases probably due to NaOH residues in the obtained films.

The presence of chlorine residues from solvent casting fabrication was verified by EDS (**Table V.2**). COM and SC were the only films presenting Cl residues. As chloroform toxicity is well known [33,34], the cytotoxicity of SC observed previously was probably due to this residual chloroform in the film. Also, the absence of Cl in TT films suggested that thermal treatment helped PLLA solvent-cast films to be biocompatible by evaporating chloroform residues.

Table V.1: *Cell viability on the different solvent-cast PLLA films. Results correspond to the percentage of alive cells after an indirect cytotoxicity assay. 1/1, 1/2, 1/10, 1/100, 1/1000 are different dilutions of the medium which have been previously in contact 72 h with the respective PLLA films. In red it is indicated cell cytotoxic surfaces.*

	Cell viability (%)				
Sample	1/1	1/2	1/10	1/100	1/1000
SC	45 ± 26	70 ± 13	67 ± 12	79 ± 16	94 ± 12
TT	95 ± 3	95 ± 4	92 ± 4	102 ± 15	96 ± 7
PL	101 ± 4	113 ± 6	122 ± 16	116 ± 12	113 ± 18
NA	95 ± 15	92 ± 19	76 ± 12	86 ± 7	123 ± 13
ENZ	98 ± 11	112 ± 24	111 ± 25	112 ± 12	121 ± 21

PLLA PL65 from Purac was chosen for its particularly high molecular weight and crystallinity in order to fabricate PLLA films with mechanical and degradation properties similar to actual PLLA BRS. **Table V.2** shows the results obtained of GPC and DSC techniques since solvent casting and activation treatments could reduce molecular weight and crystallinity. Generally, all the processed films presented M_w values in the same range, from 0,89 up to 0,98 x 10^6 g/mol. But STNT presented a M_w five times lower than SC films. SC and TT films presented statistically similar molecular weight, respectively 0.95 ± 0.04 and 0.98 ± 0.03 10^6 g/mol. Thus, thermal treatment did not significantly affect PLLA chain: nor by generating polymerization, neither by degrading PLLA. The three functionalizing treatments could break PLLA chains and, consequently, reduce PLLA films M_w. No significant changes were observed after plasma activation (PL) and enzyme hydrolysis (ENZ) suggesting that these processes work at the outermost surface layer. On the contrary, NA showed a significant 10 % reduction of the molecular weight compared to TT meaning NaOH etching affects to a deeper surface layer compared to the other treatments.

A huge difference in crystallinity is observed between STNT, and the processed films. COM and STNT presented respectively a percentage of crystallinity of 18.7 ± 2.3 and 50.5 ± 2.7 %. SC presented a percentage of crystallinity 3 times lower than the PL65 pellet employed for this synthesis. This decrease of crystallinity due to solvent casting process has already been reported [35] and is mainly associated to the fast chloroform evaporation not allowing polymer macromolecules to diffuse to the crystal growth front and overcome the energy barrier of deposition [36]. As expected, thermal treatment helped to increase crystallinity in TT due to chain reorganization [30,37]. The three activation treatments did not affect crystallinity.

A tensile test was done on SC and TT to evaluate the effect of the thermal treatment on mechanical properties. TT films presented a 5 times higher Young modulus (2.85 ± 0.27 GPa) and 2 times higher UTS (62.2 ± 5.7 MPa) compared to SC films (E: 0.53 ± 0.10 GPa and UTS: 28.9 ± 2.6 MPa). The increased mechanical properties on TT films are related to the increased crystallinity [38] and

the evaporation of solvent residues produced by the thermal treatment. Indeed, solvent residues act as a plasticizer and reduce dramatically tensile strength [35]. The Young modulus and UTS of TT films are in the upper range of the mechanical properties reported for PLLA family [39]. Consequently, the obtained solvent-cast PLLA would probably respond properly to the mechanical stress occurring during stent implantation. This could be of great interest to obtain 3D printed PLLA biodegradable stent by solvent casting direct write technique [18].

Table V.2: *Bulk properties of COM, STNT and all the different solvent-cast films: presence of Cl residues, M_w = molecular weight obtained by HPLC and % of crystallinity following DSC.*

Sample	Cl residues	Mw (10^6 g/mol)	*% cristallinity*
COM	Yes	0.16 ± 0.00	18.7 ± 2.3
STNT	No	0.19 ± 0.00	50.5 ± 2.7
SC	Yes	0.95 ± 0.04	12.5 ± 3.1
TT	No	0.98 ± 0.03	26.6 ± 2.7
PL	No	0.95 ± 0.01	25.1 ± 1.7
NA	No	0.89 ± 0.01	24.2 ± 2.7
ENZ	No	0.97 ± 0.02	25.8 ± 0.4

3.2. Surface characterization

Surface roughness modifications due to activation treatments were characterized by white light interferometry (WLI) (**Figure V.1**). SC surfaces obtained the lowest value of R_a, but it was statistically equal to TT, PL and ENZ suggesting these three treatments had a negligible effect on the surface roughness. Contrary, the effect of NaOH treatment was more aggressive and modified surface roughness parameters by doubling the parameter Ra compared to the other films. In addition to the fact that NaOH treatment also decreased PLLA molecular weight, it is suggested that alkaline activation process was a more aggressive treatment than plasma and enzyme treatment, affecting few microns depth from the surface of PLLA films.

Wettability of the different fabricated PLLA films was characterized by water contact angle (Figure V.1). Water contact angle on SC films is 10º higher than COM (70.0 ± 0.7º) as reported in a previous study [40]. This difference could be explained by the higher M_w of the PLLA used to fabricate SC films, inducing a

lower density of surface functional groups and consequently a lower hydrophilicity [13]. Wettability evaluation revealed also that thermal treatment increased significantly water contact angle compared to SC. NaOH etching did not change the wettability as NA presented a water contact angle of 84.2 ± 4.3º with no-statistical difference when compared to TT. On the other hand, plasma and enzyme activation treatments reduced significantly water contact angle, obtaining values ≈ 20º and ≈ 25º, respectively, lower than TT. Other authors have already reported the increase in hydrophilicity after plasma treatment [13,41,42] and enzymatic hydrolysis [21,42,43] on PLA, or other polyesters. This is usually attributed to the creation of new surface functional groups [13,41,42].

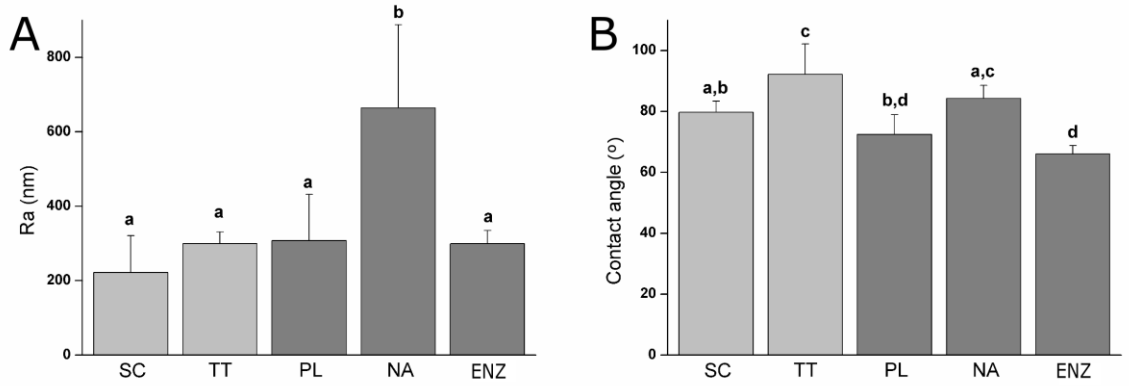

Figure V.1: *Surface properties of all the solvent-cast PLLA films. (A) Roughness Ra (arithmetic roughness average) calculated from WLI images. (B) Water contact angle on the different PLLA films. Columns marked with different letters belong to statistically different groups (p-value < 0.05).*

Surface chemical composition of TT and activated films is shown in **Table V.3**. XPS analysis revealed the presence of C 1s, O 1s, N 1s and Na 1s. The atomic percentage of O 1s increased while C 1s decreased for all activated surfaces compared to TT films. Consequently, O/C ratio was higher on activated surfaces (> 0.64) compared to TT (0.61). The increase confirmed the incorporation of O 1s on the PLLA films surfaces to form functional group. O/C ratio was statistically higher on PL and ENZ films, 0.75 and 0.97, respectively compared to NA (0.64), suggesting a higher efficiency of plasma and enzyme to create functional groups. Also, presence of N 1s was observed in small quantities on PL and ENZ films 0.8 ± 0.1 and 0.5 ± 0.1 %, respectively. For PL samples, the detection of N 1s was associated with air contaminations in the plasma chamber. But for ENZ samples it was associated to residues of cutinase, as cutinase contains nitrogen [44]. Finally,

NA films showed the presence of Na 1s at a low quantity (0.5 ± 0.1 %), these residues of NaOH could explain the cytotoxicity observed on these films.

Table V.3: *Analysis of the atomic composition percentage at the TT, PL, NA and ENZ surfaces by XPS. Values of O 1s, C 1s, N 1s, Na 1s and ratio between O/C were obtained from the XPS survey spectra. Values of the relative chemical carbon bonds were obtained from the deconvolution of C 1s peaks.*

	Elemental composition (atomic %)					**Relative chemical carbon bonds (%)**		
	O 1s	C 1s	N 1s	Na 1s	**O/C**	**284.7 eV C-C, C-H**	**286.6 eV C-O**	**288.8 eV O=C-O**
TT	37.7 ± 0.5	62.3 ± 0.5	0.0 ± 0.0	0.0 ± 0.0	0.61	42.1 ± 0.9	28.7 ± 0.7	**29.2 ± 0.6**
PL	42.3 ± 0.3	56.8 ± 0.4	0.8 ± 0.1	0.0 ± 0.0	0.75	30.4 ± 0.2	32.8 ± 0.1	**36.9 ± 0.1**
NA	39.0 ± 0.3	60.9 ± 0.2	0.0 ± 0.0	0.2 ± 0.0	0.64	34.6 ± 0.9	34.7 ± 1.4	**30.7 ± 1.0**
ENZ	49.0 ± 0.2	50.4 ± 0.2	0.5 ± 0.1	0.0 ± 0.0	0.97	31.1 ± 0.4	32.4 ± 0.6	**36.6 ± 0.4**

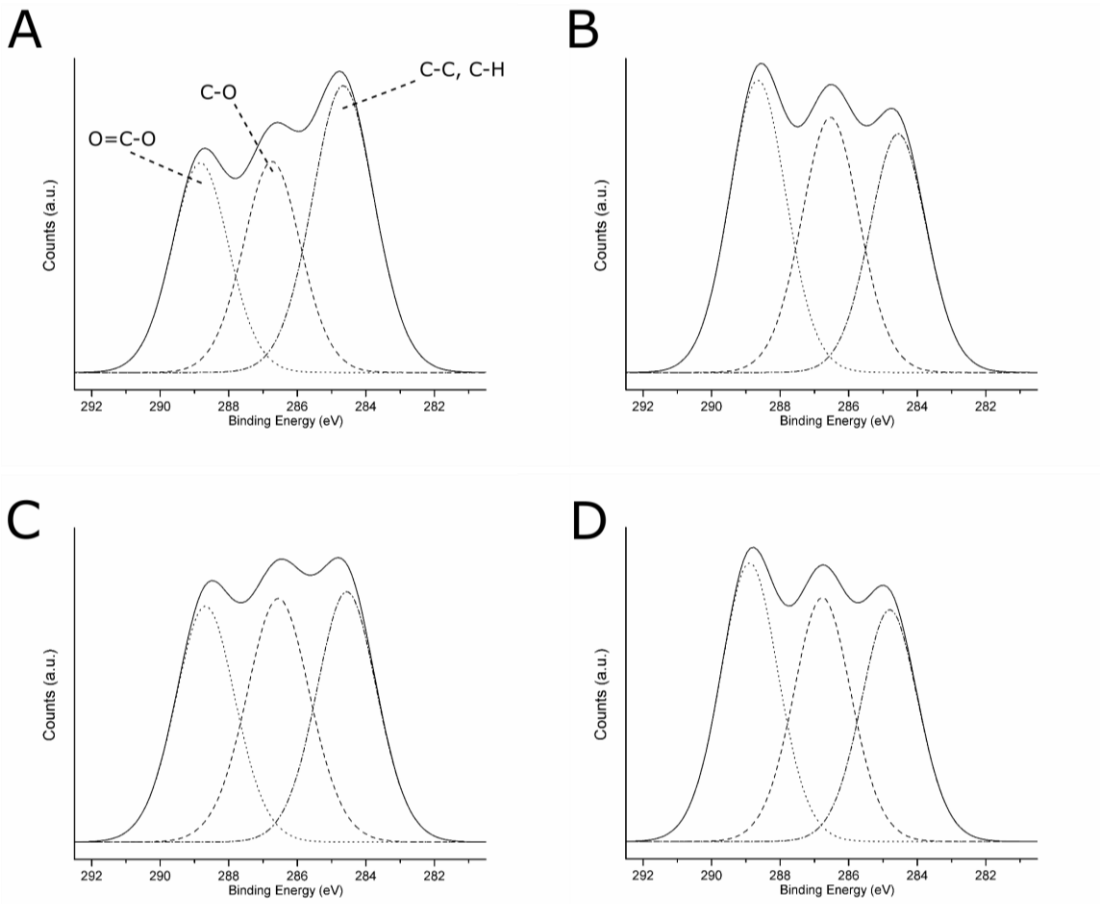

Figure V.2: *High-resolution spectra of C 1s obtained by XPS for (A) TT, (B) PL, (C) NA and (D) ENZ surfaces. Dashed lines represent the fitting components and solid lines the sum of these components.*

The deconvolution of the high-resolution C 1s peak has been applied for TT and activated samples (Table V.3 and **Figure V.2**). On all surfaces, C 1s peak was composed of three peaks corresponding to: (1) C – C and C – H bonds at 284.7 eV; (2) C – O bonds at 286.6 eV and; (3) O = C – O bonds at 288.8 eV [42]. All activated surfaces presented a significantly higher atomic percentage of O = C - O bonds (> 30.7 ± 1.0 %) than TT films (29.2 ± 0.6 %) meaning all three activation treatments created – COOH functional groups. Plasma and enzyme treatments presented 36.9 ± 0.1 and 36.6 ± 0.4 % of O = C – O bonds, respectively, meaning a higher amount of carboxyl group were created on these surfaces than on alkaline surface (30.7 ± 1.0 %). When hydrolyzing an ester bond, a single - COOH and a single - OH group are created [45]. As NaOH solution and enzyme act on PLLA only by ester bond hydrolysis, on NA and ENZ surfaces the increase of hydroxyl group is proportional to the increase of the generated carboxyl groups. Plasma treatment do not act only by hydrolysis, there is also a formation of functional group in surface with the oxygen excited species present in the plasma. The fact that O/C ratio was inferior on PL compared to ENZ and that PL and ENZ presented similar percentage of carboxyl group suggested that PL had less hydroxyl groups than ENZ.

The higher density of functional group on PL and ENZ compared to NA samples is coherent with the higher decrease of wettability observed after plasma or enzyme hydrolysis compared to alkaline hydrolysis, suggesting plasma and enzyme hydrolysis presented the best efficiency to create functional group in order to biofunctionalized a surface or to improve implant biological response.

3.3. Degradation of PLLA films

BRS stents are expected to maintain their radial strength at least during the 6 months post implantation, the stent material should degrade without losing mechanical properties during this period of time [46,47]. High M_w PLLA are expected to have a slow degradation rate compared to low M_w polyester [48]. An accelerated degradation assay was conducted in conditions similar to previous works [29–31,49]. The films were immersed in a 0.1 M NaOH solution during 10 days in order to evaluate the effect of solvent-casting, thermal and activation treatments on degradation of high M_w PLLA by measuring the percentage of mass

loss (**Figure V.3**). Moreover, surface SEM images and roughness of the studied surfaces before and after the degradation assay are shown in **Figure V.4**.

As expected, all samples presented a linear decrease of the percentage of mass loss with time. This behaviour, was already described by D. Cam *et al.* [29] in alkaline solution and it is totally different to the sigmoidal degradation pattern observed for PLLA in saline and buffered solutions or in body conditions related by Middleton *et al*. [47]. COM and SC films clearly presented statistically faster degradation rates compared to other surfaces. For example SC and COM mass loss after 10 days was higher than 45 %; whereas, all the other films had a mass loss lower than 30 %. According to literature [29], as degradation occurs first in the amorphous part, the faster degradation on SC and COM could be explained by the lower crystallinity of these films. In addition, on one hand, PL and ENZ films presented a mass loss statistically equal to TT films at each time point, suggesting that the studied activation treatments do not affect PLLA degradation since they act at the outermost layers of the surface. On the other hand, NA films presented a slightly faster degradation rate than TT films resulting probably from the greater surface in contact with the NaOH solution, due to the higher roughness. Finally, TT, PL and ENZ films showed a degradation rate statistically similar to Remedy stent (STNT) degradation rate. Associating this result with the high mechanical properties of TT films observed and the non-modified crystallinity and Mw after plasma and enzyme hydrolysis, it can be concluded that TT, PL and ENZ films are suitable for stent fabrication.

According to the SEM images, a clear degradation of the surface and an increased roughness can be observed for all samples, except for STNT surface. The faster degradation observed by mass loss on SC and COM compared to the other samples was confirmed by a higher surface deterioration, and an increase of Ra by a factor of 5.51 and 11.65, respectively. Surfaces with thermal treatment presented a lower surface degradation and Ra was increased by a factor 1.86. Thus, confirming that the increase of crystallinity made the PLLA more resistant to degradation. NaOH, plasma and enzyme activated surfaces had a surface degradation similar to TT, confirming also that the studied activation treatments did not affect PLLA degradation.

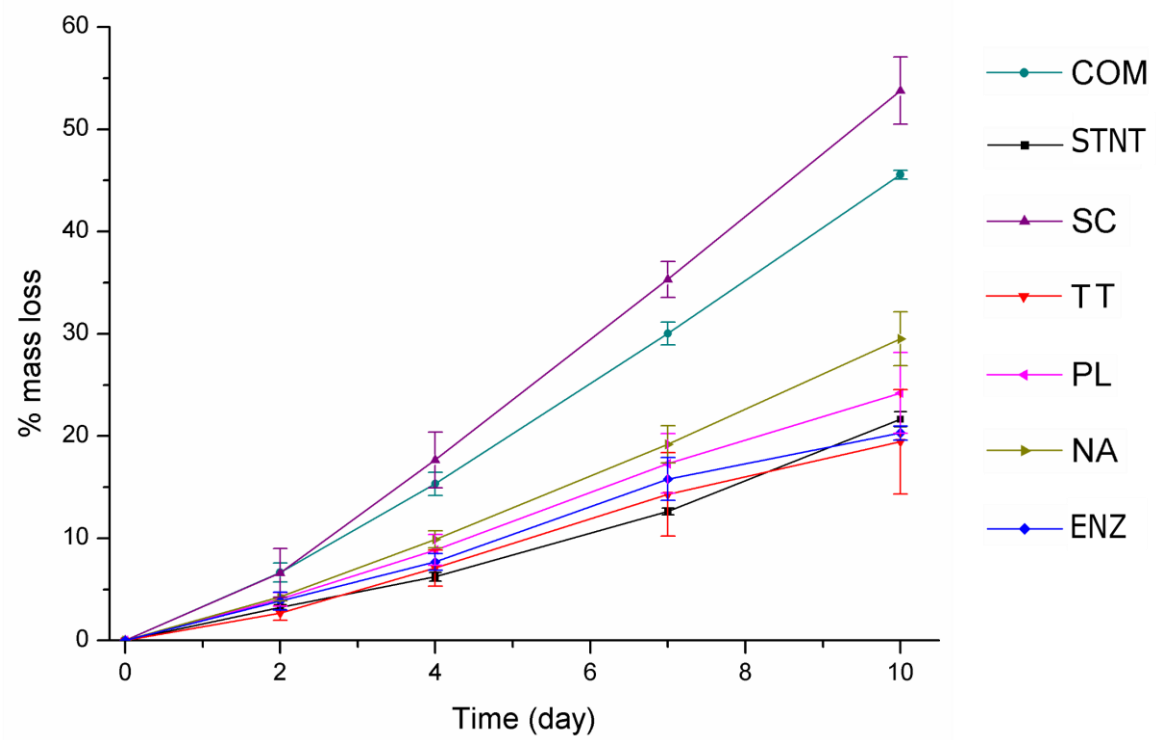

Figure V.3: *% mass loss evolution during alkaline accelerated degradation assay on COM, STNT and all solvent-cast PLLA films. Assay was done in a 0.1 M NaOH solution during 10 days.*

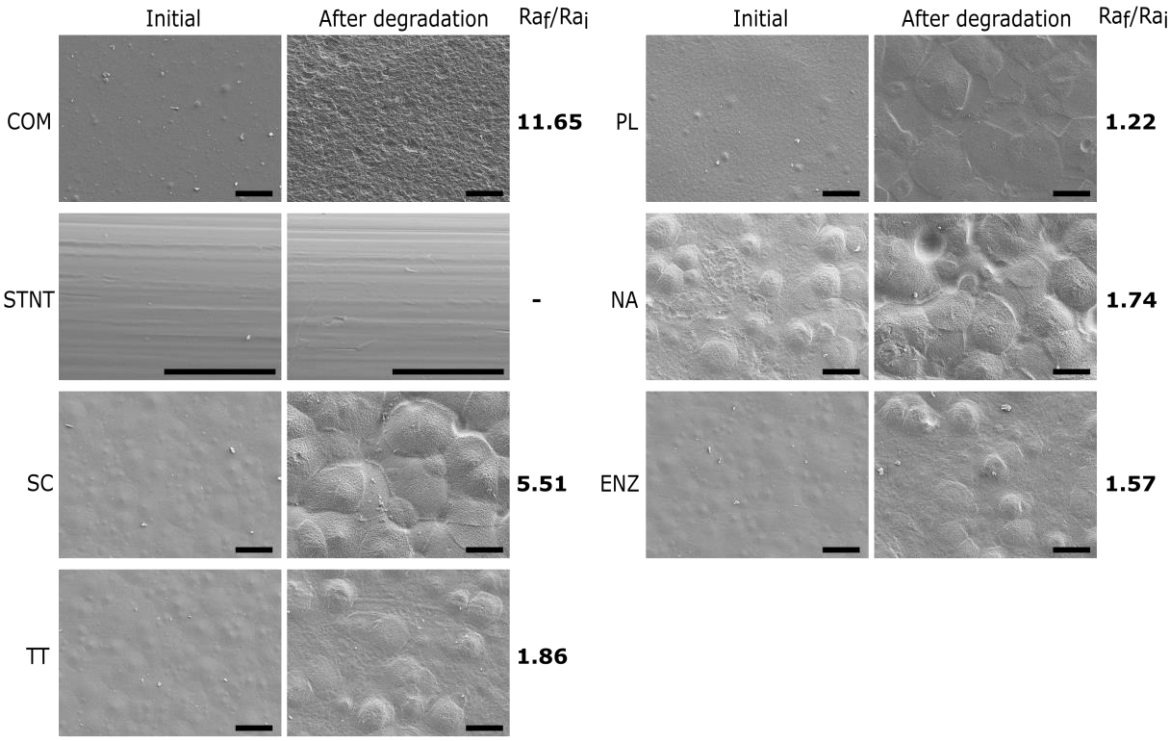

Figure V.4: *SEM images and roughness ratio Ra_f/Ra_i of COM, STNT and all solvent-cast PLLA films before and after alkaline accelerated degradation assay. Assay was done in a 0.1 M NaOH solution during 10 days. Scale bar = 50 µm. Roughness was obtained from WLI. STNT roughness could not be characterized for geometrical reasons.*

3.4. HUVECs adhesion

In order to biologically characterize the effect of plasma, NaOH and enzyme hydrolysis of PLLA solvent-cast films, it was evaluated HUVECs adhesion after 12 h of cell culture. Cell number was slightly higher on NA films (25787 ± 2288 cells/cm^2) compared to TT surfaces (21297 ± 1528 cell/cm^2) (**Figure V.5A**). Whereas, PL and ENZ films presented statistically higher number of HUVECs, 36958 ± 2967 and 33541 ± 4434 cells/cm^2 respectively, compared to TT and NA samples. SEM images confirmed visually the higher cell density on activated surfaces and showed a higher spreading on these surfaces compared to TT films (**Figure V.6**). In particular, cell close-up images of TT surfaces showed round HUVECs, non-expanded, showing an initial adhesion stage with many extended *filopodia*. On the contrary, HUVECs on PL, NA and ENZ films were flat and extended. This higher cell number and spreading on activated surfaces induced a percentage of area occupied by HUVECs at least 4 times higher compared to TT samples (**Figure V.5B**). Plasma and enzyme activation had the highest values with 66.0 ± 11.5 and 58.7 ± 3.9 %, respectively. Surface characteristics such as wettability and functional group density evolved proportionally with HUVECs adhesion on the three functionalized surfaces, confirming the relationship between higher functional group density, hidrophilicity and increased cell adhesion. The reason for this correlation could be attributed to a higher protein adsorption on hydrophilic surfaces, as reported previously [50,51]. In summary, concerning the effect of the different activation treatments applied to PLLA surfaces on cell response we found that, on the one hand, plasma and enzyme activation increased PLLA biocompatibility by improving HUVECs adhesion and also, created a higher density of surface functional groups that can be used to covalently immobilize biomolecules. On the other hand, sodium hydroxide activation showed a lower density of activated functional groups onto the surface compared to other activation treatments and HUVECs adhesion slightly increased compared to control. Moreover, NaOH activation increased PLLA films roughness which could dramatically induce a higher platelet adhesion and promote thrombus formation when using this surface for cardiovascular applications [52,53].

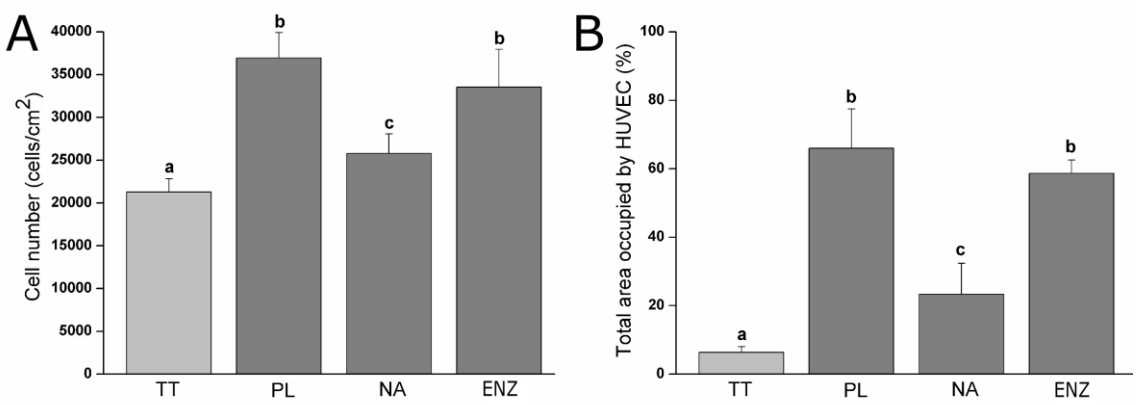

Figure V.5: *HUVECs adhesion and spreading on TT and activated films after 12 h of cell culture. (A) Cell number quantified by LDH enzymatic assay. (B) % of area occupied by HUVEC obtained after SEM images analysis. Images were analysed with FIJI software. Columns with different letters belong to statistically different groups (p-value < 0.05).*

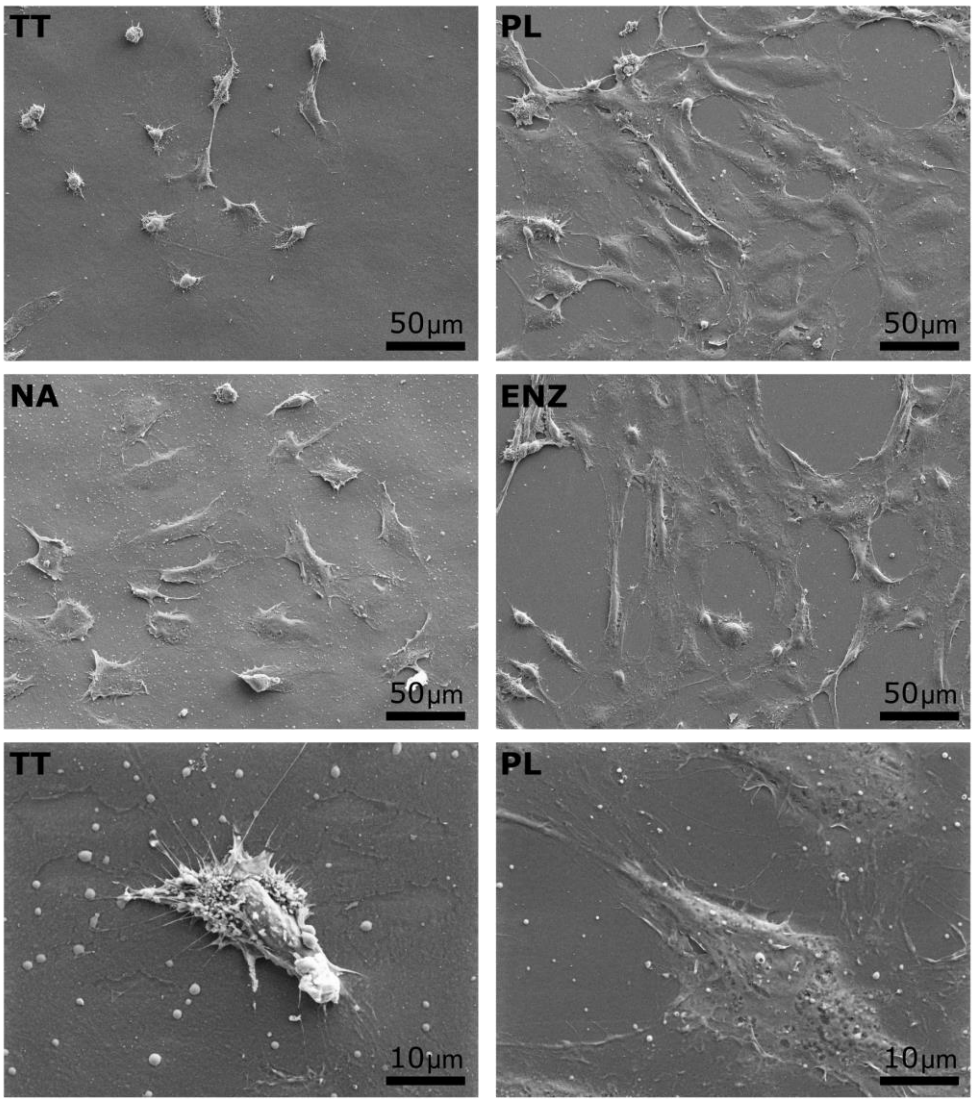

Figure V.6: *SEM images of HUVECs adhesion and spreading on TT and activated surfaces after 12h of incubation.*

3.5. BRS obtained by solvent-cast direct write technique

Solvent-cast high molecular weight PLLA activated with plasma or enzymes presented appropriate cristallinity, molecular weight, degradation rate and enhanced ECs response which makes it a biomaterial suitable to be used for BRS fabrication. As a proof of concept, PLLA BRS stent were fabricated by solvent-cast direct write technique to assess its feasibility. The 3D-printer was modified with a rotating mandrel and it was successfully fabricated seamless BRS of 5 mm diameter and 20 mm length (**Figure V.7**). The stents presented homogeneous wire diameter around 150 µm and the junctions between wires were welded properly.

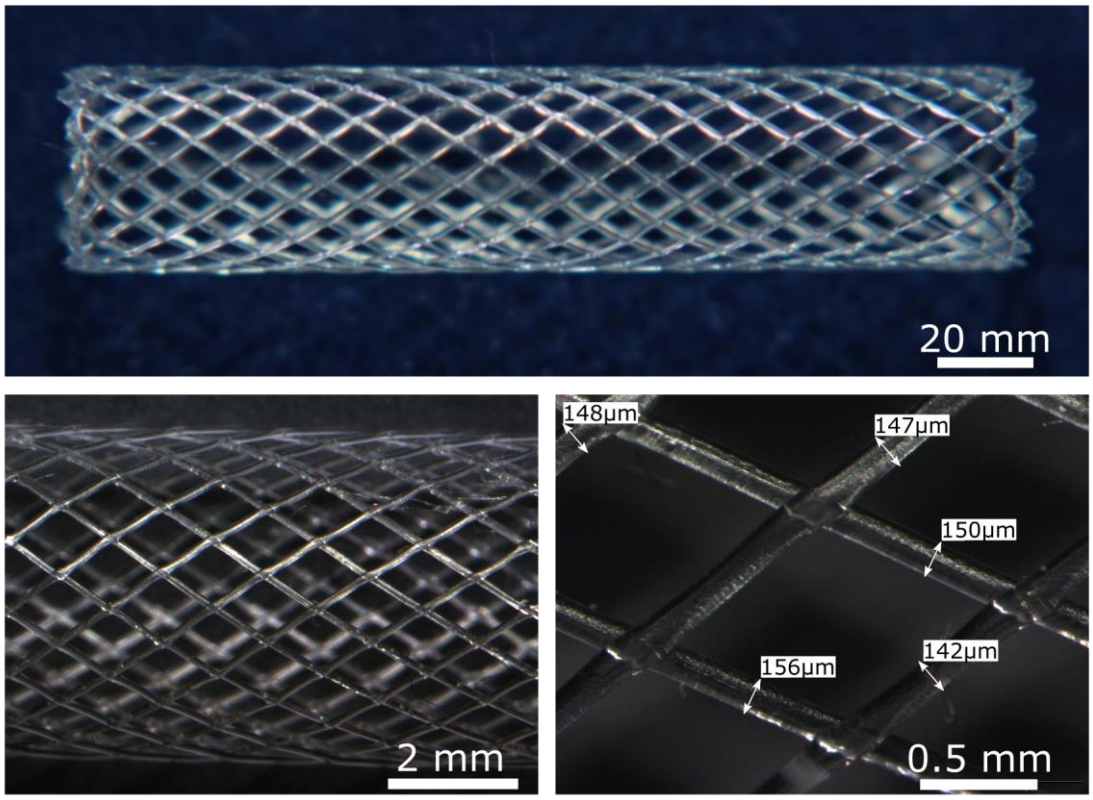

Figure V.7: *PLLA BRS obtained by solvent-cast direct write technique. Upper image: General image of PLLA BRS by optical microscopy. Lower images: Detailed optical microscopy images of the PLLA BRS wires.*

4. Conclusions

In this work, we evaluate the potential of solvent-cast PLLA functionalized by oxygen plasma, NaOH solution or cutinaze enzyme to enhance ECs adhesion and to be used for 3D-printed BRS fabrication. After thermal treatment,

solvent-cast PLLA presented full biocompatibility, high mechanical properties and degradation rates similar to the commercial Remedy BRS. Moreover, plasma and enzyme functionalization that did not affect the bulk properties of the PLLA films, increased significantly the hydrophilicity, the density of surface functional groups and the ECs adhesion and spreading. On the contrary, NaOH hydrolysis was not fully biocompatible and was proven to be less efficient than plasma and enzymes in terms of creating functional groups and improving ECs response. Finally, solvent-cast direct write technique was used to print on a rotating mandrel and 3D-printed PLLA BRS seamless were obtained. Consequently, the combined use of the solvent-cast direct write technique and plasma or enzyme functionalization holds great potential to fabricate 3D-printed PLLA BRS with the capacity to accelerate the surface endothelialization.

References

(1) Nazneen, F.; Herzog, G.; Arrigan, D. W. M.; Caplice, N.; Benvenuto, P.; Galvin, P.; Thompson, M. Surface Chemical and Physical Modification in Stent Technology for the Treatment of Coronary Artery Disease. *J. Biomed. Mater. Res. B. Appl. Biomater.* **2012**, *100B* (7), 1989–2014.

(2) Schieber, R.; Lassarre, F.; Hans, M.; Fernandez-Yague, M.; Diaz-Ricart, M.; Escolar, G.; Ginebra, M.-P.; Mucklich, F.; Pegueroles, M. Direct Laser Interference Patterning of CoCr Alloy Surfaces to Control Endothelial Cell and Platelet Response for Cardiovascular Applications. *Accept. Adv. Healthc. Mater.* **2016**.

(3) Att, W.; Hori, N.; Iwasa, F.; Yamada, M.; Ueno, T.; Ogawa, T. The Effect of UV-Photofunctionalization on the Time-Related Bioactivity of Titanium and Chromium-Cobalt Alloys. *Biomaterials* **2009**, *30* (26), 4268–4276.

(4) Koo, G.-H.; Jang, J. Surface Modification of Poly(lactic Acid) by UV/Ozone Irradiation. *Fibers Polym.* **2009**, *9* (6), 674–678.

(5) Chen, L.; Liu, M.; Bai, H.; Chen, P.; Xia, F.; Han, D. Antiplatelet and Thermally Responsive Poly (N -Isopropylacrylamide) Surface with Nanoscale. **2009**, No. 18, 10467–10472.

(6) Sun, T.; Tan, H.; Han, D.; Fu, Q.; Jiang, L. No Platelet Can Adhere-Largely Improved Blood Compatibility on Nanostructured Superhydrophobic Surfaces. *Small* **2005**, *1* (10), 959–963.

(7) de Mel, A.; Jell, G.; Stevens, M. M.; Seifalian, A. M. Biofunctionalization of Biomaterials for Accelerated in Situ Endothelialization: A Review. *Biomacromolecules* **2008**, *9* (11), 2969–2979.

(8) Castellanos, M. I.; Mas-Moruno, C.; Grau, A.; Serra-Picamal, X.; Trepat, X.; Albericio, F.; Joner, M.; Manero, J. M.; Pegueroles, M. Functionalization of CoCr Surfaces with Cell Adhesive Peptides to Promote HUVECs Adhesion and Proliferation. *Appl. Surf. Sci.* **2016**, *393*, 82–92.

(9) Nyanhongo, G. S.; Rodríguez, R. D.; Prasetyo, E. N.; Caparrós, C.; Ribeiro, C.; Sencadas, V.; Lanceros-Mendez, S.; Acero, E. H.; Guebitz, G. M. Bioactive Albumin Functionalized Polylactic Acid Membranes for Improved Biocompatibility. *React. Funct. Polym.* **2013**, *73* (10), 1399–1404.

(10) Chen, X.; Sevilla, P.; Aparicio, C. Surface Biofunctionalization by Covalent Co-Immobilization of Oligopeptides. *Colloids Surfaces B Biointerfaces* **2013**, *107*, 189–197.

(11) Chu, P. K.; Chen, J. Y.; Wang, L. P.; Huang, N. Plasma-Surface Modification of Biomaterials. **2002**, *36*, 143–206.

(12) Siow, K. S.; Britcher, L.; Kumar, S.; Griesser, H. J. Plasma Methods for the Generation of Chemically Reactive Surfaces for Biomolecule Immobilization and Cell Colonization - A Review. *Plasma Process. Polym.* **2006**, *3* (6–7), 392–418.

(13) Jordá-Vilaplana, a.; Fombuena, V.; García-García, D.; Samper, M. D.; Sánchez-Nácher, L. Surface Modification of Polylactic Acid (PLA) by Air Atmospheric Plasma Treatment. *Eur. Polym. J.* **2014**, *58*, 23–33.

(14) Miller, D. C.; Thapa, A.; Haberstroh, K. M.; Webster, T. J. Endothelial and Vascular Smooth Muscle Cell Function on Poly(lactic-Co-Glycolic Acid) with Nano-Structured Surface Features. *Biomaterials* **2004**, *25* (1), 53–61.

(15) Serrano, M. C.; Portolés, M. T.; Vallet-Regí, M.; Izquierdo, I.; Galletti, L.; Comas, J. V.; Pagani, R. Vascular Endothelial and Smooth Muscle Cell Culture on NaOH-Treated Poly(epsilon-Caprolactone) Films: A Preliminary Study for Vascular Graft Development. *Macromol. Biosci.* **2005**, *5* (5), 415–423.

(16) Pellis, A.; Herrero Acero, E.; Ferrario, V.; Ribitsch, D.; Guebitz, G. M.; Gardossi, L. The Closure of the Cycle: Enzymatic Synthesis and Functionalization of Bio-Based Polyesters. *Trends Biotechnol.* **2016**, *34* (4), 316–328.

(17) Pellis, A.; Silvestrini, L.; Scaini, D.; Coburn, J. M.; Kaplan, D. L.; Herrero, E.; Guebitz, G. M. Enzyme-Catalyzed Functionalization of Poly (L-Lactic Acid) for Drug Delivery Applications. *Process Biochem.* **2016**, 1–20.

(18) Guo, S. Z.; Gosselin, F.; Guerin, N.; Lanouette, A. M.; Heuzey, M. C.; Therriault, D. Solvent-Cast Three-Dimensional Printing of Multifunctional Microsystems. *Small* **2013**, *9* (24), 4118–4122.

(19) Byun, Y.; Whiteside, S.; Thomas, R.; Dharman, M.; Hughes, J.; Carolina, S. The Effect of Solvent Mixture on the Properties of Solvent Cast Polylactic Acid (PLA) Film. *J. Appl. Polym. Sci.* **2011**, 3577–3582.

(20) Buxadera-Palomero, J.; Canal, C.; Torrent-Camarero, S.; Garrido, B.; Javier Gil, F.; Rodríguez, D. Antifouling Coatings for Dental Implants: Polyethylene Glycol-like

Coatings on Titanium by Plasma Polymerization. *Biointerphases* **2015**, *10* (2), 29505.

(21) Pellis, A.; Acero, E. H.; Weber, H.; Obersriebnig, M.; Breinbauer, R.; Srebotnik, E.; Guebitz, G. M. Biocatalyzed Approach for the Surface Functionalization of poly(L-Lactic Acid) Films Using Hydrolytic Enzymes. *Biotechnol. J.* **2015**, *10* (11), 1739–1749.

(22) American Society for Testing and Materials International. Standard Test Method for Transition Temperatures and Enthalpies of Fusion and Crystallization of Polymers by Differential Scanning, ASTM D3418 - 03, 2003.

(23) Fischer, E. W.; Sterzel, H. J.; Wegner, G. Investigation of the Structure of Solution Grown Crystals of Lactide Copolymers by Means of Chemical Reactions. *Kolloid-Zeitschrift Zeitschrift für Polym.* **1973**, *251* (11), 980–990.

(24) Zhai, W.; Ko, Y.; Zhu, W.; Wong, A.; Park, C. B. A Study of the Crystallization, Melting, and Foaming Behaviors of Polylactic Acid in Compressed CO2. *Int. J. Mol. Sci.* **2009**, *10* (12), 5381–5397.

(25) American Society for Testing and Materials International. Standard Test Method for Tensile Properties of Thin Plastic Sheeting, ASTM D882 - 02, 2002.

(26) American Society for Testing and Materials International. Standard Practice for Cutting Film and Sheeting Test Specimens, ASTM D6287 - 98, 1998.

(27) International Organization for Standardization. Biological Evaluation of Medical Devices. Part 5: Citotoxicity in Vitro Assays ISO 10993-5, 2009.

(28) Owens, D. K.; Wendt, R. C. Estimation of the Surface Free Energy of Polymers. *J. Appl. Polym. Sci.* **1969**, *13* (8), 1741–1747.

(29) Cam, D.; Hyon, S.; Ikada, Y. Degradation of High Molecular Weight Poly(l-Lactide) in Alkaline Medium. *Biomaterials* **1995**, *16* (11), 833–843.

(30) Vasanthan, N.; Ly, O. Effect of Microstructure on Hydrolytic Degradation Studies of Poly (L-Lactic Acid) by FTIR Spectroscopy and Differential Scanning Calorimetry. *Polym. Degrad. Stab.* **2009**, *94* (9), 1364–1372.

(31) Tsuji, H.; Ikada, Y. Properties and Morphology of Poly (L -Lactide). II . Hydrolysis in Alkaline Solution. *J. Polym. Sci. Part A-Polymer Chem.* **1997**, *36*, 59–66.

(32) Schindelin, J.; Arganda-Carreras, I.; Frise, E.; Kaynig, V.; Longair, M.; Pietzsch, T.; Preibisch, S.; Rueden, C.; Saalfeld, S.; Schmid, B.; Tinevez, J.-Y. J.-Y.; White, D. J.;

Hartenstein, V.; Eliceiri, K.; Tomancak, P.; Cardona, A.; Liceiri, K.; Tomancak, P.; A., C. Fiji: An Open Source Platform for Biological Image Analysis. *Nat. Methods* **2012**, *9* (7), 676–682.

(33) Salama, A. F.; Tousson, E.; Shalaby, K. A. F.; Hussien, H. T. Protective Effect of Curcumin on Chloroform as by-Product of Water Chlorination Induced Cardiotoxicity. *Biomed. Prev. Nutr.* **2014**, *4* (2), 225–230.

(34) Fang, C.; Behr, M.; Xie, F.; Lu, S.; Doret, M.; Luo, H.; Yang, W.; Aldous, K.; Ding, X.; Gu, J. Mechanism of Chloroform-Induced Renal Toxicity: Non-Involvement of Hepatic Cytochrome P450-Dependent Metabolism. *Toxicol. Appl. Pharmacol.* **2008**, *227* (1), 48–55.

(35) Rhim, J.-W.; Mohanty, A. K.; Singh, S. P.; Ng, P. K. W. Effect of the Processing Methods on the Performance of Polylactide Films: Thermocompression versus Solvent Casting. *J. Appl. Polym. Sci.* **2006**, *101* (6), 3736–3742.

(36) Hsu, S.; Yao, Y. L. Effect of Film Formation Method and Annealing on Crystallinity of poly(L-Lactic Acid) Films. *Msec2011-50205* **2011**, 1–10.

(37) Weir, N. A.; Buchanan, F. J.; Orr, J. F.; Farrar, D. F.; Boyd, A. Processing, Annealing and Sterilisation of Poly-L-Lactide. *Biomaterials* **2004**, *25* (18), 3939–3949.

(38) Perego, G.; Cella, G.; Bastioli, C. Effect of Molecular Weight and Crystallinity on Poly (Lactic Acid) Mechanical Properties. *J. Appl. Polym. Sci.* **1996**, *59*, 37–43.

(39) Van de Velde, K.; Kiekens, P. Biopolymers: Overview of Several Properties and Consequences on Their Applications. *Polym. Test.* **2002**, *21* (4), 433–442.

(40) Canal, C.; Gallinetti, S.; Ginebra, M. P. Low-Pressure Plasma Treatment of Polylactide Fibers for Enhanced Mechanical Performance of Fiber-Reinforced Calcium Phosphate Cements. *Plasma Process. Polym.* **2014**, *11* (7), 694–703.

(41) Hirotsu, T.; Nakayama, K.; Tsujisaka, T.; Mas, A.; Schue, F. Plasma Surface Treatments of Melt-Extruded Sheets of poly(L-Lactic Acid). *Polym. Eng. Sci.* **2002**, *42* (2), 299–306.

(42) Tkavc, T.; Vesel, A.; Acero, E. H.; Zemljič, L. F. Comparison of Oxygen Plasma and Cutinase Effect on Polyethylene Terephthalate Surface. *J. Appl. Polym. Sci.* **2013**, *128* (6), 3570–3575.

(43) Ribitsch, D.; Acero, E. H.; Greimel, K.; Dellacher, A.; Zitzenbacher, S.; Marold, A.; Rodriguez, R. D.; Steinkellner, G.; Gruber, K.; Schwab, H.; Guebitz, G. M. A New

Esterase from Thermobifida Halotolerans Hydrolyses Polyethylene Terephthalate (PET) and Polylactic Acid (PLA). *Polymers (Basel).* **2012**, *4* (1), 617–629.

(44) Pio, T. F.; Macedo, G. A. Optimizing the Production of Cutinase by Fusarium Oxysporum Using Response Surface Methodology. *Enzyme Microb. Technol.* **2007**, *41* (5), 613–619.

(45) Li, S. Hydrolytic Degradation Characteristics of Aliphatic Polyesters Derived from Lactic and Glycolic Acids Hydrolytic Degradation Characteristics of Aliphatic Polyesters Derived from Lactic and Glycolic Acids. *J. Biomed. Mater. Res.* **2016**, No. February 1999, 342–353.

(46) Oberhauser, J. P.; Hossainy, S.; Rapoza, R. J. Design Principles and Performance of Bioresorbable Polymeric Vascular Scaffolds BVS ABSORB Cohort B Device. *EuroIntervention* **2009**, *5*, 15–22.

(47) Middleton, J. C.; Tipton, A. J. Synthetic Biodegradable Polymers as Orthopedic Devices. *Biomaterials* **2000**, *21*, 2335–2346.

(48) Onuma, Y.; Serruys, P. W. Bioresorbable Scaffold: The Advent of a New Era in Percutaneous Coronary and Peripheral Revascularization? *Circulation* **2011**, *123* (7), 779–797.

(49) Delabarde, C.; Plummer, C. J. G.; Bourban, P. E.; Månson, J. A. E. Accelerated Ageing and Degradation in Poly-L-Lactide/hydroxyapatite Nanocomposites. *Polym. Degrad. Stab.* **2011**, *96* (4), 595–607.

(50) Arima, Y.; Iwata, H. Effect of Wettability and Surface Functional Groups on Protein Adsorption and Cell Adhesion Using Well-Defined Mixed Self-Assembled Monolayers. *Biomaterials* **2007**, *28* (20), 3074–3082.

(51) Shah, A.; Shaha, S.; Mani, G.; Wenke, J.; Agrawal, C. M. Endothelial Cell Behaviour on Gas-Plasma-Treated PLA Surfaces: The Roles of Surface Chemistry and Roughness. *J. Tissue Eng. Regen. Med.* **2011**, *5* (7), 301–312.

(52) Park, J. Y.; Gemmell, C. H.; Davies, J. E. Platelet Interactions with Titanium: Modulation of Platelet Activity by Surface Topography. *Biomaterials* **2001**, *22* (19), 2671–2682.

(53) Hecker, J. F.; Scandrett, L. A. Roughness and Thrombogenicity of the Outer Surfaces of Intravascular Catheters. *J. Biomed. Mater. Res.* **1985**, *19* (4), 381–395.

Chapter VI: General conclusions

Stents implantation has been a revolutionary advance in the treatment of atherosclerosis. However, none of the three stent generations, BMS, DES and BRS, achieved to avoid ISR and LST complications after coronary intervention. To overcome these drawbacks and to obtain a functional artery after coronary stent implantation, it is decisive to accelerate stent surface endothelialization and, if possible, without the use of antiproliferative drugs that generally delay the formation of a healthy endothelium.

Different strategies, based in surface modification, were explored in this thesis in order to control ECs and platelet response on CoCr alloy and PLLA surfaces for cardiovascular applications. The results displayed and analyzed in the previous chapters, which are summarized and highlighted in the following conclusions, expanded our comprehension in the field that could lead to the fabrication and design of stents with enhanced endothelialization and reduced platelet adhesion, ameliorating ISR and LST rates of actual commercial stents.

❖ Topography modification of CoCr alloy surfaces:

CoCr alloy was modified and linear patterned surfaces with periodicities between 3 and 32 μm and, depths around 20 and 800 nm were obtained by DLIP technique. Surface modification did not modify the corrosion properties and the surface charge of CoCr alloy. Low depth patterned surfaces presented negligible topographical modification and they did not show significant effect on ECs response compared to smooth CoCr surfaces. Otherwise, the significant topographical modifications of high depth patterned surfaces induced ECs elongation, alignment and migration following the pattern direction.

As a consequence of the high temperatures generated during DLIP, there was a transformation of the crystalline oxide layer into a thicker and homogeneous amorphous oxide layer with lower wettability. All patterned surfaces decreased

platelet adhesion and aggregation, indicating that the oxide layer structure transformation affected surface thrombogenicity.

❖ Topography modification and biofunctionalization of CoCr alloy surfaces:

The combination of topography and biochemical features as a strategy to accelerate and increase ECs adhesion and migration, was successfully achieved. Smooth and 10 µm periodicity patterned CoCr alloy surfaces were covalently biofunctionalized with RGD and YIGSR cell adhesive peptides through CPTES silanization. Peptide functionalization and, particularly YIGSR, increased the number of adhered ECs compared to non-functionalized surfaces. The majority of the coating peptide is stable when subjected to either gamma radiation sterilization or ultrasound sonication.

The combination of high-depth patterned and functionalized surfaces accelerated ECs migration and proliferation. The positive synergy between linear patterning and biofunctionalization makes this approach of great potential to accelerate endothelium healing without generating platelets adhesion and aggregation.

❖ Functionalization of solvent-cast PLLA films:

Biocompatible solvent-cast PLLA surfaces with mechanical properties and degradation rates similar to the commercial Remedy BRS were obtained after thermal treatment. Surface functionalization with oxygen plasma and cutinase enzyme increased significantly the hydrophilicity, the density of surface functional groups and the ECs adhesion and spreading without affecting the bulk mechanical and crystallinity properties of PLLA films. Consequently, plasma and cutinase enzyme PLLA hydrolysis could be used as a previous step for covalent immobilization of biomolecules or, directly, as a functionalization step to improve ECs response.

3D-printed PLLA BRS seamless were obtained by solvent-cast direct writing on a rotating mandrel. Consequently, the combined use of the solvent-cast direct write technique and plasma or cutinase enzyme functionalization could be a

potential strategy to fabricate 3D-printed PLLA BRSs with the capacity to accelerate the surface endothelialization.